3-2016

Thermal neutron analysis for improvised explosive device detection

Matthew David Marziale
Purdue University

Graduate School Form
30 Updated 12/26/2015

PURDUE UNIVERSITY
GRADUATE SCHOOL
Thesis/Dissertation Acceptance

This is to certify that the thesis/dissertation prepared

By Matthew David Marziale

Entitled

THERMAL NEUTRON ANALYSIS FOR IMPROVISED EXPLOSIVE DEVICE DETECTION

For the degree of Doctor of Philosophy

Is approved by the final examining committee:

Andrew Hirsch Chair	C2238
Marc Caffee	C5808
Chan Choi	C2505
Jorge Rodriguez	C5609

To the best of my knowledge and as understood by the student in the Thesis/Dissertation Agreement, Publication Delay, and Certification Disclaimer (Graduate School Form 32), this thesis/dissertation adheres to the provisions of Purdue University's "Policy of Integrity in Research" and the use of copyright material.

Approved by Major Professor(s): Andrew Hirsch

Approved by: Ken Ritchie 3/1/2016

Head of the Departmental Graduate Program Date

THERMAL NEUTRON ANALYSIS FOR IMPROVISED EXPLOSIVE DEVICE DETECTION

A Dissertation

Submitted to the Faculty

of

Purdue University

by

Matthew D. Marziale

In Partial Fulfillment of the

Requirements for the Degree

of

Doctor of Philosophy

May 2016

Purdue University

West Lafayette, Indiana

This dissertation is dedicated to the memory of my father, Dr. Michael L. Marziale (1957 – 2011), my first teacher, my mentor, my friend.

ACKNOWLEDGMENTS

I would like to extend my deepest appreciation to my committee chair Dr. Hirsch and co-chair Dr. Caffee, without whom I would never have been able to complete this dissertation. I would like to extend my thanks to the other members of my committee, Dr. Rodriguez, and Dr. Muzikar. My particular thanks to committee member Dr. Choi, for his wisdom and kindness through the years.

I also want to thank the Department of Physics, for providing the computational resources that made this dissertation possible.

In addition, I would also like to thank Mrs. Sandy Formica, for all of her tremendous help navigating the intricacies of Purdue.

Finally, I would like to thank my family for their unending support throughout the dissertation process.

TABLE OF CONTENTS

LIST OF TABLES

LIST OF FIGURES

Figure Page

Figure Page

ABSTRACT

Marziale, Matthew D. Ph.D., Purdue University, May 2016. Thermal Neutron Analysis for Improvised Explosive Device Detection. Major Professor: Andrew Hirsch.

In this dissertation, the design of a system to detect improvised explosive devices is considered. The technique utilized is thermal neutron analysis. In this method, thermal neutrons are used to interrogate a volume for the presence of nitrogen, which is used as an indicator of explosive, given its unusual high energy line in the gamma ray spectrum generated by thermal capture reactions on explosive material. The performance of the system is then considered for a number of devices used to represent an improvised explosive device, including a 155 mm shell, an antitank mine, and a air to surface bomb. The system is shown to be capable of detecting IEDs within between 15.6 and 3800 seconds for HPGe detectors, and within 277 seconds for the best case scenario with NaI while more deeply buried explosives are shown to be undetectable by NaI.

1. Introduction

From October 7, 2001 through May 31, 2011, improvised explosive devices, or IEDs, caused 31,625 casualties during military operations in Iraq and Afghanistan. This constitutes 63% of all casualties suffered [1], and thus present a very real threat.

While term improvised explosive device has only recently entered the lexicon of warfare, the usage of such devices has a long history. Recent examples have included bombings in Oklahoma City, Bali, London, Moscow, Cairo, and Madrid [2]. Among the earliest users of IEDs is the Irish Republican Army's forebearer, the Irish Republican Brotherhood. During the Clerkenwell Outrage of 1867, the IRB placed a cask of gunpowder against a prison wall in an attempt to free Richard O'Sullivan Burke, a gunrunner, leaving a sixty foot hole. IEDs also had a presence in World War II, during which they were employed by anti-Nazi resistance groups and retreating soldiers [3]. The Vietcong and the North Vietnamese Army also made extensive use of IEDs during the Vietnam War, often recycling unexploded ordnance (UXO) after bombing runs [4].

The Irish Republican Army particularly made expansive use of IEDs, having set more than 10,000 explosions using such devices by 1992, and remain as the world's most advanced builders of improvised explosive devices. Many terror groups' devices have been influenced by their designs. Their largest bomb, employed at the 1993 Bishopsgate Bombing using ANFO as its charge, had a yield of 1.2 kilotons. Such a yield is comparable to a small tactical nuclear weapon. They also devised sophisticated command detonation techniques to provide reliable, controllable detonation of an explosive charge. The techniques devised by the IRA included radio controlled detonation devices with encoding and decoding of signal pulses to thwart jamming devices, projectile command detonation in which a device was initiated by the attackers firing at two copper contacts which would close the initiation circuit, and a

device incorporating a photocell in the initiation circuit which could be triggered by an individual 100 meters away using a photography flash gun. They also pioneered a number of anti-handling devices to prevent deactivation of their explosives, the classical example of which was the mercury tilt switch, which would trigger the explosive if the bomb was tilted in any way. These techniques continue to be employed by other terror groups [3].

1.1 Improvised Explosive Device Characteristics

Improvised explosive devices vary greatly in their design; however, they always contain explosive materials, a triggering mechanism, and a detonator They are typically used by terrorist groups against soft targets, or against a stronger foe. What makes these devices so difficult to successfully defeat is the fact that attackers can often adapt more quickly to new countermeasures than those attacked can develop and deploy new countermeasures [5]. The most common examples of IEDs in Iraq and Afghanistan employ one or more 155mm artillery shells, though other forms of unexploded ordnance such as anti-tank mines and bombs are also employed. The most common military explosives employed are HMX, PETN, RDX, and TNT [6], though combination explosives such as Composition A and Composition B are also used. Devices that do not involve unexploded ordnance often use the improvised explosives TATP and HMTD, including the devices used in the 2005 London Bombings [6]. IEDs tend not to exceed more than a few hundred kilograms of explosives, and have a burial depth of no greater than 60 cm in soil [7].

A typical example of an Iraqi IED can be seen in Fig. 1.1. This device utilizes munitions from three different countries of origin, and three different explosive fillers. The devices include, from left to right, two French PR 14 artillery shells, an Italian VS-2.2 mine, and two Russian OF-26 artillery shells. The French PR 14 shells each contain 4.4 kg of TNT. The Italian VS-2.2 mine contains 3.8 kg of Composition B, which is a mixture of 59.5% RDX and 39.4% TNT. The Russian OF-26 artillery shells

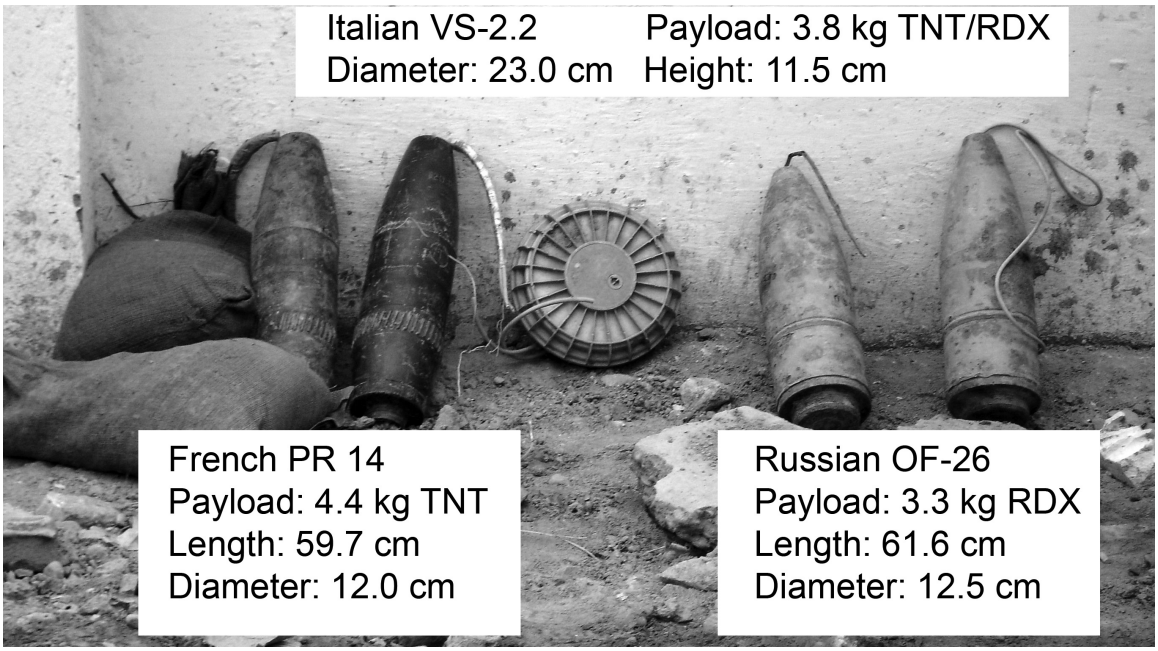

Figure 1.1. An example of a typical IED recovered in Bahgdad. [9]

both have a payload of 3.3 kg of RDX [8]. Dimensions given for the artillery shells are typical for such munitions. These munitions have their detonators daisy chained together to allow simultaneous detonation, another common feature of Iraqi IEDs.

1.2 Explosive Characteristics

Explosives are energetic materials which decompose rapidly by producing gases. The rate at which the explosive undergoes decomposition determines whether that explosive is a high or low explosive. If the reaction proceeds through the material at rate equal or less than the speed of sound, the process is referred to as deflagration, characteristic of low explosives. High explosives undergo detonation, in which the reaction proceeds through the material at a speed greater than that of sound.

Explosives are further subdivided according to their sensitivity to stimuli such as heat, spark, and friction. The most sensitive explosives are called primary explosives.

Typical examples include lead adize, mercury fulminate, and nitroglycerin. The next most sensitive group of explosives are secondary explosives, such as RDX, PETN, and TNT, which are much more insensitive to stimuli. They generally will not detonate without a powerful shock, and so explosive devices generally employ a main charge of a secondary explosive, and a detonator composed of a small quantity of primary explosive which is used to initiate the less sensitive main charge.

To maximize the expansion of material during the explosion, and thus produce the greatest effect, explosives must be dense and include elements to form gases, and so must include large amounts of carbon, hydrogen, nitrogen, and oxygen. The rapid decomposition also requires its own source of oxygen to proceed, so all explosives must contain oxygen. Optimal energy release occurs when there is enough oxygen that every hydrogen atom forms a water molecule and every carbon atom forms carbon monoxide [6]. The signature of explosive is thus a dense material (typically 1 – 2 g cm^{-3}) with large amounts of carbon, hydrogen, nitrogen, and oxygen, with the exception of TATP, a peroxide explosive which contains no nitrogen. Composition and other characteristics of explosives are given in Table 1.1.

Bulk detection of explosives is then based on the detection of concentrated hydrogen, nitrogen, oxygen, and carbon. There are many detection technologies for explosives. However, the presence of a large amount of parasitic material, soil, surrounding an explosive charge requires a detection method that can penetrate a large quantity of material and produce a return signal that can also penetrate that same material when returning to a detection system. Thermal neutron analysis, in which neutrons impinge upon a material and produce a return signal of prompt gamma rays, are a natural choice for this application, as both gamma rays which form the signal and the neutrons which produce them are highly penetrating forms of radiation.

Explosive	Density (TMD) (g/cm^3)	Detonation Velocity ($mm/\mu s$)	% TNT Trauzl	%N	%O	%C	%H
PETN	1.76	8.4	174	18	61	19	3
RDX	1.82	8.6	160	38	43	16	3
HMTD	1.6	5.1	60	13	46	34	6
TNT	1.65	6.9	100	19	42	37	2
HMX	1.96	9.1	160	38	43	–	–
AN	1.72 (0.8 bulk)	3.7	60	35	60	–	–
TNB	1.6	7.45	108	4	14	76	7
TATP	1.2	5.3	88	0	43	49	8

Table 1.1.
Characteristics of select explosives [6, 10]

2. Problem Approach

Many approaches have been applied to the problem of explosives detection. These approaches include electromagnetic induction, infrared imaging, electrical impedance tomography, nuclear quadrupole resonance, x–ray backscatter, electrochemical methods, the application of trained animals, non linear junction detection, and neutron interrogation. While many of these methods can be applied to explosives placed near the soil, only neutron interrogation is useful for detecting explosives placed far from the soil surface.

2.1 Electromagnetic Induction

Electromagnetic induction is used to identify explosives using the metallic content of the explosive device. A primary coil is driven with a time varying current, which in turn induces a current within the metallic object. The object's current then generates a varying magnetic flux within a pick up coil, which in turn generates a current in this coil, which serves as the signal for this detection method.

The primary problem with this approach is the extremely high false positive rate associated with technique, since this technique signals only the presence of metal, which is not specific to the presence of explosives. In the case of the detection of landmines, the EMI technique yields up to 1000 false positives for every mine detected. This is caused by the presence of metallic scrap within the soil. An additional cause of these false positives is the presence of ferrite soils, soils which are high in iron content and so will also trigger an EMI sensor [11]. However, there are advanced applications of EMI which can reduce this false positive rate.

One such improved system is the U.S. Army's AN/PSS–12 metal detector. Discrimination was made by exploiting the time dependent response of the metallic

object. The induced current in the object, and the resulting signal, exhibit an exponential decay which is dependent on the size, shape, conductivity, and permeability of the object. This decay time can then provide a fingerprint for the buried metallic object and be used to discriminate a target of interest from metallic scrap. A measurement of this decay time along a loop oriented in only one axis provided poor discrimination, which was only slightly better than chance. This system was then modified to allow the response to be measured along 3 axes, which improved results. The highest achieved probability of detection was only 25% if an acceptable false positive rate was to be maintained [12], making this system's performance unacceptable.

Several more systems with advanced detection capability were tested in a large collaboration under the International Pilot Project for Technology Co-operation. The systems tested included the Minelab F1A4 CMAC, the Pro–Scan Mark 2 VLF, the Minelab F1A4 MIM, the Vallon ML 1620C, and the Giat Model F1. The final report of this collaboration concluded that none of the systems evaluated were capable of finding all explosives devices during testing, and that moreover none were capable of detecting all mines down to 10 cm [13]. While in the future more advances may be made to improve detection probability and reduce false positives, the performance of current electromagnetic induction devices, especially for deeply buried munitions, is too poor to be a good candidate for a standalone detector.

2.2 Infrared Imaging

The alteration of the optical and thermal properties caused by the presence of a buried explosive or the act of burying the object can be used to detect the presence of a device. Because explosive devices have distinct physical properties in comparison to soil, they cause changes in the way electromagnetic radiation and heat behave in the surrounding soil [14]. This can be exploited to establish a means of detection.

2.2.1 Passive Thermal Imaging

One such method is passive thermal detection. Under this method, the ground is imaged using an IR sensor. Because the thermal properties of an explosive device are different from those of the surrounding soil, the soil in the vicinity of the device heats and cools at a different rate than the surrounding soil, leading to temperature differences in the soil that can then be detected. Because buried objects act as a barrier to thermal conduction, the soil above a buried object tends to be cooler than the surrounding soil during the night, and hotter during the day.

However, the contrast between the temperature of the object and the surrounding soil depends on the time of day. The longer the field is exposed to light, the fewer objects can be seen on the infrared camera, and so the number of detectable objects decreases. The greatest contrast between the surrounding soil and the object will occur during times with great amounts of heat transfer occurring. Since the primary input of heat into the soil is radiative transfer from the sun, this time is when the sun just began heating the soil, or stops heating the soil, so the greatest contrast occurs during sunrise and sunset. Consequently, there are also times when there will be little contrast between the object and surrounding soil, which will occur when heat transfer conditions have been steady for some time, so as the day or night progresses the temperature differential will decrease making detection difficult [15]. Deeply buried objects will also be difficult to find as they will cause less disruption in heat transfer near the soil surface. Further, surface roughness of the soil can create temperature differentials which can lead to a false positive detection of an object. To combat these problems using only passive infrared imaging, multiple scans would be required at different times of the day [16]. An alternative to rescanning is to instead provide heating with the system instead of relying on natural conditions to provide heat.

2.2.2 Active Thermal Imaging

The active thermal IR imaging approach has been applied in different ways. One system used 2.45 GHz microwaves at a power of 5 kW. The detection target used in this study was a large TM–62P3 landmine. Using this technique, detection could be reliably achieved in 30 seconds [17]. However, the large microwave source required would prevent this system's application to a small, portable system.

An alternative approach used high pressure, small diameter water jets heated to 50 degrees Celsius to provide heat to the area of interest. These jets were at pressures of 16 MPa, and were capable of penetrating the soil surface up to 15.2 cm. In areas with no buried object, a series of dots appears where the jets injected water in to the soil. When a device is present, however, the surface of the object radiates heat backward and has a multiplicative effect on the heat appearing at the soil surface, resulting in an image of the object at the soil surface when imaged in infrared. Unfortunately, this method requires detection times on the order of minutes [18].

Neither the active nor the passive thermal imaging method are suitable for this application. The use of the passive method would only allow detection at certain times of day, and also cannot detect deeply buried explosives. The active thermal approach does yield better results and could be used at any time, instead of at specific times, but either the power required to produce detection is too great for a portable system, or the detection time is too long. Hence, neither method is applicable to a portable system designed for road clearance.

2.3 Electrical Impedance Tomography (EIT)

In electrical impedance tomography, electrodes are placed on the surface at injection points which occur in a grid pattern. These measurements can then be used, along with the Poisson equation for continuously inhomogeneous media and inhomogeneous Neumann boundary condition, from which the electrical potential, surface current density, and impedance can be determined approximately. Buried objects

result in disturbances in the electrical impedance of the soil, and so a map of the electrical impedance of the soil can be used to locate buried objects.

To provide the map, low level electrical currents are passed through the electrodes in to the surrounding soil with which the electrodes are in surface contact. The soil is stimulated by applying voltages to pairs of electrodes, and the resulting voltages in remaining pairs of electrodes are measured. These measurements are then used to solve the boundary value problem, from which a map of conductivity can be obtained [19]. Both metallic and non-metallic then create disturbances in the electrical conductivity which appear as anomalies in the resulting electrical impedance map.

Detection of anomalies in the soil requires an electrode spacing that is 1.0 – 1.5 electrode spacings deep and at least 2 electrode spacings in size, and under these conditions detection can be reliably made. Moreover, good electrical contact is required between the surface probes and soil in question. This is difficult to obtain in arid soils with little moisture, as the water content aids electrical contact between the soil and probe. However, because moisture aids the EIT process, it can work in moist soils where methods such as metal detection fail [20]. This technique, as a result of the requirement that the electrode spacing be on the order of maximum detection depth and twice the size of the object means that objects buried 60 cm in depth would have to be 120 cm in size to be detected. This would mean that a 155 mm shell, at a length of 24 cm, would not be detectable by this system at depth. Moreover, the system considered in this dissertation is destined for the Middle East, an area which by nature has arid soils, and so an EIT-based detection system would be a poor choice for this area of deployment.

2.4 Nuclear Quadrupole Resonance

Unlike previous methods, nuclear quadrupole resonance (NQR) has a significant advantage over previously discussed methods of explosives detection. Rather than detecting anomalies in the ground or the presence of metals which may indicate the

presence of an explosive device, NQR detects the presence of specific elements, and thus is specific to the detection of the explosive itself, rather than characteristics of an explosive device. In theory, this should allow a lower false positive rate by not signalling on metal debris or other anomalies.

The technique itself relies on the splitting of nuclear spin states caused by the electromagnetic radiation's interaction with the nuclear charge density within the material in question. This interaction results in a flipped nuclear spin state, which then relaxes to the original state when electromagnetic field disappears, resulting in a signal characteristic of that element. The relaxation time of this spin state is of particular interest, since it is this time that determines how quickly a measurement may be repeated to reduce error. Multiple induction pulses may be sent out to reduce false positives, however the decay of the resultant signal is such that a long delay is required before the next pulse may be sent. In the case of TNT, this delay may be up to 30 seconds [21].

Detection largely relies on the existence of ^{14}N, as the other elements typically found in explosives do not produce a significant NQR signal [22]. This would preclude detection of peroxide-based explosives such as HMTD which do not contain nitrogen. More significantly, eddy currents induced in metallic casings of artillery and bombs, of which IEDs are often made, could create a significant background for the NQR signal. These casings can also shield the NQR signal altogether.

Most concerning, however, is the fact that most NQR signals, that generated by ^{14}N in particular, are in the range of several hundred kilohertz to several megahertz. This range is coincident with the AM radio band, which runs from 148.5 kHz to 26.1 MHz [23]. Since both transmitters and jammers along with plans for the same are readily available, it would be trivial for enemy personnel to completely interfere with NQR based detection of explosives should the basis of the technology ever be discovered. This, in combination with significant interference caused by the presence of a metallic casings makes the NQR technique unsuitable for the detection of improvised explosive devices in a hostile environment.

2.5 X–Ray Backscatter

At x–ray energies, three interactions are dominant, Rayleigh scattering, Compton scattering, and the photoelectric effect. For low Z materials, the photoelectric effect is dominant for energies < 50 keV. Between 60 and 200 keV, Compton scattering becomes important and backscatter reaches its maximum. Above 200 keV, Compton scattering is dominant [24]. The probability of photoelectric absorbtion is given by

$$\tau \propto \frac{Z^n}{E^3} \tag{2.1}$$

where n is a constant between between 3 and 5, depending on the x–ray's energy. The probability of Compton scattering per atom is given by

$$\sigma \propto \frac{Z}{E} \tag{2.2}$$

As a result, density related information can be derived from these interactions, as Z is directly proportional to electron density, which in turn is directly proportional to mass density [25]. Given the simple dependance on Z as well as the well known relationship that

$$E' = \frac{E m_e c^2}{m_e c^2 + E\left[1 - \cos\theta\right]} \tag{2.3}$$

and a monoenergetic source of x–rays, it is possible to get both density related information as well as determine the direction from which the scattered x–rays came using Compton scattering. Low effective Z materials will also have more x–rays available to Compton scatter, as the absorption probability is strongly Z dependant. Given that soil has an effective Z of approximately 11 and explosive approximately 7, explosives will preferentially backscatter compared to the soil [24].

However, this method is complicated by metallic explosives. As metals are generally higher Z materials, the x–rays will preferentially be absorbed by explosive casings. Additionally, given their relatively low energy, x–rays will be absorbed in

the soil with increasing depth. This will generally prevent the detection of explosives at greater burial depths.

Moreover, increasing depth also increases the chance that x–rays that do make it to the target area may encounter multiple scatters or also be reabsorbed as it traverses the soil back to the detector, which again will limit the useful signal produced by deeply buried explosives. For example, the common industrial isotopic source caesium-137 produces x–rays at 662 keV. At this energy, for world average soil at a density of 1.4 grams per cubic centimeter, the attenuation coefficient, λ, is 7.041×10^{-2} $\frac{\text{cm}^2}{\text{g}}$. The intensity is given by

$$I = I_0 e^{-\rho\lambda x} \tag{2.4}$$

So

$$\frac{I_0}{2} = I_0 e^{-\rho\lambda x_{\frac{1}{2}}}$$
$$\ln 2 = \rho\lambda x_{\frac{1}{2}}$$
$$x_{\frac{1}{2}} = \frac{\ln 2}{\rho\lambda}$$

resulting in a mean free path of 7 cm [26]. As the detector and source require and angled path through the material, detecting explosives at greater depths becomes all the more problematic. Assuming explosive at 15 cm and a 45 degree angle from the normal for the source, 21 cm of soil would be traversed. This would result in the attenuation of 88% of source x–rays before explosive was reached. As lower energy x–rays than 662 keV are commonly use to make differences due to photoeletric absorption more prominent, detection depth would be severely limited. Moreover, no direct measurement of Z can be made using this method, and so no specificity to explosives is provided by this technique. Given these limitations, x–ray backscatter is not a good candidate for a standalone detector for buried explosives.

2.6 Neutron Interrogation

Neutron interrogation falls into two general categories, fast neutron analysis (FNA) and thermal neutron analysis (TNA), or some combination of the two techniques as in pulsed fast neutron analysis (PFNA) or a refinement thereof such as the associated particle technique. These two techniques rely on two different types of reactions. Fast neutron analysis uses inelastic scattering events while thermal neutron analysis relies on thermal neutron capture. Both of these interactions produce gamma rays characteristic of the element with which the neutron interacted, which can in turn be used to identify a material using the spectrum produced.

Neutron interrogation has the advantage, along with nuclear quadrupole resonance, of providing a signal that is specific to the chemistry of the target interrogated, and not features of explosives such as the presence of metal or electronics, allowing for a reduction of false positives from debris. Further, since neutrons carry no charge, they are weakly interacting with common materials, allowing for significant penetration in common materials, thus allowing for non-destructive interrogation at greater depths than most other techniques.

Both techniques rely on the detection of elements contained by explosives, most commonly hydrogen, nitrogen, oxygen, and carbon. These elements produce spectra which are characteristic of each element. The detection of one of the elements singularly or a combination of the elements, especially in certain relative ratios, can then signal the presence of explosive in the environment. The presence of particular ratios of elements is of interest because explosives have characteristic ratios of these elements, since optimal energy release occurs when there is enough oxygen that every hydrogen atom forms a water molecule and every carbon atom forms carbon monoxide [6].

Element	Mass Percentage	(n, n') Threshold (MeV)
Al	8.2%	0.87
Fe	5.6%	0.87
Ca	4.2%	1.2
Mg	2.8%	0.6
Na	2.4%	6.46
K	2.1%	2.6

Table 2.1.
Inelastic scatter threshold energies for important constituants of soil [27]

2.6.1 Fast neutron analysis (FNA)

Fast neutron analysis is based on inelastic scattering of fast neutrons (neutrons having kinetic energies exceeding 0.1 MeV) off of nuclei in the target material. In this process, a fast neutron collides with a neutron, scattering off in a different direction with reduced energy. The energy lost excites the target nucleus resulting in an excited nuclear state, which then decays, releasing one or more gamma rays with energies dictated by selection rules. The emitted gamma rays have energies characteristic of each nucleus, and so a spectrum of energies of gamma rays results from neutron interrogation of a target material composed of one or more elements. Lines in the resulting spectrum can then be used to identify the composition of the target material. To examine the feasibility of this method, the constituents of explosives and their respective lines must be examined. From the discussion in the previous chapter, these include hydrogen, carbon, oxygen and nitrogen. The lines produced by inelastic scatter for these elements are the 4.44 MeV line for carbon, 6.13 MeV for oxygen, and 2.31 MeV for nitrogen. Hydrogen does not produce an inelastic scatter line [28]. While fast neutron analysis has been used successfully in the field of luggage screening and other related fields, IED detection presents a substantial challenge which the screening of luggage does not, the presence of a large quantity of parasitic material, namely the soil, that provides significant interference with the inelastic scattering lines which form the basis of fast neutron analysis.

This is particularly true in the case of oxygen. World average soil contains 48.87% oxygen by mass [29], making the possibility distinguishing the presence of oxygen from explosive from background oxygen unlikely. The presence of oxygen also presents a problem for the use of carbon and its characteristic 4.44 MeV inelastic scatter line. Instead of inelastic scattering, oxygen may also participate in a ^{16}O(n, α) reaction, leaving an excited ^{12}C nucleus, which may then decay by releasing a 4.44 MeV gamma, as in an inelastic scattering reaction. This effect is strong enough to completely mask the presence of carbon from an explosive [30]. As a result of the natural abundance

of oxygen in soil, neither oxygen nor carbon lines provide of useful signature for the presence of explosive.

The only remaining candidate element for use with fast neutron analysis is then nitrogen. Unfortunately, the nitrogen line occurs very close to the thermal neutron line produced by hydrogen, which will provide a strong source of interference given the presence of hydrogen in the soil at an average percentage by number of 25%. Nitrogen also produces another strong line at 5.31 MeV without any significant background interference from soil, however the cross section of 42.4 mb is 43.4% smaller than the 75 mb thermal capture cross section of ^{14}N [31]. Moreover, as the neutrons produced by the generator traverse the soil, they may participate in a number of reactions which will result in a loss of energy. As a result as neutrons penetrate deeper and deeper in to the soil, their average energy will decrease, leaving fewer and fewer neutrons available to participate in an inelastic scatter with nitrogen. Neutron capture, the reaction that serves as the basis of thermal neutron analysis, by contrast, will become more likely with decreasing energy and has a larger cross section. Hence, for the identification of explosives within soil, thermal neutron analysis is the better choice.

2.6.2 Thermal neutron analysis (TNA)

Thermal neutron analysis is based on thermal capture of neutrons by target nuclei, which produces an excited state which then decays by emission of gamma rays characteristic of the element with which the neutron reacts. As with fast neutron analysis, the elements of interest for the detection of explosives are oxygen, hydrogen, nitrogen, and carbon. As before, neither hydrogen nor oxygen's lines can serve as an indicator of explosive, as soil contains a high percentage of either element, leaving nitrogen and carbon as the only elements of interest for the detection of explosives in soil.

As with fast neutron analysis, however, carbon is not useful for the detection of explosives. The two natural isotopes of carbon, ^{12}C and ^{13}C, both have small thermal

capture cross sections of 0.34 mb and 0.14 mb, respectively [31]. The three strong lines produced by ^{12}C occur at 1.261 MeV, 3.683 MeV, and 4.945 MeV. The 1.261 MeV line is not useful because it is quite close to a line produced by ^{29}Si at 1.263 MeV. The line at 3.683 MeV has no significant naturally occurring background from any particular element, however this energy is within the range where Compton scattering is the dominant energy loss mechanism of gamma rays within the detector material, which results in a strong continuum background. Given ^{12}C's small capture cross section and the large background produced by Compton scattering, this line is of limited use for explosives detection. The 4.945 MeV line does have a background at 4.933 MeV produced by ^{28}Si. The only strong line produced by ^{13}C occurs at 8.174 MeV. While this line does not have any significant background, the isotopic abundance of ^{13}C is quite low at 1.07%. Given the combination of a low isotopic abundance and a small capture cross section, the 8.174 MeV line produced by carbon-13 will also be unlikely to serve as a useful indicator of the presence of explosive [32].

The remaining element of interest is then nitrogen, which has two stable isotopes, ^{14}N and ^{15}N, though the isotopic abundance of ^{15}N is small at 0.364%, and further has a small capture cross section of 0.00241 mb, and so is not of interest as an explosive signature. Nitrogen-14, however, has a capture cross section of 75 mb which produces its strongest lines at 1.884 MeV, 3.677 MeV, 4.508 MeV, 5.269 MeV, 6.322 MeV, and 10.829 MeV [32]. None of these lines have significant sources of background, outside of the Compton continuum, which is often a considerable source. However, the 10.829 MeV line is within the range of energies where the Compton continuum is small as a result of pair production being the dominant energy loss mechanism for gamma rays of that energy and further has the advantage of being the most energetic gamma ray produced by thermal capture on naturally occuring elements. The only significant background is the relatively weak 10.6 MeV line produced by ^{29}Si, which only has an isotopic abundance of 4.685% and a capture cross section of 120 mb. The 10.8 MeV line is thus preferable to the other lines produced by nitrogen as it should have a low

background compared to the other lines which fall within the Compton continuum and will serve as the basis of the detection of explosives.

3. Introduction to MCNP5

MCNP5 will be used to simulate the ground, explosives, and detectors to determine the efficacy of the designed system. MCNP uses the Monte Carlo method to simulate the transport of neutrons, electrons, and photons. The program can be set up to transport either each type of radiation by itself, or any combination of 2 or more of the possible types [33].

3.1 The Monte Carlo Method

The Monte Carlo technique uses repeated random sampling to compute some result. One historical example of an application of the Monte Carlo technique involves a technique proposed by George-Louis Leclerc and Comte de Buffon to estimate the value of pi. The method employed involved dropping sticks of known length on to a plane surface on which parallel lines had been arranged such that the lines were spaced a distance equal or greater than the length of the sticks. The probability a stick would land on the cut could then be expressed as

$$P_{\text{cut}} = \frac{2L}{\pi D} \tag{3.1}$$

By repeatedly dropping sticks on the plane, an estimate of P_{cut} can be obtained, since probability of an event occuring is defined as

$$P = \lim_{n\to\infty} \frac{N}{N_t} \tag{3.2}$$

where N is the number of trials which result in the event, and N_t is the total number of trials. If n_c is the number of trials in which the stick lands on one of the line segments, and n_t is the total number of trials,

$$P_{\text{cut}} \approx \frac{n_c}{n_t} \tag{3.3}$$

This estimation of the probability can then be used to estimate the value of pi by solving Eq. 3.1, so that

$$\pi = \frac{2L}{P_{\text{cut}} D} \approx \frac{2L}{\frac{n_c}{n_t} D} \tag{3.4}$$

The statistical process of dropping stick is thus used to obtain an estimate of the value of pi [34].

3.1.1 Particle Transport

The transport process of neutral particles such as gamma rays and neutrons is likewise a statistical process which can be estimated using Monte Carlo techniques. For example, given the macroscopic cross section

$$\Sigma_T = \sum_j \rho_j \sigma_{T,j} \tag{3.5}$$

where $\sigma_{T,j}$ is the total cross section of the jth atomic species of the material and ρ_j its density, the probability of interaction for $0 \leq x \leq \infty$ is given by

$$f(x) = \Sigma_T e^{-\Sigma_T x} \tag{3.6}$$

and the probability of having interacted after a distance x is

$$F(x) = 1 - e^{-\Sigma_T x} \tag{3.7}$$

the distance travelled before interaction can then be sampled by using a random number, ξ, and solving for the distance travelled, x

$$x = -\frac{ln(1-\xi)}{\Sigma_T} \tag{3.8}$$

by repeatedly sampling x, the average distance travelled and other quantities can then be estimated.

In addition to travelled distance, colliding isotope is also important for transport. The probability of interacting with isotope j is given by

$$p_j = \frac{\rho_j \sigma_{T,j}}{\sum_i \rho_i \sigma_{T,i}} \tag{3.9}$$

As these are discrete values, a table lookup is used to sample these. A random number ξ is generated. The colliding isotope j is that which satisfies $P_{j-1} \leq \xi \leq P_j$ where

$$P_j = \sum_{i=1}^{j} p_i \tag{3.10}$$

where p_i is the probability of interacting with the ith isotope given by

$$p_i = \frac{\rho_i \sigma_{T,i}}{\sum_l \rho_l \sigma_{T,l}} \tag{3.11}$$

Given the selected isotope, the reaction on that isotope must be selected among the n possible reactions types. Similar to the calculation determining isotope with which to react,

$$\sigma_T = \sum_n \sigma_n \tag{3.12}$$

and the probability of the jth reaction type is

$$p_n = \frac{\sigma_{i,n}}{\sigma_T} \tag{3.13}$$

The jth reaction type is then selected if the value of

$$P_j = \sum_i p_i \tag{3.14}$$

is such for a randomly generated number ξ, $P_{j-1} \leq \xi \leq P_j$. Once this is completed, the outgoing energy and direction must be computed. The method of doing this is reaction type dependant [35].

MCNP and Histories

For each particle generated by the source, MCNP follows the above method, tracking the movement of the particle in what is called a history. Cells are defined using conical mathematically defined surfaces. As each particle traverses the problem space, a determination is made if an interaction occurs within the current cell by calculating the distance to the exit point in the cell. If an interaction is not made within the

remaining distance travelled through the cell, then that particle does not interact with the current cell and instead moves in to the next cell.

In the next cell the process is repeated. If the particle does interact, its new energy and direction are computed and the process repeats again. If secondary particles are generated, they are tracked through the problem space with their own history. The history of the particle is terminated when the particle is absorbed, or when the particle enters a cell with an importance set to zero for that particular particle type. Cells of zero importance mark the extent of the problem space.

This process is repeated, typically for a defined number of particles, and then the run is terminated [36].

3.1.2 MCNP Problem Definition

Simulations are entered in to MCNP using what are referred to as decks. These decks include cell, surface, and data cards.Cells define the problem's volume. For example, the interior of a sphere of 100 cm radius may be chosen to be a cell within the simulation. These cells are defined by the surface cards, which consist of mnemonics for various surface equations, such as $PZ1$ for a plane defined by $z = 1$. By combining these surfaces and indicating the sense of the surface for a given cell, cells may be defined using the surfaces entered in the deck.

The data card then define the other information about the problem. Examples of the data cards include the source definition card. This card defines the source particle type as well as its distribution. The default is a point source at coordinates which are set by the user in this card. The importances of cells are also defined within the data cards, which determine how particle transport will proceed, or if transport will terminate all together in the case that the cell importance is zero.

Tallies are also defined by the data cards. Tallies are what is used to generate physically meaningful data, such as a surface flux. These cards define parameters of the tally, such as for the surface flux what surface the flux is to be collected on.

Tallies can also be binned. The most common bin would be an energy bin so that energy spectrum associated with a given particle can be seen on a defined surface. Cosine bins can also be used to split the flux in to angular information, such as counting only particles moving upward. Tallies, with the exception of the F8 energy deposition tally, can also be binned by time. This allows the flux to be split up in the time domain, and used to account for things such as a detector being gated off [36].

3.1.3 MCNP Limitations

While a respected and time tested software package, MCNP5 does have limitations. In terms of the simulations required, the most significant of these is the inability to perform an F8 energy deposition tally, normally used to simulate detector response, with time binning. The use of pulsed mode operation, that is gating off the detectors during a neutron pulse followed by a period without neutron production with the detectors gated on, would require time binning during an F8 tally for the most accurate representation of the detectors' response.

However, as this is an impossibility, an alternate simulation technique was developed wherein a surface tally was taken with time bins in place over the surfaces of the detector array. A series of simulations was then conducted with a pure gamma ray source of energies between 0 and 11 MeV were placed in varying positions and angles of incidence on the detector surface. The results, with energy broadening applied, were averaged across these positions and locations at each bin energy from the primary simulation. This allowed an estimate of the signal after time binning was applied.

A second major limitation is the inability to account for the background produced by the radioisotope ^{128}I which is produced as a result of the capture of neutrons on ^{127}I. This would require knowing the energy captured as the 6.8 MeV photons produced by decay traverse the detectors during the period in which the detectors are gated

on, which would again require an F8 tally with time binning, which is unsupported in MCNP5.

The final significant limitation is that of available soil data. There is little detailed elemental analysis of soil available for different regions, and so accounting for potential variation caused by regional soil variation is difficult absent this data.

4. Source Selection

4.1 Types of Neutron Sources

The two types of sources include radioisotopic sources, such as Cf-252, which produce neutrons through the spontaneous fission, sources based on the (α, n) reaction, and fusion based sources which use fusion reactions which produce neutrons as a product.

4.1.1 Radioisotopic Sources

Californium-252

Californium-252 decays both by spontaneous fission (3.09% probability) and alpha emission (96.91% probability) with a half life of 2.645 years. Its neutron emission rate is 2.314×10^{6} s^{-1} μg and a specific activity of 0.536 mCi μg. ^{252}Cf does not produce monoenergetic neutrons, instead producing a Maxwellian energy spectrum, given by

$$N(E) \propto \sqrt{E}e^{-\frac{E}{T}} \tag{4.1}$$

which yields an average energy of 2.1 MeV and a most probable energy of 0.7 MeV [37]. The density of ^{252}Cf is 15.1 g cm^{-3}. To obtain a neutron production rate of 3×10^{8} s^{-}1, a rate comparable to typical DT fusion sources, a volume of only 8.6×10^{-6} cm^{3} of californium would be required, allowing for a very compact source. The cost of these sources is \$60 per microgram, meaning that to obtain a neutron production rate comparable to that of available DT fusion sources, 129 μg would be required at a cost of \$7,800 [37], so a ^{252}Cf source would also be a low cost, compact, and low maintenance option. However, since the source is based on spontaneous fission, it may not be deactivated, and so would require bulky shielding, present a radiation

safety hazard, and prevent pulsing of the source to reduce the background of the thermal capture lines of interest. Further, ^{252}Cf also produces 8 gamma rays for every 4 neutrons produced, and so would also present a considerable increase in the gamma ray background [38, 39].

4.1.2 Fusion Sources

In fusion sources, deuterons are accelerated to an energy sufficient to overcome the Coulomb barrier and strike a target containing light nuclei, typical deuterons or tritons. The fusion reactions that result produce neutrons as a product of the reaction. The two major types of commercially available neutron generators utilize DD and DT fusion reactions. These sources utilize a linear accelerator to accelerate a beam of particles through a potential of 100 keV. The particles then strike a metal hydride target which has been loaded with tritium and deuterium, in the case of a DD generator, or deuterium in the case of a DD generator. The DD reactions produces a 2.5 MeV neutron while that of the DT generator produces a 14.1 MeV neutron.

These types of sources provide the advantage that they can be turned on and off by activating and deactivating the beam of incoming particles. As a result, they do not present a safety threat when not in use, and more importantly can be used in a pulsed mode. Pulsed mode operation allows the collection of gamma ray spectra in the detectors during the generator's off cycle. This can allow fast neutrons to die away so that the spectra being collected are predominately thermal neutron reactions. As a result, the background to the signal can be significantly reduced in the case of thermal neutron reactions, as radiative inelastic scatter reactions no longer contribute to the spectrum, thus reducing the background considerably.

4.1.3 Source Type Selection

Given the selection of thermal neutron analysis, the neutron source then had to be selected. The types of sources considered include a ^{252}Cf radioisotopic source, a DD

fusion-based source, and a DT fusion–based source. Ultimately, a DT neutron generator was selected because of safety and physics considerations that will be discussed later.

Radioisotopic sources were rejected because it is not possible to deactivate these sources since they produce neutrons using spontaneous fission. Because of this shortcoming, these sources may not be pulsed, and so a significantly higher signal to noise ratio results from their use. Furthermore, since this system is destined for use around civilians and for use by those with little or no radiation safety training, it is preferable to have a source that can be turned off to limit incidental exposure.

4.2 Source Optimization

Of the two remaining candidates, generators based on DD or DT fusion, MCNP and practical considerations were used to select a source. For our purposes, the best performer is the source which produces the most thermal neutrons per starting neutron at each depth. The production of thermal neutrons at 10 cm depth intervals was simulated. In the simulation, a cube 1 m on side of air was placed above a 10 cm thick plane of concrete. Below the concrete plane, a cube 1 m on side sample of pure quartz sand was placed which contained 10% moisture. This configuration can be seen above in Fig. 4.1. In the following discussion, the reflector thickness will refer to the difference between the inner radius of the reflector, defined by the neutron generator tube, and the outer radius of the reflector. Length refers to the extent of the reflector along the axial direction. Then, the number of thermal neutrons crossing the boundaries between successive 10 cm thick soils was tallied using an F1 tally, starting at the concrete–soil interface. The F1 tally computes the number of particles crossing a particular surface and is defined by

$$F1 = \int_{E_i} dE \int_{t_j} dt \int_{\hat{\Omega}_k} d\hat{\Omega} \int dA \left| \hat{\Omega} \cdot \hat{n} \right| \nu n(\vec{r}, \hat{\Omega}, E, t) \tag{4.2}$$

All fit data was taken from the tally at 20 cm depth to allow for the effects of both the concrete surface and soil to be taken into consideration.

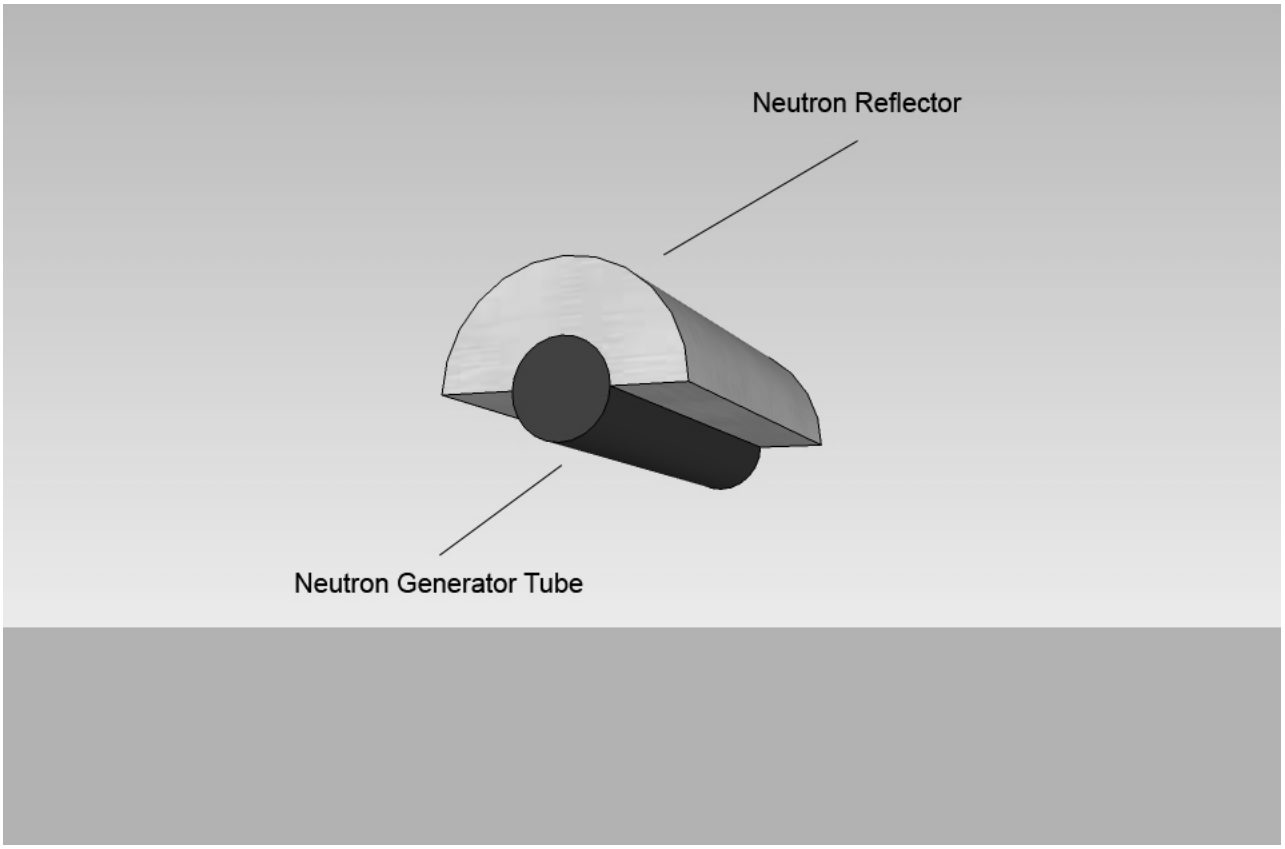

Figure 4.1. Geometry of the neutron reflector.

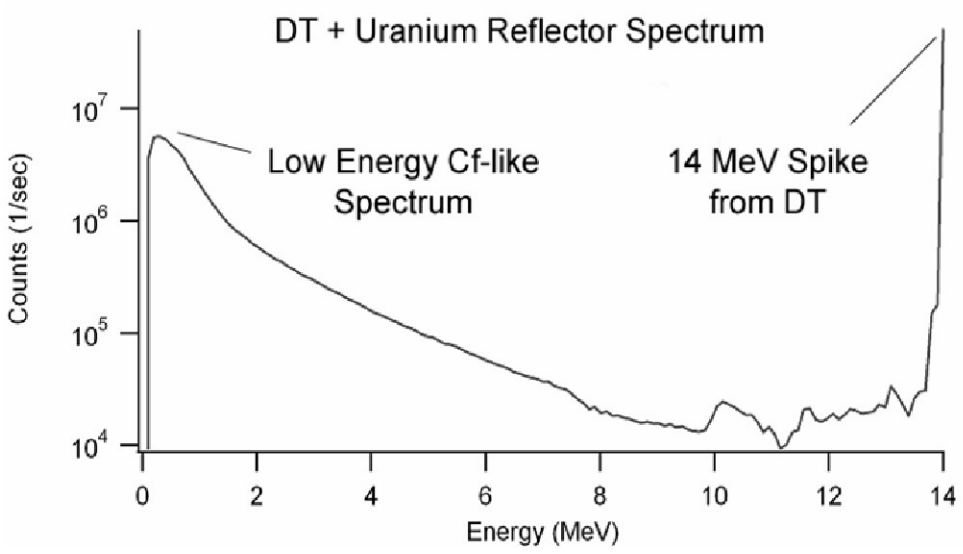

Figure 4.2. Neutron energy spectrum of a DT generator coupled to a depleted uranium reflector.

In addition to testing the bare sources, it was also desired to test the effects of a neutron reflector. Both lead and depleted uranium were used as test materials in both cylindrical and hemispherical configurations. Lead was selected for its naturally occurring isotopes' large (n, 2n) cross section at 14 MeV. Depleted uranium was also chosen for its large (n, 2n) cross section at the same energy, but in addition it also has large fission and (n, 3n) cross sections. The purpose of these reflectors is to both multiply the number of neutrons emitted and produce a neutron energy spectrum comparable similar to the Watt spectrum produced by ^{252}Cf, as shown in Fig. 4.2. This is advantageous because the higher energy 14 MeV neutrons will take more soil depth to thermalize than lower energy neutrons, and so provide fewer thermal neutrons at the soil surface, decreasing near surface bulk elements' signal. If a portion of the neutron energy spectrum is lower in energy, more thermal neutrons will be produced at or near the soil surface than in the case of a bare neutron source, resulting in more capture reactions.

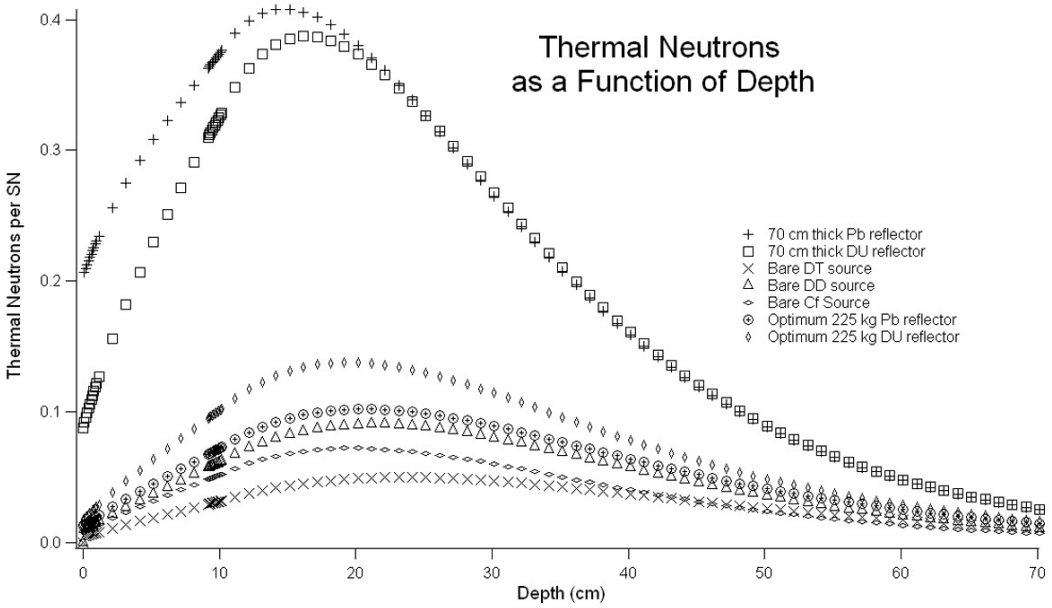

Figure 4.3. Thermal neutron population as a function of depth for various source type and reflector combinations.

4.3 Reflector Effects

The general trend of neutron behaviour in soil can be seen from from Fig. 4.3. Two competing effects determine the number of thermal neutrons available for capture reactions at each depth in soil. The first of these is the thermalization of higher energy neutrons. Because soil and concrete both contain hydrogen and other light elements, they act as moderators, and so increase the number of thermal neutrons by decreasing the energy of incoming neutrons through scattering. While the production of thermal neutrons occurs at all levels within the simulation, there is an additional competing effect, neutron absorption, which decreases the number of thermal neutrons available. At first, there are more thermal neutrons produced than are being absorbed by elements within the sample, and so the number of thermal neutrons increases. At some point, the neutron absorption rate exceeds thermalization rate, and the number of thermal neutrons decreases. At what depth this occurs depends on the average

energy of the incoming neutrons. The higher the average neutron energy, the deeper in soil this maximum occurs.

The advantage of the reflector can also be seen in Fig 4.3. The depth at which the maximum number of thermal neutrons occurs, without regard to the absolute number of neutrons, is much shallower for the DT generator and reflector combination (15 ± 1 cm), than for either a bare DD neutron generator (21 ± 1 cm), or a DT generator (24 ± 1 cm). The saturated reflector also generates more thermal neutrons at each depth than either source alone, producing a maximum of 0.4076 ± 0.00012 thermal neutrons per starting neutron, as compared to 0.09047 ± 0.000054 for a DD source and 0.049879 ± 0.000040 for a DT source. By producing more thermal neutrons at each depth, a DT source coupled to a reflector produces many more capture reactions than the DT or DD source alone.

4.4 Reflector Design

The next step in developing a neutron reflector is to decide on the dimensions of that reflector. Because the reflector will be placed on a portable system, its mass must be limited. It is assumed that the cart for deployment will have a similar size and class of motor as that of a typical utility golf cart. Typical utility carts have a maximum carrying capacity of a 450 kg. Since other equipment will need to be carried, half the carrying weight will be allotted to the reflector, meaning the reflector mass is limited to 225 kg. To determine the optimum reflector with this fixed mass, simulations were conducted with MCNP. Since the neutron generator has a cylindrical shape, the shape of the reflector will also be cylindrical, with a 6 cm radius half cylinder hollow removed from the center of the half cylinder reflector to accommodate the neutron generator.

For the purposes of the simulating the reflectors, the 14 MeV point source was placed centered on the cylinder axis, flush with the surface of the reflector. The source was placed 10 cm above the concrete surface. Depths are measured from the top of

the concrete surface, so that the air–concrete interface is at 0 cm, the soil–concrete interface is 10.16 cm, and the bound of the problem space is at 70 cm. Hereafter, length shall refer to the length of the cylinder along its axis, and thickness shall refer to the difference between the radius of the neutron generator channel and the outer radius of the reflector.

4.4.1 Simulation Fit Equations

It is assumed that the reflector length will control only the probability that the neutrons strike the reflector, while the thickness, will determine the probability that the neutrons interact with the reflector material. Under this assumption, it is presumed that the neutron production data can be fitted to a function with two independent terms, one relating to the solid angle of the reflector, a function of length, and the other relating to the interaction probability, a function of thickness.

The total neutron population data can then be fitted to a combination of these two terms, with addition of two parameters. The two fit equations represent the probability of interaction, and so must be multiplied together to obtain the total probability of interaction. This total probability is then multiplied by the number of thermal neutrons produced by an infinite reflector. An additive constant must then be added to the fit function to account for thermal neutrons produced by the source in the absence of the reflector.

It is presumed that the thickness will control the probability of interaction. As neutrons enter the reflector material, they react with its nuclei. The number of neutrons which have interacted with the reflector is determined by the number of remaining neutrons, N, which have not interacted with the reflector and the distance travelled through the material, x. A differential equation then arises of the form of Eq. 4.3, given below.

$$\frac{dN}{dx} = \frac{-N}{\lambda} \tag{4.3}$$

The solution to this equation is given by

$$N = N_0 e^{\frac{-x}{\lambda}} \tag{4.4}$$

However, the number of interest is the number of neutrons which have interacted with the reflector, N_r, given by Eq.4.5.

$$N_r = N_0 - N(x) = N_0 \left(1 - e^{\frac{-x}{\lambda}}\right) \tag{4.5}$$

This is the function that will be used to fit the thickness data.

The functional form of the length fit is determined by the solid angle that the reflector presents. This is found using a spherical coordinate system, with the source at the origin. The reflector is placed with its axis of symmetry along the z axis, with its length centered on the xy plane. Since the reflector is a half cylinder and the reflector has its axis on the z axis, the azimuthal angle varies from 0 to π.

The polar angle extremes of the reflector are determined by the length of the reflector. Let r_0 be the perpendicular distance from the source to the surface of the cylindrical reflector and L the total length. The angle from the top of the reflector to its center, α, is then given by Eq. 4.6.

$$\alpha = \arctan\left(\frac{\frac{L}{2}}{r_0}\right) \tag{4.6}$$

The solid angle of the reflector as viewed by the source is then given by Eq. 4.7. The data produced by MCNP simulations will be fitted to this function.

$$\Omega(L) = \int_{\alpha-\frac{\pi}{2}}^{\alpha+\frac{\pi}{2}} \sin\phi d\theta d\phi = 2\pi \sin\alpha = 2\pi \sin\left[\arctan\left(\frac{L}{2r_0}\right)\right] \tag{4.7}$$

If the two parameters' effects are assumed to be independent, then the probability that the neutron strikes the reflector (event A) and interacts (event B), is $P_{total} = P_A P_B$. From the forms derived above, the probabilities are given below by Eqs. 4.8 and 4.9.

$$P_A = \frac{1}{2} \sin\left[\arctan\left(\frac{L}{2r_0}\right)\right] \tag{4.8}$$

$$P_B = 1 - e^{\frac{-x}{\lambda}} \tag{4.9}$$

The combination of these two equations then yields the final fit function, Eq. 4.10, where n_0 is the maximum number of thermal neutrons produced by the reflector, and n_b is the number of thermal neutrons produced by the source in the absence of the reflector.

$$n(x, L) = n_0 \sin\left[\arctan\left(\frac{L}{2r_0}\right)\right]\left(1 - e^{\frac{-x}{\lambda}}\right) + n_b \tag{4.10}$$

4.4.2 Reflector Thickness Fit Data

The first MCNP simulation conducted varied the thickness of the reflector. Length was held fixed at 2 meters so that $\frac{L}{2} \gg r_0$ to approximate an infinitely long reflector. The thickness of the reflector was then varied from 1 to 70 cm. The source and reflector were placed 10 cm above the surface of the concrete. The results of this simulation are plotted in Fig. 4.4. The concrete road surface occurs at depths between 0 and 10 cm, and the soil extends from 10 cm to 110 cm. All fit data was taken at 20 cm depth to allow the 14 MeV neutrons to be affected by the concrete and soil. This depth is of the order of the mean free path of the 14 MeV neutrons.

Once the simulations were finished, the thickness data was fit to the presumed form, given by Eq. 4.11. The n_0 parameter reflects the maximum number of thermal neutrons produced by the reflector, and nb the number produced in the absence of the reflector. Fit parameters are given in Table 4.1.

$$n(d) = n_0\left(1 - e^{\frac{-d}{\lambda}}\right) + n_b \tag{4.11}$$

Three important conclusions may be reached from this graph and fit. The first of these is that fit equation is valid since the fit produced is very good as shown by Fig. 4.4. The second is that the lead reflector has the potential to generate more thermal neutrons per source neutron at depth than the uranium reflector. Taken to infinite thickness, the lead reflector would produce 0.492 ± 0.0043 thermal neutrons per source neutron at 20 cm depth, whereas the uranium reflector would produce 0.3979 ± 0.00054 thermal neutrons per source neutron at the same depth. Finally, the characteristic length controlling thermal neutron production is smaller for the

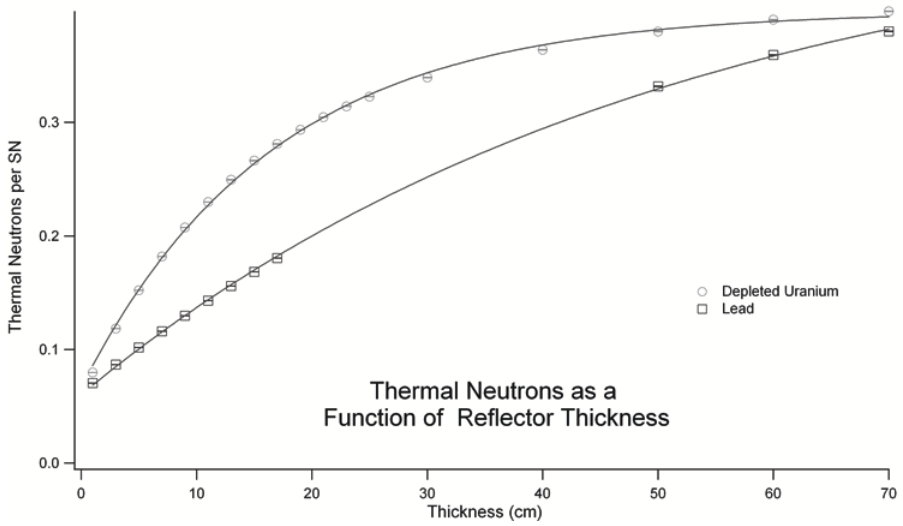

Figure 4.4. Thermal neutron population length fit for lead and depleted uranium reflectors.

Fit Parameter	Lead Reflector Values	Uranium Reflector Values
n_0	0.432 ± 0.00163	0.3314 ± 0.00037
λ(cm)	51.2 ± 0.456	16.58 ± 0.0403
n_b	0.060 ± 0.00399	0.0665 ± 0.000394

Table 4.1.
Fit parameters for lead and uranium thickness fit.

uranium reflector by a little more than a factor of 3. This is of considerable importance if the weight of the reflector is of practical importance, since weight of the reflector will go as thickness squared. By having a smaller characteristic length, the uranium reflector will produce more thermal neutrons at practical weights than a lead reflector will, making the depleted uranium reflector the better choice.

Fit Parameter	Lead Reflector Values	Uranium Reflector Values
c_0	0.06703 ± 0.00092	0.1419 ± 0.00098
r_0 (cm)	18.8 ± 0.56	16.7 ± 0.24
c_b	0.026 ± 0.0010	0.022 ± 0.0011

Table 4.2.
Fit parameters for lead and uranium length fit.

4.4.3 Reflector Length Fit Data

The next step was to determine the number of thermal neutrons per starting neutrons as a function of length. For this simulation, the reflector was kept at a fixed thickness of 12.7 cm. This thickness is roughly two mean free paths for neutron production in depleted uranium and one mean free path in lead. Length was varied from 5.4 cm to 95 cm. The data was then fitted using the fit function in Eq. 4.12. This fit equation reflects the solid angle of the reflector. Fit parameters can be found in Table 4.2. Again, the presumed fit function is validated by a high quality fit.

$$c(L) = c_0 \sin\left[\arctan\left(\frac{L}{2r_0}\right)\right] + c_b \tag{4.12}$$

4.4.4 Fixed Mass Reflector Fit Data

Given the validity of the fit functions, the reflector performance can be optimized using the fit equation for both length and thickness at a fixed mass of 225 kg. Given this fixed weight, reflectors of varying lengths and a constant mass were simulated in MCNP, in both lead and depleted uranium. The results of these simulations are shown in Fig. 4.6. The depleted uranium reflector was the best performer, with a maximum of 0.1375 ± 0.00049 thermal neutrons per source neutron at a 30 cm long and 6.7 cm thick. The data was fit to Eq. 4.13, which is Eq. 4.10 modified to account

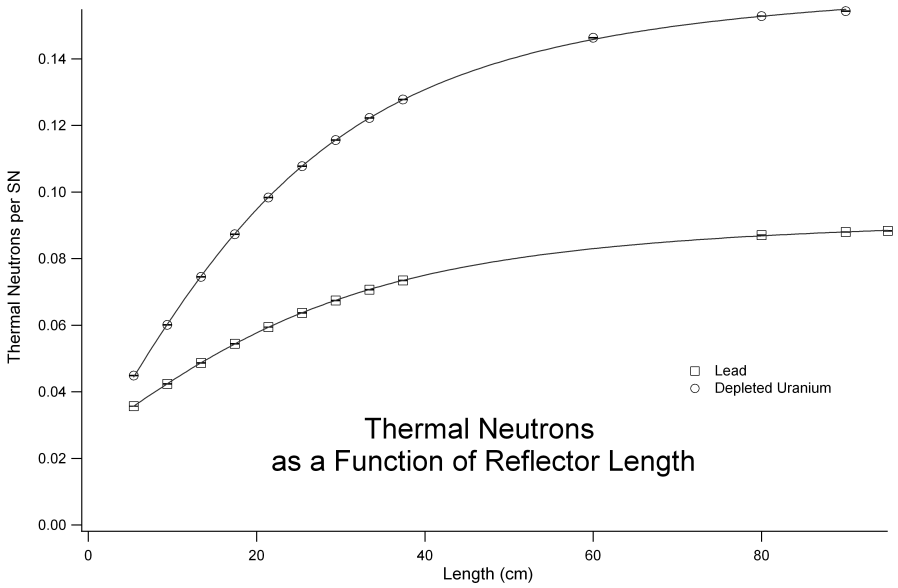

Figure 4.5. Thermal neutron population length fit for lead and depleted uranium reflectors

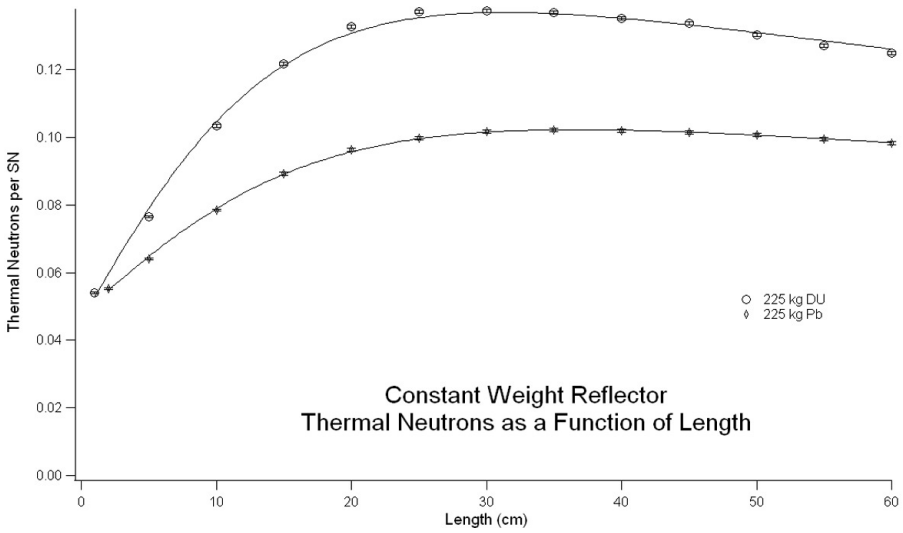

Figure 4.6. Thermal neutron population fixed mass fit for lead and depleted uranium reflectors.

for the dependence between length and thickness at fixed mass. Fit parameters are given in Table 4.3. Lead produced at maximum 0.1022 ± 0.00041 thermal neutrons per source neutron at a 35 cm long and 8.7 cm thick. The bare DT source provides 0.049846 ± 0.00004 thermal neutrons per source neutron, so the depleted uranium and lead reflectors provide 2.8 and 2.1 times the thermal neutrons at depth than a bare source.

$$n(L) = n_0 \left(1 - e^{\frac{\sqrt{\frac{m}{\rho \pi L}} - r_{in}}{\lambda}}\right) \sin\left[\arctan\left(\frac{L}{2r_0}\right)\right] + n_b \tag{4.13}$$

4.5 Source Selection

Given that radioisotopic sources are unacceptable, the best fusion-based source must be selected based on performance. Two considerations must be made when selecting the source, signal strength and background noise. While the top layer of

Fit Parameter	Depleted Uranium Values	Lead Values
n_0	0.15 ± 0.0178	0.084 ± 0.013
λ (cm)	7.1 ± 1.17	5.6 ± 1.36
r_0 (cm)	11 ± 1.15	12 ± 1.88
n_b	0.04595 ± 0.00313	0.0480 ± 0.000311

Table 4.3.
Fit parameters for lead and uranium constant mass fit.

material may or may not contain a target material, because it is close to the detectors and neutron generator, it will always provide a significant source of noise.

This is particularly true in the modelled concrete surface, which contains 31% by weight silicon (nitrogen's primary background) [40], and is not expected to contain target material. To make the system sensitive to deeply buried targets, the thermal neutron population must be minimal near the surface, and increase with depth.

While it is desirable for the thermal neutron population near the soil surface to be minimized, this must be balanced by the need to produce thermal neutrons within a target material which may be buried at any depth. Should the material be near the surface, detection should still be possible even with a small number of thermal neutrons since the gamma rays produced are close to the detectors and do not pass through a large amount of material that would otherwise attenuate the signal.

That the thermal neutron production must be biased towards greater depths is especially true when gamma ray propagation is taken into account. The gamma rays produced will spread isotropically from the point of production, and so the number of gamma rays reaching the detectors goes as $\frac{1}{r^2}$. Moreover, the gamma rays can interact with the soil or concrete. In soil, the energy loss mechanism is dominated by pair production accounting for 83% of the interactions, with Compton scattering providing the balance. In concrete, roughly two thirds of the energy is lost by Compton scattering and the remainder is lost through pair production [26]. Either loss mechanism will reduce a gamma ray's energy enough to remove it from the signal energy region in one interaction. Between geometric effects and soil interaction, the expected signal produced by a deeply buried target will be much weaker than a comparable target near the surface.

Because of attenuation by soil and geometric effects, it is more important for the source to generate thermal neutrons far from the soil surface than it is to produce thermal neutrons near the surface to maximize the gamma ray signal at depth and minimize the noise. The optimal source, then, is the one which provides the fewest thermal neutrons near the surface while maximizing the number of thermal neutrons

far from the surface. To compare the various sources, two weighted averages will be taken of the thermal neutron population at depths between 0 and 70 cm.

The first of these averages emphasizes the thermal neutron population near the soil surface. This is accomplished by using the expected attenuation from both soil interaction and geometric effects as a weighting factor. Since the expected attenuation from both effects is given by $w_{i,NS} = \frac{1}{d_i^2} e^{\frac{-d_i}{\lambda_i}}$, where d_i is the depth of the thermal neutron population in question, and λ_i is the gamma ray mean free path of the material at depth d_i. This weighting factor becomes large at the surface, and decreases considerably with depth, so this weighting factor will emphasize near surface thermal neutron populations. The average is given by Eq. 4.14, where n_i refers to the number of thermal neutrons per source neutron at depth d_i.

By combining these two weighted averages, the optimal source may be identified. As previously stated, the best source will produce more thermal neutrons far from the soil surface, and fewer thermal neutrons near the soil surface. This can be identified mathematically by taking the ratio of the far surface average population to the near surface average population. The source with the highest ratio is then the one which produces the most thermal neutrons far from the surface, and the least thermal neutrons close to the surface, and hence maximizes the signal to noise ratio.

$$\langle n_{NS} \rangle = \frac{\sum_i n_i \frac{1}{d_i^2} e^{\frac{-d_i}{\lambda_i}}}{\sum_i \frac{1}{d_i^2} e^{\frac{-d_i}{\lambda_i}}} \tag{4.14}$$

$$\langle n_{FS} \rangle = \frac{\sum_i n_i d_i^2 e^{\frac{d_i}{\lambda_i}}}{\sum_i d_i^2 e^{\frac{d_i}{\lambda_i}}} \tag{4.15}$$

Based on this optimization, the best source is a DT generator without a reflector, which provides the best ratio. The reason for this can be seen in Fig. 4.3. With the exception of the 70 cm thick reflectors, the different source types have very similar behaviour at 40–50 cm depth. However, near the surface their behaviour is very different. The sources with a lower energy spectrum produce the maximum number

Source Type	$\langle n_{FS} \rangle$	$\langle n_{NS} \rangle$	$\frac{\langle n_{FS} \rangle}{\langle n_{NS} \rangle}$
Bare DT	0.0303	0.00554	5.48
Bare DD	0.0473	0.0109	4.33
Optimum Pb + DT	0.0543	0.0127	4.27
Optimum DU + DT	0.0682	0.0173	3.96
Bare ^{252}Cf	0.0348	0.00905	3.85
70 cm thick DU + DT	0.156	0.0881	1.77
70 cm thick Pb + DT	0.159	0.210	0.755

Table 4.4.
Simulation results of near to far surface average thermal neutron population for various source types.

of thermal neutron nearer to the surface than the higher higher energy DT source, and the maximum number of thermal neutrons produced at that maximum is much larger than the DT source. By producing more thermal neutrons near the surface, more background will be created as this excess of thermal neutron captures on the near-surface elements within the soil or the concrete, and unless the source is very close to the surface, a comparable gain in signal from the detection target will not be achieved. So, the lower energy source will not provide the signal significance that the DT source will provide. Of the sources, the worst performer is the 70 cm thick lead reflector, which produces considerably more thermal neutrons within the concrete or surface than any other source. Based on performance, the DT source is the best available, however there are other considerations that must be considered when selecting a source.

Principle among these is safety. This automatically disqualifies the ^{252}Cf source, since this source is based on spontaneous fission and obviously cannot be deactivated. Since this system will be placed in the hands of those with little or no radiation safety training, and will also be used within civilian population centers, the inability to turn off the source presents a considerable hazard, and so ^{252}Cf is not a viable source. However, both DD and DT sources may be deactivated, and are still candidate sources.

Source mass is the other significant consideration. This consideration removes DD sources from consideration. Since the fusion rate parameters are significantly smaller for DD than DT at comparable energies, a much larger accelerator must be provided to obtain similar neutron fluxes, which in turn also requires greater cooling. These cooling and accelerator systems push the mass of these systems in excess of what can reasonably be used on a portable system limited to 500 kg total mass. It was also decided by the engineering team at the sponsor that even the 225 kg reflector mass was undesirable for the purpose of a portable system, and so the reflectors have also been removed from the candidate sources.

The best source in terms of performance, safety, and portability is a bare DT source. This source provides the most favourable thermal neutron population distribution, allows the source to be deactivated when not in use, is commonly commercially available, and does not require extensive cooling equipment.

5. Detector selection and placement

Given the selected source, the next step is to determine the type of detector to use in the system. This selection is dictated by both performance and practical considerations. The detector type selected must both produce a strong signal relative to the background, and be practical for a portable system that may be used in remote areas with little technical infrastructure. The system must also be affordable to produce. The detector types considered include high purity germanium, sodium iodide, and BGO detectors.

5.1 Available Detector Types

5.1.1 Scintillation Detectors

The are two types of detectors relevant to gamma ray spectroscopy, the first of which are scintillation detectors. The most common and readily available of these, NaI and BGO, will be considered as larger sizes of these, necessary for the efficient collection of spectra, are readily available without significant lead time. Both of these scintillators are inorganic scintillators, whose scintillation mechanism depends on energy states resulting from the lattice structure of the crystal. The lattice structure results in the valance band, with electrons bound to lattice sites, a band gap in which no electron may exist, and a conduction band which contains electrons which are of sufficient energy that they may freely move through the crystal.

When a particle strikes a scintillator, the energy of the particle is imparted to electrons within the crystal. This can promote them from the valance to the conduction band, and thus create an electron hole pair. As the band gap in materials is generally sufficiently large that energy transitions will not release photons in the

visible spectrum, dopants are added, such as thallium in the case of NaI, to introduce new energy states in the forbidden band so that energy transitions fall within the visible range as well as enhance the rate at which holes are captured by lowering the ionization energy required compared to that of a lattice site. If an electron is recaptured at an activator site, it will do so by transitioning to a lower energy state and releasing a photon. This photon can then be collected by the PMT tube to which the scintillator is coupled, which is then transformed in to an electrical signal which may be measured [41].

Of the two scintillator types, NaI has the superior light yield, giving 40,000 photons per MeV [42], while BGO is 7 – 10% of this value [43], resulting in poorer energy resolution. In addition, its higher index of refraction makes efficient light collection more difficult [41]. It is also more dense, at 7.13 $\frac{g}{cm^3}$ versus 3.67 $\frac{g}{cm^3}$ for NaI, which will allow a greater efficiency as its stopping power will be greater. However, despite its increased stopping power, the primary issue with BGO is its resolution. NaI is capable of 290 keV FWHM while BGO is capable of 350 keV FWHM at 10.8 MeV [44]. Given the proximity of the ^{29}Si background, the higher resolution of the NaI is preferred over that of BGO, regardless of efficiency.

Another potential drawback to NaI detectors is the high capture cross section of ^{127}I, which also produces the radioactive isotope ^{128}I, which has a half life of 25 minutes. This results in a strong 6.8 MeV peak and resultant continuum background below this energy resulting from capture on ^{127}I as well as a constant high background after continuous operation for extended periods of time from the decay products of ^{128}I [45].

5.1.2 Semiconductor Detectors

In contrast to scintillation detectors, semiconductors measure the energy of an incoming gamma ray by measuring charge produced when the gamma ray deposits some of its energy in to a valence band electron in the detector material. Repeated

Quantity	NaI:Tl	BGO
Afterglow ($\frac{\%}{ms}$)	$\frac{0.5-5.0}{3}$	$\frac{0.005}{3}$
Absorption coefficient (cm^{-1})	2.22	9.98
Z_{eff}	51	75
Density ($\frac{g}{cm^3}$)	3.67	7.13
Radiation length (cm)	2.59	1.12
Decay constant (ns)	230	300
Peak emmision (nm)	415	480
Relative light yield	100	7–10
Index of refraction	1.85	2.15
Peak excitation (nm)	290	280
Hygroscopicity	strong	none
Melting point (°C)	651	1050
Radiation Hardness (rad)	10^3	10^4 – 10^5
Hardness (Mohs)	2	5
Cleavage	100	none

Table 5.1.
Properties of BGO and NaI scintillating crystals. [43]

interaction of the gamma ray with the detector produces a cascade of electron-hole pairs which are then collected by an applied electric field.

To provide the best signal, the detector material must have a high absorption coefficient, indicating heavier materials as the absorption coefficient goes as Z^2. The material must further produce many electron-hole pairs for a given quantity of energy (ϵ) to provide good energy resolution, have a high electron-hole mobility to allow collection of charge in a reasonable time, and be available in high purity. Properties of materials suitable for semiconductor detectors are given in Table 5.3.

HPGe

At present, the best properties are those exhibited by germanium, which can be manufactured at high purity, has an energy per electron-hole pair comparable to other suitable materials, a large atomic number and density which allow measurement of higher energy gammas, and further has an electron-hole mobility at least an order of magnitude larger than any other suitable material. However, owing to a relatively small band gap, germanium detectors require cooling to cryogenic temperatures to prevent an excessive leakage current and thus obtain satisfactory energy resolution.

5.2 Performance considerations

Of performance considerations, the most important considerations are energy resolution, detection efficiency, and the maximum number of events the detector can measure within a given time. As a result of the large number of charge carriers produced relative to scintillation detectors (3.38×10^5 electron hole pairs per MeV [46]), HPGe detectors have the best energy resolution, producing peaks with a width of 21 keV FWHM at 10.8 MeV, based on measurements conducted in our lab. Scintillation detectors produce far fewer photons per MeV, with NaI crystals producing 38,000 photons per MeV and BGO producing 8,200 photons per MeV [41] and as result have inferior energy. NaI and BGO detectors are capable of producing peaks with widths of

Material	Atomic Number	Operating Temperature (K)	Band Gap (eV)	ϵ (gcm^{-3})	Density Mobility ($cm^2V^{-1}s^{-1}$)	Electron Mobility ($cm^2V^{-1}s^{-1}$)	Hole Mobility ($cm^2V^{-1}s^{-1}$)
Si	14	293	1.106	3.62	2.33	1350	480
Ge	32	77	0.67	2.96	5.32	3.6×10^4	4.2×10^4
CdTe	48, 52	293	1.47	4.43	6.06	1000	80
CdZnTe	48, 30, 52	283	1.57	4.64	5.78	1000	50 – 80
HgI_2	80, 53	293	2.13	4.22	6.30	100	4
GaAs	31, 33	293	1.45	4.51	5.35	8000	400

Table 5.3.
Properties of semiconductor detector materials. [46]

290 keV FWHM and 350 keV FWHM respectively [44] at the same energy, assuming the energy resolution goes as $\sqrt{E_\gamma}$, hence HPGe provides considerably better energy resolution than either type of scintillation detector.

Both NaI and BGO provide better detection efficiencies at 10.8 MeV. BGO has a detection efficiency of 25% at 10.8 MeV for a 3"x3" right cylinder crystal [47], whereas NaI has a detection efficiency of 4% at the same size, and 8% for a 5"x4" detector [48]. HPGe detectors have a much smaller detection efficiency, with an efficiency of 3.2x10^{-3}% at 10.8 MeV for a 43% relative efficiency detector [49], which has roughly the same size as a 3"x3" right cylinder, making either scintillation detector a better choice.

Scintillation detectors also allow more events to be detected within a given time. While HPGe is limited to 40,000 events per second, NaI and BGO may both accept higher rates. If it is assumed that the light decay time is the principle limitation on event rate, and that a time separation of 4 decay times between events is sufficient to prevent pile up, since under Poisson statistics the probability of two events occurring within the decay time with that rate is 2.4%. Given that BGO has a time constant of 0.3 μs [50] and NaI a time constant of 0.25 μs [51], these detectors may accept 800,000 and 1,000,000 events per second respectively in principle, however the phosphorescence of these scintillators will continually build. The added background of light limits resolution. If 5% resolution is to be maintained, the rate must be limited to 200 kHz.

Given the performance characteristics of the detectors, HPGe is not acceptable, despite its excellent energy resolution, because both the efficiency and the maximum event will reduce the number of counts to a point where these detectors will not provide a reasonable detection time for a practical system. Of the remaining two types of detectors, NaI is the best choice in terms of performance. While BGO may have a better detection efficiency, NaI provides both better energy resolution and a higher maximum event rate, negating any advantage the improved detection efficiency of BGO detectors provides.

5.3 Practical considerations

Practicality considerations also make HPGe undesirable for this application. As previously stated, the system must be practical for a portable system deployed in areas without technical infrastructure. One of the primary concerns with HPGe is cooling, as the detectors must be maintained at liquid nitrogen temperatures for operation, whereas either scintillation detector may be operated at room temperature. Because of the cooling requirement, mechanical coolers must be provided, or a steady supply of liquid nitrogen must be available. Mechanical cooling would considerably increase the cost of the system at $5,000 per cooler. The mechanical coolers would also require additional power generation capability, considering that typical coolers require 400 W of power [52], meaning a 10 detector system would require an additional 4 kW of power generation, which would also decrease the portability of the system, and so mechanical coolers are unacceptable.

If liquid nitrogen were employed to cool the detectors, the cooling nitrogen would present a significant background to nitrogen found in a target of interest, meaning that the liquid nitrogen would either have to be placed far from the detectors, or be heavily shielded. Neither of these requirements is practical in a portable system. A steady supply of liquid nitrogen could also not be guaranteed in likely areas of deployment. Because there is no practical way to cool HPGe detectors with this system, they are not practical for deployment.

Either type of scintillator would be practical for deployment. Neither detector type requires cooling. Both types are radiation hard, and can also be obtained in off the shelf ruggedized packages that would tolerate the mechanical shocks to be expected in a portable system. Both types are also low cost, at roughly $10,000 for a NaI detector package, and $3,000 for a BGO detector package. However, the NaI has the performance advantage given its higher event acceptance rate and energy resolution, and so is the best choice for the system.

5.4 Detector placement

With the detector type selected, the next step is to determine the best arrangement for the detector array. The best detector array is the one that produces the greatest signal significance in the shortest amount of time for a detection target. To determine if a preferable location exists, it was necessary to determine the angular distribution of the gamma rays from both signal and background.

5.5 Angular distribution of gamma rays

In these simulations, a spherical 5 m in diameter was placed centered in the x and y plane on the neutron source and center of an explosive device and centered on the road-air interface in the z plane. The explosive devices were buried at depths ranging from 1 to 60 cm. The spherical surface was further subdivided by conical surfaces in 10 degree increments of the azimuthal angle, starting at $\theta = 10°$ and continuing to $\theta = 80°$, the the 90° mark created by the plane of the concrete surface. And F1 surface current tally was collected on the 10° sections of spherical surface to obtain the angular distribution of 10.8 MeV gammas resulting from the ^{14}N(n,γ) reaction along with the distribution of 10.6 MeV gammas resulting from the ^{29}Si(n,γ) reaction which serves as the primary background to the 10.6 MeV gamma rays. It is expected that the nitrogen gamma rays will be largely biased towards the smaller azimuthal angles, especially as burial depth of the device increases, considering that these gammas will be attenuated as $\exp^{-\mu x}$ through the soil and concrete, as increasing the angle means going through an increasing large amount of soil. As the entire volume of soil contains significant numbers of thermal neutrons, all layers of soil will contribute to the 10.6 MeV background gamma count, and as those coming from the near-surface layers of the soil will be the least attenuated, they should contribute most to the count in the detectors, and so this count may still have a dependence on angle, but not as strong as that of the 10.8 MeV gammas.

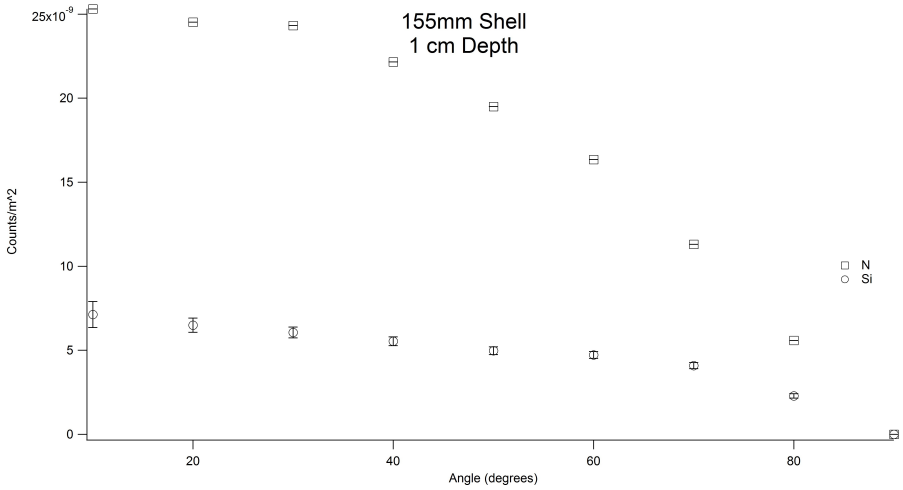

Figure 5.1. Angular distribution of N and Si counts for a 155mm shell at a depth of 1 cm

The explosive devices were chosen to mimic typical munitions. The first representative device is a US-made M-107 high explosive shell, represented by a cylinder of explosive 60 cm in length and 7.747 cm in radius, covered with a 1.27 cm thick layer of A-36 steel and containing 20.5 kg of explosive. The next device chosen was designed to represent a US-made Mk-12 bomb, and is represented in the simulations as a cylinder of explosive 78.74 cm in length and 17.78 cm in radius joined to a hemisphere 17.78 cm in radius, covered with a 1.27 cm thick layer of A-36 steel, containing 164 kg of explosive. The final object selected was representative of an Italian made VS-2.2 mine, and represented by a cylinder of explosive 5 cm high and 12 cm in radius, covered by an 0.635 cm layer of polyethylene.

As can be seen from the Figs. 5.1 – 5.21, no preferable location exists where signal outpaces the silicon background, however in the far surface cases, those in which the explosive producing signal is the farthest from the neutron source, the signal generally begins to drop off at the 40° mark. As a result, the detector array will designed to fall within this cone.

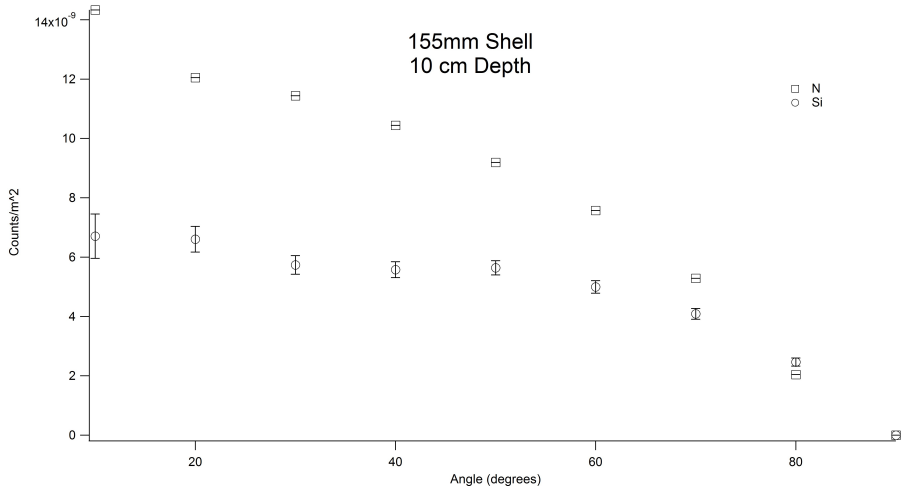

Figure 5.2. Angular distribution of N and Si counts for a 155mm shell at a depth of 10 cm

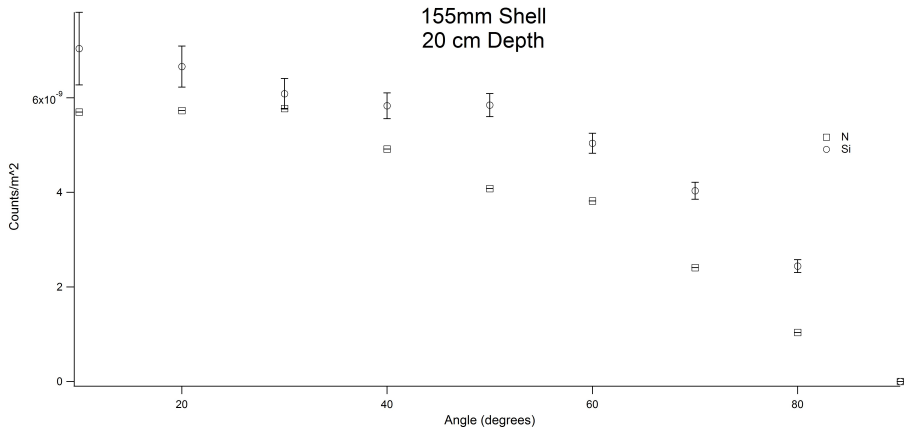

Figure 5.3. Angular distribution of N and Si counts for a 155mm shell at a depth of 20 cm

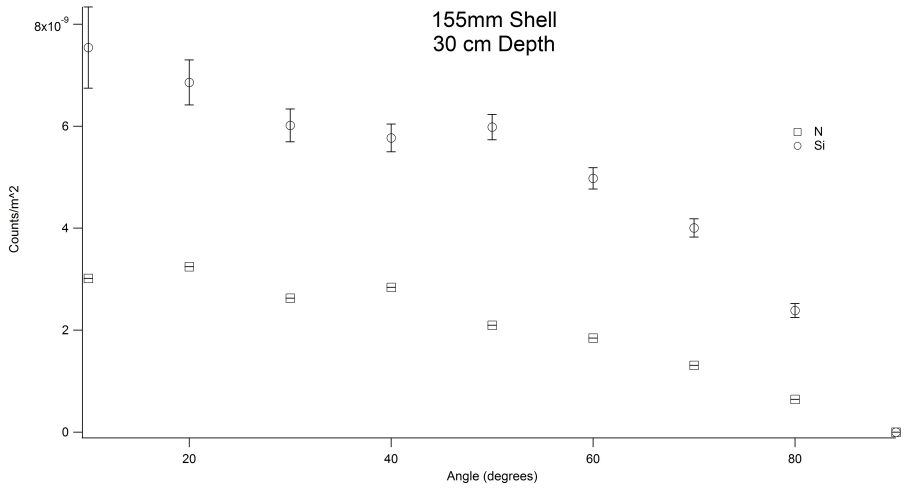

Figure 5.4. Angular distribution of N and Si counts for a 155mm shell at a depth of 30 cm

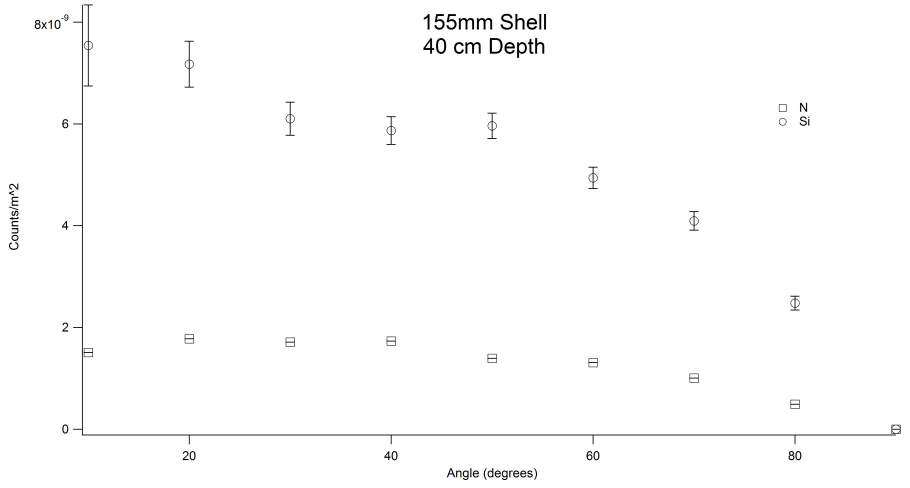

Figure 5.5. Angular distribution of N and Si counts for a 155mm shell at a depth of 40 cm

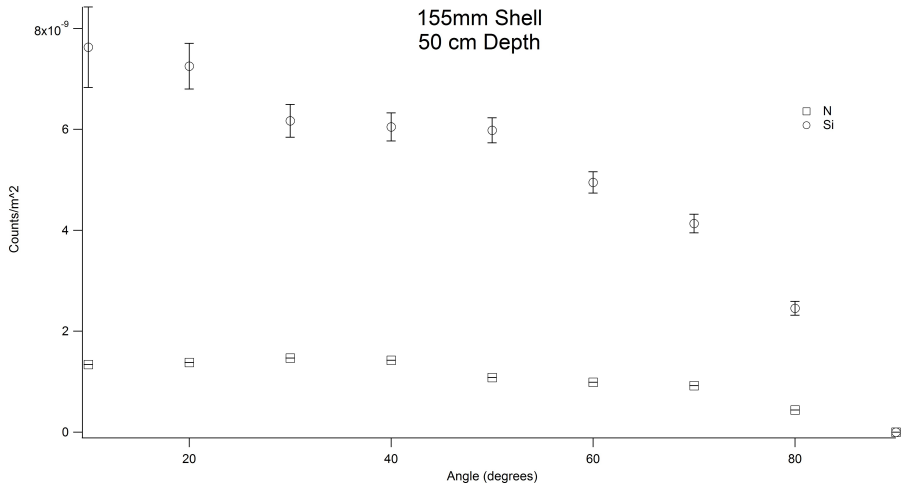

Figure 5.6. Angular distribution of N and Si counts for a 155mm shell at a depth of 50 cm

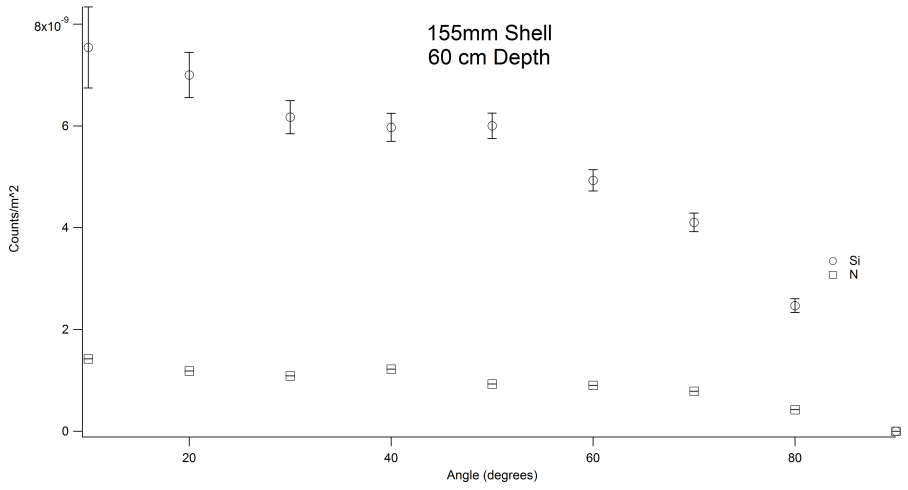

Figure 5.7. Angular distribution of N and Si counts for a 155mm shell at a depth of 60 cm

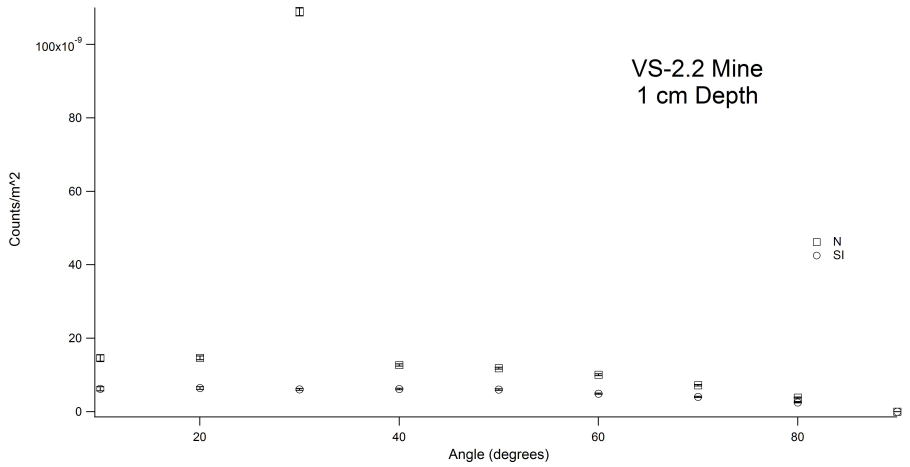

Figure 5.8. Angular distribution of N and Si counts for a VS-2.2 mine at a depth of 1 cm

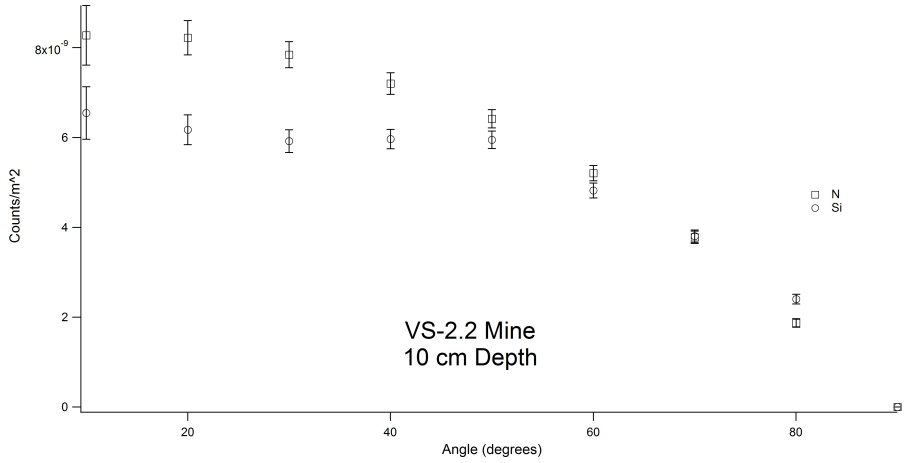

Figure 5.9. Angular distribution of N and Si counts for a VS-2.2 mine at a depth of 10 cm

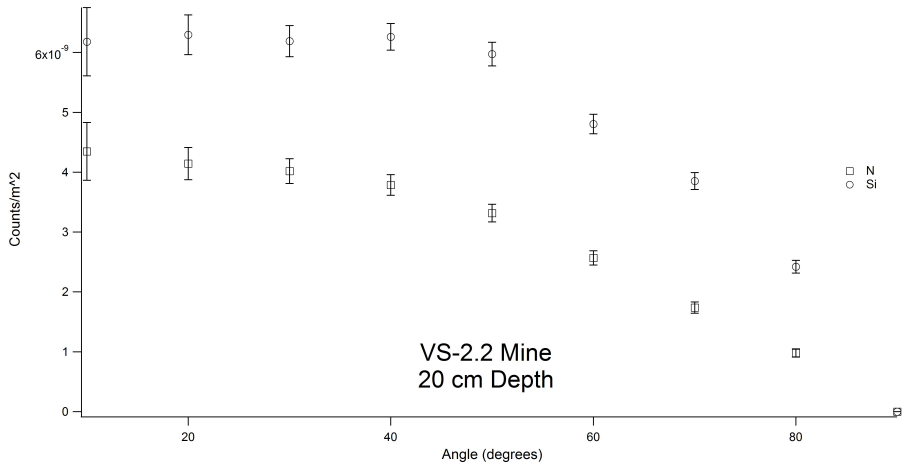

Figure 5.10. Angular distribution of N and Si counts for a VS-2.2 mine at a depth of 20 cm

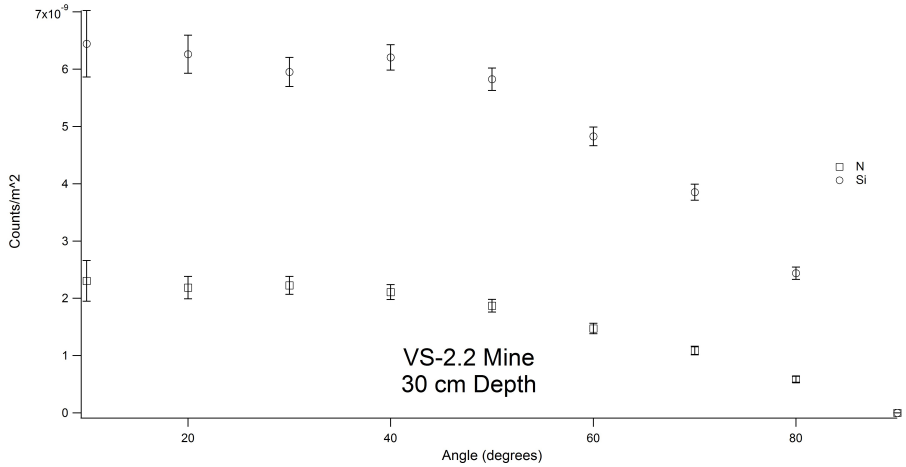

Figure 5.11. Angular distribution of N and Si counts for a VS-2.2 mine at a depth of 30 cm

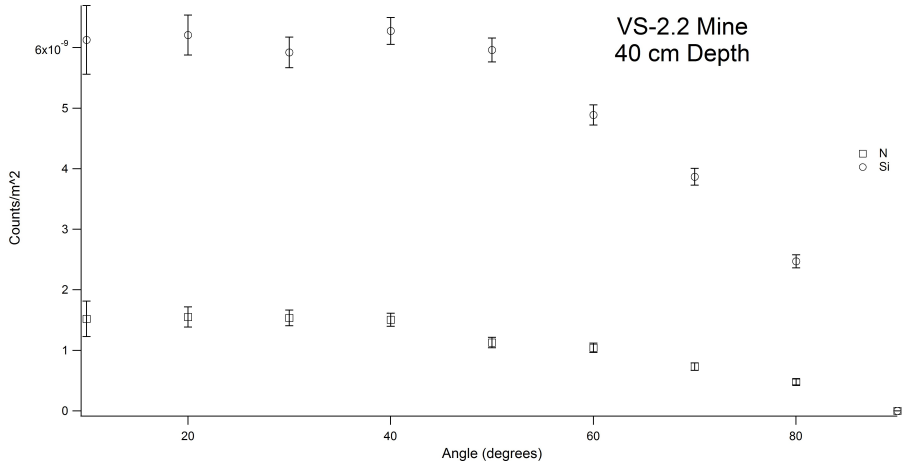

Figure 5.12. Angular distribution of N and Si counts for a VS-2.2 mine at a depth of 40 cm

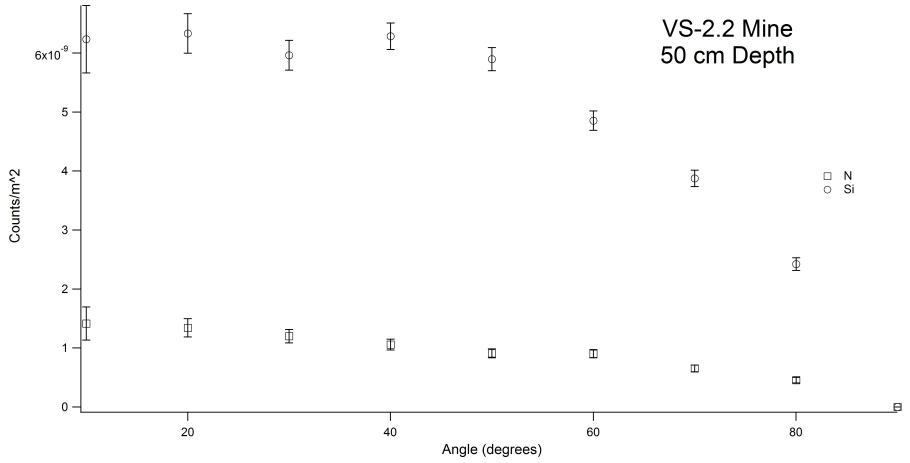

Figure 5.13. Angular distribution of N and Si counts for a VS-2.2 mine at a depth of 50 cm

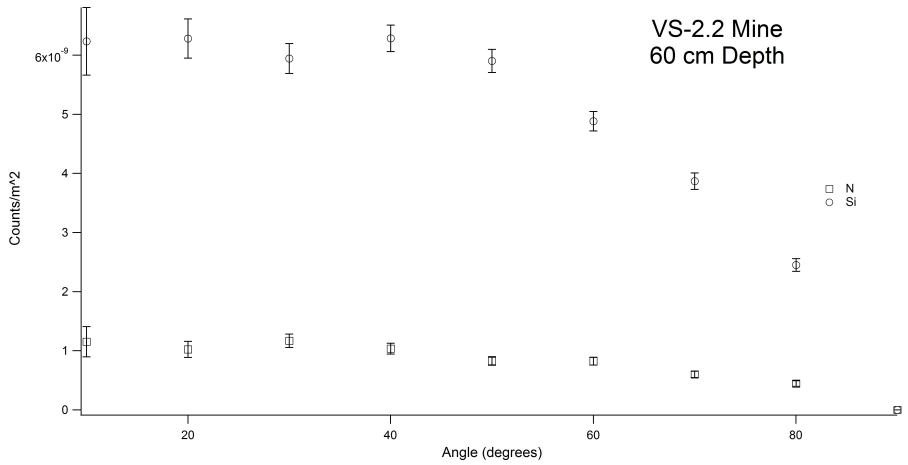

Figure 5.14. Angular distribution of N and Si counts for a VS-2.2 mine at a depth of 60 cm

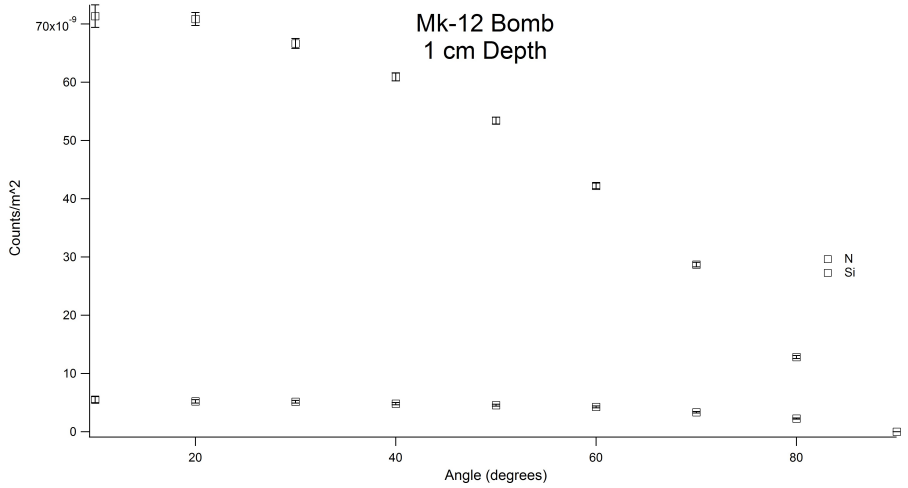

Figure 5.15. Angular distribution of N and Si counts for a Mk-12 bomb at a depth of 1 cm

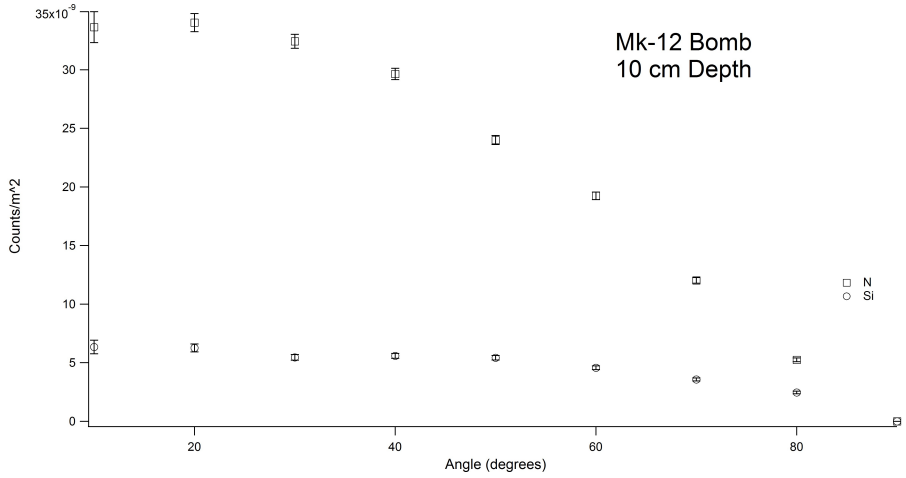

Figure 5.16. Angular distribution of N and Si counts for a Mk-12 bomb at a depth of 10 cm

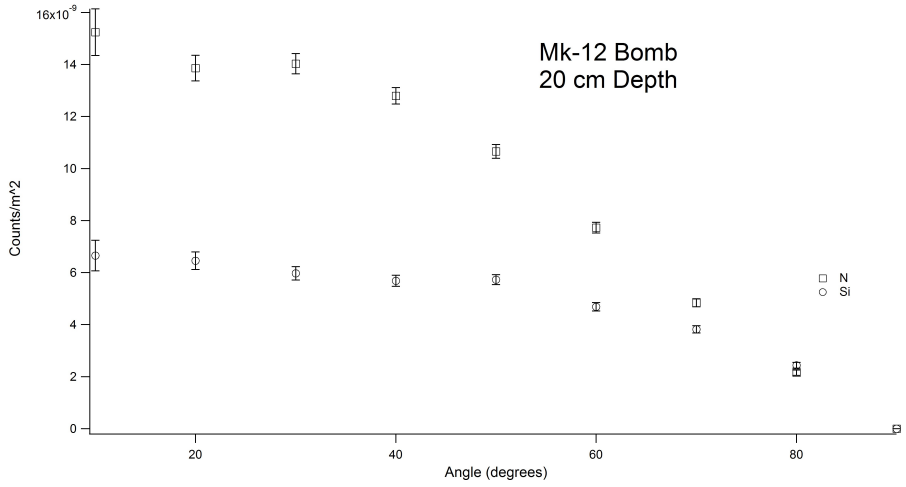

Figure 5.17. Angular distribution of N and Si counts for a Mk-12 bomb at a depth of 20 cm

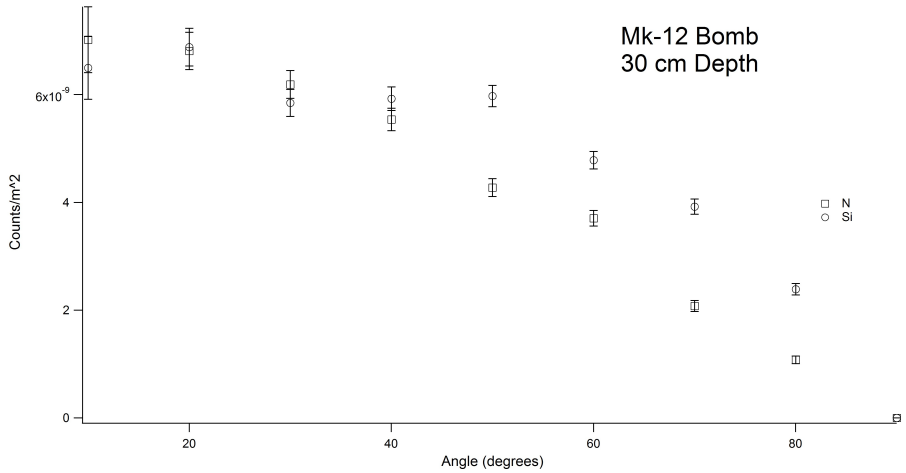

Figure 5.18. Angular distribution of N and Si counts for a Mk-12 bomb at a depth of 30 cm

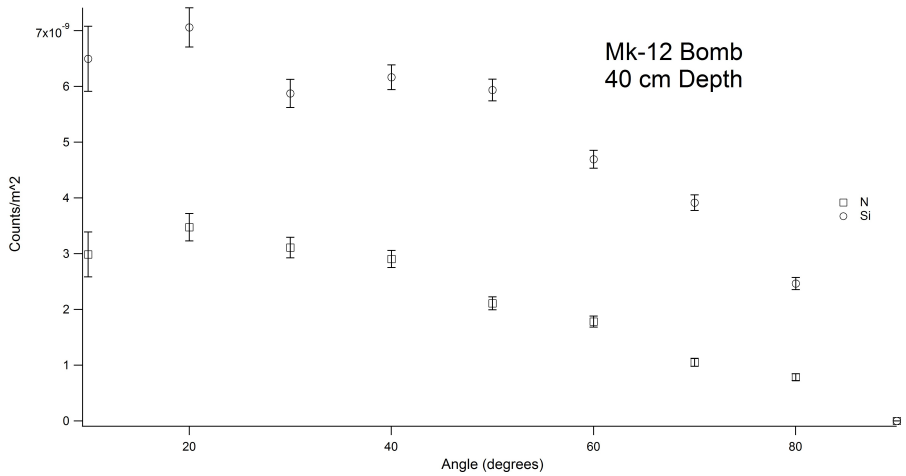

Figure 5.19. Angular distribution of N and Si counts for a Mk-12 bomb at a depth of 40 cm

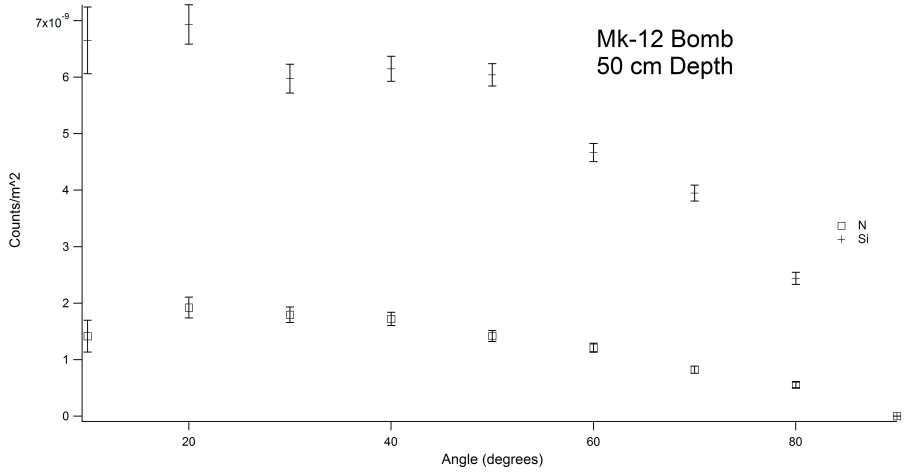

Figure 5.20. Angular distribution of N and Si counts for a Mk-12 bomb at a depth of 50 cm

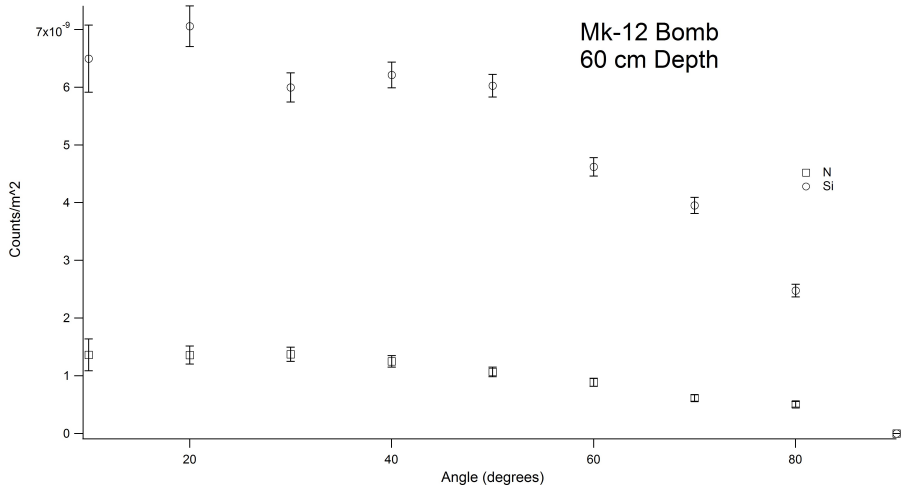

Figure 5.21. Angular distribution of N and Si counts for a Mk-12 bomb at a depth of 60 cm

Efficiency Effects

In addition to the radius of the detector array, another factor that must be decided is the angle of the detector with respect to the ground. To be useful for spectroscopy purposes, a gamma ray's energy must be fully absorbed by the detector material. In the case of an infinitely large detector, all energy is absorbed because the initial photon and all subsequent photons of lesser energy have a track length sufficient for the photon to interact with the material and impart its energy to the detector material.

With a real detector of finite size, however, there is no guarantee that a photon will be absorbed. Classic examples of this include first and second escape lines, which are created by photons which interact with the detector material through pair production, but one or both of the 511 keV annihilation gamma rays escapes the detector, leaving peaks 511 keV and 1022 keV from the true peak.

If the signal is to be maximized, then the path length the signal gamma rays travel through must be maximized. To understand the dependence of the full photopeak efficiency on the location and angle at which the gamma ray strikes the detector surface, an MCNP study was conducted.

In this study, a photon source was created which put out a monoenergetic beam of photons directed at a 10.16 cm $\times$ 10.16 cm right cylindrical NaI detector. A 0.5 mm thick layer of aluminum covered the cylinder, which is typical of NaI detectors produced by Canberra, a scintillation detector manufacturer.

The photon source and NaI detector were then enclosed in a 1 m sphere in which there was only a vacuum. The photon source was then directed at the detector at 0, 2.54, 5.08, and 7.62 cm from the detector's center. For each location, the angle at which the photon struck the detector surface was varied from -80° to +80° with respect to the normal from the detector surface. An energy deposition (F8) tally was then used to determine the energy deposition in the NaI, yielding the energy spectrum that would be produced by a NaI detector. Gaussian energy broadening was also

applied to the F8 tally to reflect the energy resolution typical of NaI detectors. The resolution of detectors is given by

$$\text{FWHM} = a + b\sqrt{E + cE^2} \tag{5.1}$$

Broadening constants of $a = -0.00789$ MeV $b = 0.06769$ MeV$^{\frac{1}{2}}$ $c = 0.21159$ MeV^{-1} were used [53] to simulate actual detector behavior.

Results from this simulation are given in Figs. 5.22 – 5.25. Among the more interesting results of this simulation are that the primary photopeak at 10.8 MeV seems undesirable to indicate the presence of bulk explosive. This becomes particularly obvious when looking at the region of interest as shown in Fig. 5.25. This shows the energy spectrum in the vicinity of the 10.8 MeV peak produced by ^{14}N with a 10.8 MeV photon source directed at the center of the detector with an angle of incidence of -80°. As can be seen, the 10.8 MeV peak is barely noticeable, and in practice automated peak search routines have difficulty locating this peak without finding numerous superfluous peaks. By contrast, the first escape peak at 10.289 MeV is prominent and easily found by automated peak search routines. Moreover, better efficiency is generally obtained at the 10.289 MeV line. While the maximum efficiency seen at the 10.8 MeV line of $0.144368 \pm 2.88736 \times 10^{-5}$ is higher than the that of the 1st escape peak at $0.106533 \pm 3.19599\text{e} \times 10^{-5}$, the efficiency across the range of angles of incidence is higher for the 1st escape peak. In particular, at the extremes of angles of incidence, the primary photopeak has its lowest efficiency of $0.0154756 \pm 1.23805 \times 10^{-5}$, while the 1st escape peak's lowest efficiency is $0.0620816 \pm 2.48326 \times 10^{-5}$.

This effect is likely the result of the small size of the detector. When an electron-positron pair are formed, by momentum conservation, the two particles are emitted anti-parallel to each other. Given a random orientation within the detector, one particle is likely to experience a long track length in the detector material while the other experiences a relatively short track, meaning that it is likely that only one instead of both particles will expend its full energy in the detector, and in doing so create a first escape peak that is more prominent than the primary photopeak at 10.8

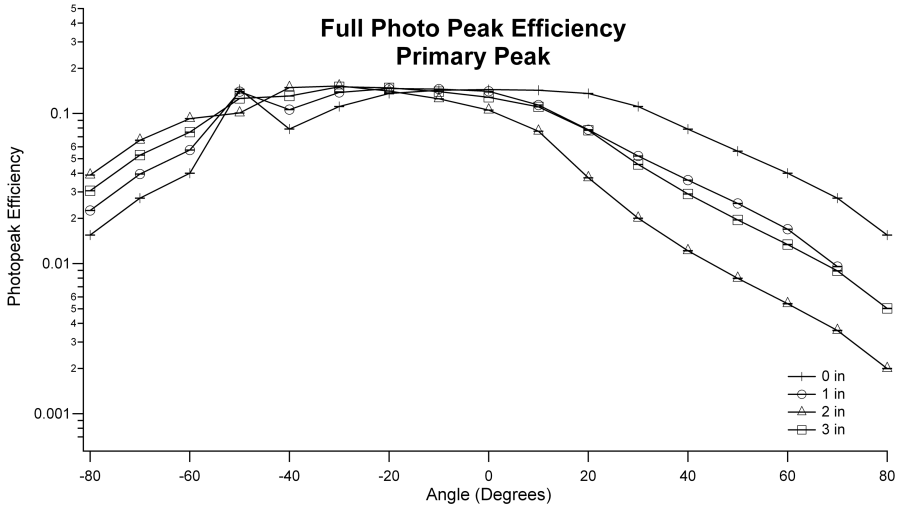

Figure 5.22. Primary full photopeak efficiency for the 10.8 MeV line

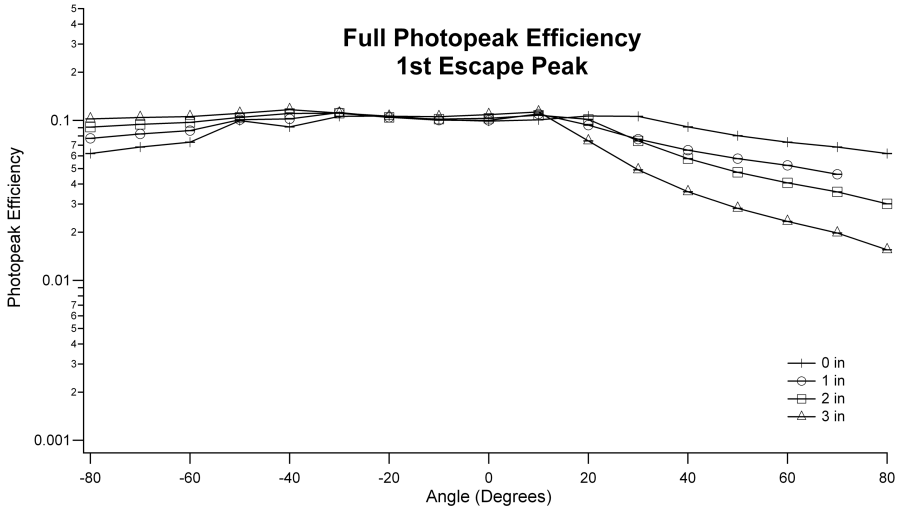

Figure 5.23. Full photopeak efficiency for the 1st escape peak of the 10.8 MeV line

MeV. The 1st escape peak is thus a better choice for detection as it should generally be more prominent than the primary photopeak.

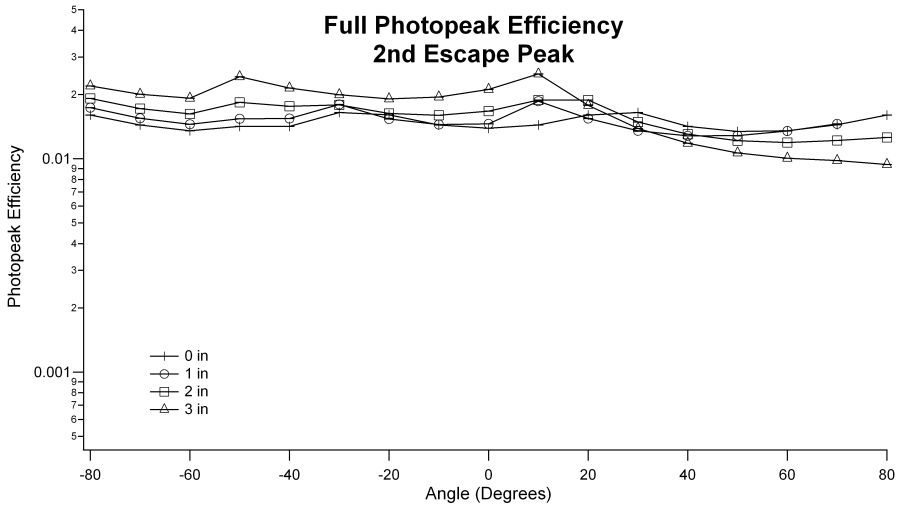

Figure 5.24. Full photopeak efficiency for the 2nd escape peak of the 10.8 MeV line

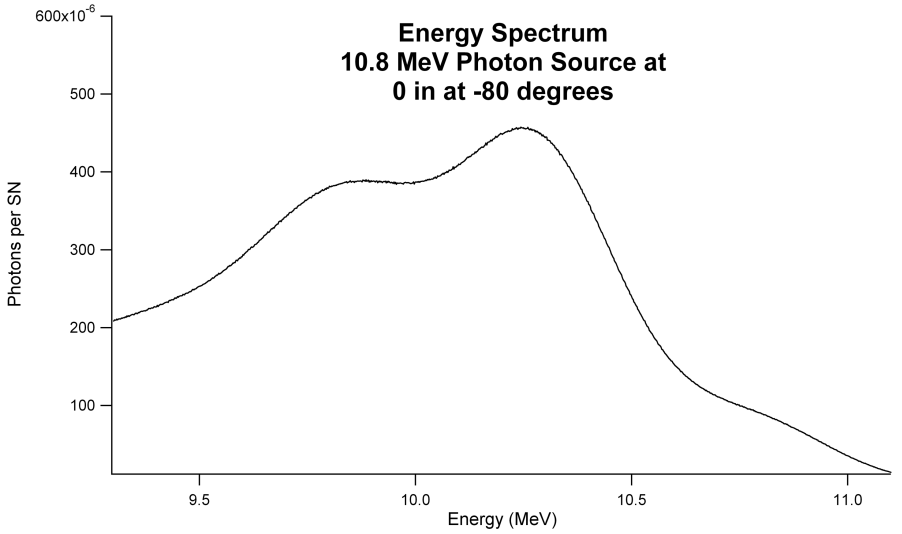

Figure 5.25. Energy spectrum produced by a 4"×4" NaI detector in the 10.8 MeV region with a photon source striking the center of the detector at -80° incidence

5.6 Timing Gate

Central to a TNA system is the selection of a timing gate for the detector. In the 11 MeV region of the gamma ray spectrum, there are few lines from thermal capture. As a result, the bulk of the background in this region will result from the presence of inelastic scatter reactions and their corresponding backgrounds. Inelastic scatter reactions occur soon after release of the neutron pulse, as these reactions typically have threshold energies above 6 MeV, and so after a period of time neutrons of sufficient energy to participate in an inelastic scatter reaction will either scatter away from the point of interrogation, or thermalize and lack sufficient energy to produce an inelastic scatter reaction. To determine this, a simulation was conducted in which a 6 m by 6 m by 6 m cube of soil was placed below a 6 m by 6 m by 10.16 cm concrete surface. A cube of air 6 m by 6 m by 6 m was then placed above the concrete. A 155 mm shell containing explosive was placed at a depth of 30 cm to produce signal. An F1 tally of photons was then collected at the concrete-air interface. This F1 tally was further binned by time in 10 μs bins and by 10 keV increments of energy to allow measurement of the spectrum of photons leaving the soil as a function of time from neutron release.

The results of this simulation can be seen in Fig. 5.26. As can be seen from the graph, the total count across all energies decreases rapidly with time. By 20 μs, the total count across the spectrum has been reduced by three orders of magnitude, while the signal count has only been reduced by roughly a factor of two. As a result, the introduction of a timing gate will allow for a substantial reduction in the dead time of the detectors and the background of the 10.8 MeV line. The effect of gating can be seen in Fig. 5.27. Without the gate, no peaks are apparent in the signal region. With the gate included, however, background in the signal region reduces dramatically, making the 10.8 MeV nitrogen line and its 10.6 MeV background from silicon plainly visible.

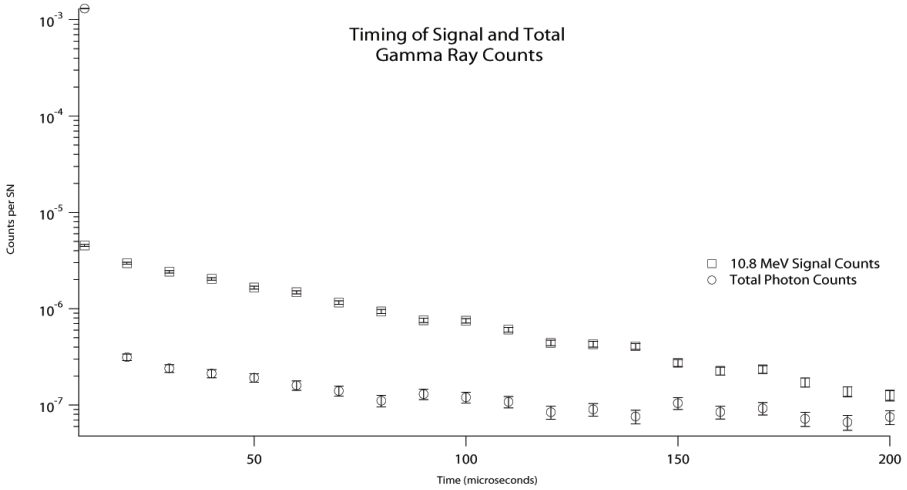

Figure 5.26. Total and signal background counts emerging from the ground as a function of time.

To determine the proper beginning and ending time for the gate, a simulation was run using the same deck with the count collection starting at 10 μs, and a variable end of the collection time, starting at 20 μs through 200 μs in 10 μs increments. This was repeated for a start of collection at 15 and 20 μs. As can be seen from Fig. 5.28, there is little difference in the number of counts accumulated between these initial points, nor is there a significant reduction in the background in the signal region. To allow faster repetition of the collection cycle, and because there is little disadvantage in doing so, collection with the detectors should begin 10 μs after the neutron pulse is turned off.

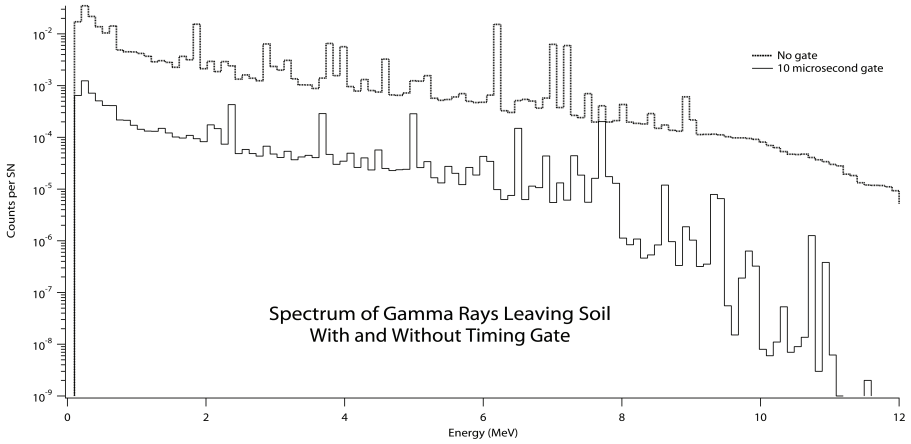

Figure 5.27. The effect of a 10 μs gate on the spectrum of gamma rays leaving the soil.

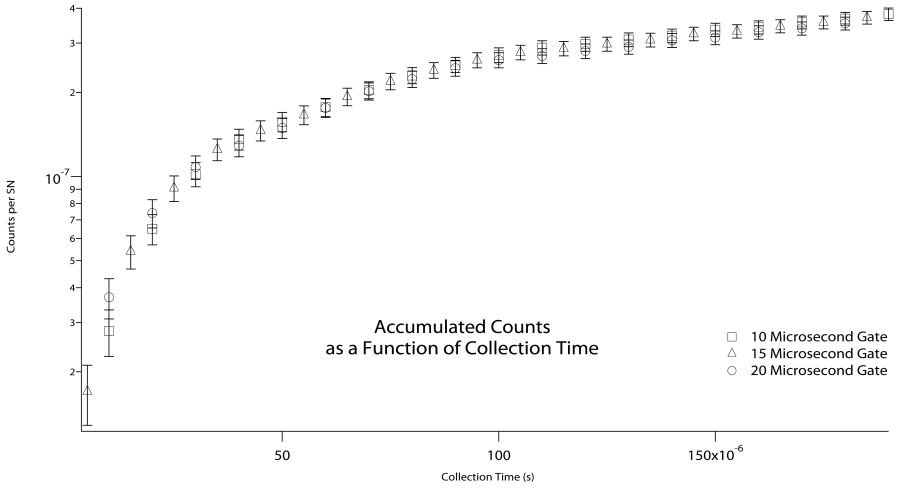

Figure 5.28. Accumulated signal gamma rays crossing the soil-concrete interface as a function of starting and ending collection times.

6. Shielding

In order for the detection system to be most effective, the detectors must be shielded from excess neutrons and gamma rays. The goal of this is to reduce activation of the the crystal, prevent detector damage, and limit degradation of detector performance caused by afterglow created by excess gamma rays, which in turn will all degrade detection time of the explosive.

It is important to shield the detectors from neutrons, both because of radiative capture reactions on the crystal material, and because fast neutrons can damage the crystalline structure of the scintillation material, resulting in degradation of performance. Slow neutrons further degrade performance by participating in thermal capture reactions on ^{127}I and ^{23}Na, with cross sections of 10 b and 0.53 b, respectively [31]. These capture reactions not only release prompt gamma rays, but further result in the radioactive isotopes ^{128}I and ^{24}Na, with half lives of 25 minutes and 15 hours, resulting in background spectra and increasing the gamma ray fluence which will in turn increase afterglow [54].

It is then necessary to shield the detectors from neutrons of all energies using a shield, but that shield itself may contribute prompt gamma rays or additional neutrons, as is the case in materials such as lead, a material often used to shield gamma rays, which participates in inelastic scatter reactions which produce gamma rays, but also in reactions such as the (n, 2n) reaction which multiplies the number of free neutrons.

Shielding may be provided by either absorption or reflection. In absorption, the incident neutron is consumed in a reaction, whereas in reflection it is scattered away from the shielded area. That reflection may either change the energy of the incident neutron, so that moderation occurs, or may leave the energy of the neutron largely

unchanged, which is referred to as reflection. The energy lost during an elastic scatter is a strong function of the mass number of the target nucleus, A, and is given by

$$\Delta E = \frac{1}{2}\left[1 - \left(\frac{A-1}{A+1}\right)^2\right] E_i \tag{6.1}$$

In hydrogen, for which $A = 1$, this becomes $\frac{1}{2}E$, while for high A materials,

$$\Delta E = \lim_{A\to\infty} \frac{1}{2}\left[1 - \left(\frac{A-1}{A+1}\right)^2\right] E_i = 0$$

and so light nuclei are preferred for moderation, while heavy nuclei are preferred for reflection.

6.1 Moderation

Moderators are often used in combination with an absorber to reduce neutron population, since the neutron absorption cross section is usually strongly dependant on energy, with greater cross sections occurring at lower energies. Many neutron absorbers have absorption cross sections which go as the inverse of the incident neutron speed, and so decreasing neutron speed via moderation may make a neutron shield based on neutron absorption more effective.

Hydrogen is generally the preferred moderator nucleus as it reduces incident neutron energy by half on average. Common hydrogen containing materials used for moderation are paraffin wax and both heavy and light water. While both ^{1}H and ^{2}H cannot participate in inelastic scattering reactions which often yield gamma rays, both may capture a thermal neutron, producing a gamma ray in the process. Hydrogen produces a 2.2 MeV line and has a thermal capture cross section of 334 mb, while deuterium has an 0.5 mb cross section and produces a 6.3 MeV gamma [31,32]. While hydrogen-bearing materials may be favorable for moderation, the MeV energy gamma rays produced by thermal capture reactions produced may require considerable shielding material on their own.

Other common moderating materials are carbon, often in the form of graphite, beryllium in its metallic form, and ^{7}Li, usually as a salt. Beryllium is both expensive

to aquire and toxic. It also has a 8.6 mb thermal capture cross section, with the most probable gamma ray produced having an energy of 6.8 MeV. ^{7}Li also has a 46 mb thermal capture cross section, and produces its strongest line at 2.0 MeV [31,32]. Unlike beryllium or lithium, carbon has no significant thermal capture lines, and so will produce less background than either maeterial. It is also inexpensive and readily available, making it a common choice for a moderator, despite its larger A which will in turn result in a greater thickness required to provide moderation.

The required thickness for a moderator to reduce a neutron's energy between two values may be calculated. A convenient measurement of energy loss is given by the logarithmic energy decrement, given by

$$\xi = \ln\left(\frac{E_i}{E_f}\right) \tag{6.2}$$

The number of collisions, N, required to reduce the energy of a neutron to a given energy, E_l, from an energy, E_h, is given by

$$N = \frac{\ln\left(\frac{E_h}{E_l}\right)}{\xi} \tag{6.3}$$

The RMS distance travelled in a three dimensional random walk, d_r, is related to the path step size, d_s, and the number of steps taken, N, by

$$d_r = d_s\sqrt{\frac{N}{3}} \tag{6.4}$$

The appropriate step size for moderation is the mean free path between elastic scatterings. For any material, this mean free path, λ, is given by

$$\lambda = \frac{1}{\sum_i n_i\sigma_i} \tag{6.5}$$

where σ_i is the elastic scattering cross section of the ith isotope and n_i is its number density.

6.2 Absorbtion

There are a number of nuclei with large absorption cross sections that either do not produce gamma rays or produce low energy gamma rays that are readily shielded.

These include ^{6}Li, ^{10}B, and ^{113}Cd. ^{3}He and Gd are also effective neutron absorbers, but are extremely expensive. Cadmium is also an effective neutron absorber, but is highly toxic and emits gamma rays at 558, 576, 725, 806, 1210, 1364 and 1399 keV during its capture process, making it less preferable than lithium and boron. Of these materials, lithium and boron are preferred as both have significant absorption cross sections, and in addition generate no gamma radiation in the case of lithium, and only a 482 keV gamma ray in the case of boron.

6.3 Bulk material testing

6.3.1 Candidate Materials

Two elements were identified as a basis for an absorption-based neutron shield, lithium and boron. Lithium presents the significant advantage in that its most significant neutron absorption reaction, the ^{6}Li(n, α)^{3}H reaction, produces no gamma radiation and has a cross section of 941 b [31]. However, it also produces tritium, which presents a safety hazard as a result of its radioactive decay. It also present a proliferation concern, and further the trapped gas can cause bulging of the structure of the shielding material. Boron, by contrast, has a 3838 b neutron absorption cross section, mostly as a result of the ^{10}B(n,$\alpha\gamma$)^{7}Li reaction. While this reaction does create a gamma ray, its energy is only 482 keV, and so is readily shielded by a thin lead shield.

Lithiated and borated polyethylene both present the advantage of a high hydrogen content, which, as a result of the its low atomic wieght is an extremely effective moderator, per Eq. 6.1. Since the neutron absorption cross sections of both boron and lithium follow the a $\frac{1}{v}$ dependence, lower energy neutrons will capture with higher probability than higher energy neutrons, and so it is ostensibly preferable to reduce the incident 14 MeV neutrons in the shielding material via moderation. The presence of hydrogen also presents a problem as a result of the 334 mb thermal capture cross section, which produces a 2.2 MeV gamma ray that will require substantial shielding

to prevent a considerable background to the detectors, especially given their proximity. Another significant disadvantage the low density of polyethylene, at 0.9 g/cc, which limits the macroscopic cross section for both scattering and neutron absorption, which will limit the efficacy of polyethylene shields with a practical size.

Boron carbide has the advantage that it does not create any appreciable thermal capture gamma rays, beyond a 478 keV gamma produced by boron with 94% probability. It also has a high density relative to the polyethylene-based materials at 2.52 g/cc, which will results in a larger macroscopic cross section for the absorption reaction. Carbon also has no significant thermal capture lines, though does have a strong 4.4 MeV fast neutron line. While any fast lines will not be recorded in the spectrum as a result of detector gating, these gammas will still present a concern as a result of the afterglow effect of scintillation spectrometry, and so can still present a concern as it relates to the resolution of the detectors. Carbon will also moderate the incoming 14 MeV neutrons, though to a lesser degree than hydrogenous materials.

Lithium fluoride is another possibility, and is easily slip cast in to a number of possible forms. It also holds a density advantage over the polyethylene-based materials at a density of 2.64 g/cc. Lithium fluoride retains the advantage that neutron absorption will be non-radiative. Fluorine does produce two strong high energy capture lines at 6.6 MeV and 1.6 MeV, but has a capture cross section of only 10 mb, and so background resulting from the shield should be minimal. It will still present the issue of tritium production as a result of the neutron absorption reaction.

Lead will not provide moderation or significant neutron absorption. Instead, it can act as a shield by reflecting incident neutrons, as opposed to the above discussed materials which will function as shields via neutron absorption. Since lead has a large atomic mass, when high energy neutrons collide with lead atoms, they will be scattered with nearly the same energy as their incident energy. Thus, by elastic scattering, a large number of incident neutrons will be reflected rather than transmitted or absorbed by the shield. Lead might, however, present an issue as a result of its (n, 2n) cross section. The neutron products of this reaction will have low energy, and so

could present an issue. Moreover, lead produces three strong fast lines at 7.37, 6.74, and 6.80 MeV. While a lead shield would self shield these capture gamma rays to a degree, it would also block any signal gamma rays, and so could result in a decline of system performance.

6.3.2 Shielding performance

To select the best shielding material, an initial run was made in MCNP. A 5 m by 5 m plane of the test material was used in the simulation. On either side of the material, a cell containing vacuum was placed. A 14 MeV point source of neutrons was then placed centered on the square, and 0.5 cm above the material's surface. An F1 tally of the neutrons passing the surface of the material opposite the source was then collected. Plots were then made of the neutrons with $E \geq 6$ MeV, the threshold of most fast neutron reactions, and the thermal neutrons (defined as having $E \leq 0.173$ eV, the energy at which the exponential term in the Boltzmann distribution at room temperature is equal to 0.001). Candidate materials selected include boron carbide, a ceramic material, borated polyethylene, polyethylene lithiated with both natural lithium and 90% enriched lithium, lithium fluoride, and lead. The results of these simulations can be seen in Figs. 6.1 – 6.12.

As thicker shields will limit portability of the system, the required thickness to reduce the fast neutron population by two orders of magnitude will be used to evaluate materials, along with the thermal neutron population at that thickness. Results are given in Table 6.1. As can be seen from the table, the best performers are boron carbide and lithium fluoride, with both reducing the fast neutron population to the requisite level at 15 cm, with boron carbide producing a 10% lower population given the same thickness, likely as a result of boron's larger neutron absorption cross section. Boron carbide does, however, have a 4% higher thermal neutron population at this thickness. The mass required of moderator material is roughly comparable, with boron carbide having a slightly smaller mass. Borated, enriched lithiated, and

non-enriched lithiated polyethylene all required 25 cm of material to reduce the fast neutron population by two orders of magnitude, with borated polyethylene performing the best, followed by enriched lithiated polyethylene, and non-enriched lithiated polyethylene. All of these require the same mass of material. The worst performer is lead. Although comparable in terms of reduction of the neutron population, the mass required to reach this reduction was an order of magnitude above the other candidate materials, and well above that which would feasibly fit in a portable system.

From the initial results, either boron carbide or lithium fluoride would be the best choices for shielding material. Lead is simply too heavy to be of use and has performance comparable to materials that are far lighter. The mass required for any of the polyethylene materials is comparable to that required of lithium fluoride or boron carbide, but the bulk significantly greater. Moreover, the polyethylene materials will require, in addition to the bulk material, an additional cladding of lead of significant thickness to cover the shielding material to shield the 2.2 MeV gamma rays produced by thermal capture on hydrogen within the materials.

Of the two remaining materials, boron carbide the best options, given that the only backgrounds it will produce are the relatively easily shielding 478 keV rays from boron, as compared to that of fluorine at 7.37, 6.74, and 6.80 MeV. In addition, boron carbide is an extremely tough ceramic, and is often used create armor for tanks as a result of its toughness. In the event of detonation of an undetected IED, the neutron shield might limit damage to system components. By contrast, lithium fluoride is a brittle glass, and so might present issues both in a rugged environment, and would not provide similar protection.

6.3.3 Shielding Design Considerations

With the material for the shield determined, the shielding must be designed to fit the application. In this case, there are three things that the detectors must be protected against, 14.1 MeV neutrons from the generator, neutrons which are backscat-

Material	Thickness (cm)	Fast Neutron Population (per SN)	Thermal Neutron Population (per SN)	Mass (kg)
B_4C	15	$9.22622\times10^{-3}\pm$ 0.0005	3.91669E-03 $\times10^{-3}$ 0.0005	192
B Polytheylene	25	$9.48142\times10^{-3}\pm$ 0.0005	$4.65144\times10^{-3}\pm$ 0.0006	160
E Li Polytheylene	25	$1.01590\times10^{-2}\pm$ 0.0004	$4.81487\times10^{-3}\pm$ 0.0006	160
NE Li Polytheylene	25	$1.05543\times10^{-2}\pm$ 0.0004	$6.92372\times10^{-3}\pm$ 0.0005	160
LiF	15	$1.02571\times10^{-2}\pm$ 0.0004	$3.77529\times10^{-2}\pm$ 0.0002	202
Pb	25	$1.05812\times10^{-2}\pm$ 0.0004	$1.40589\times10^{-2}\pm$ 0.0004	1970

Table 6.1.

Initial shielding results

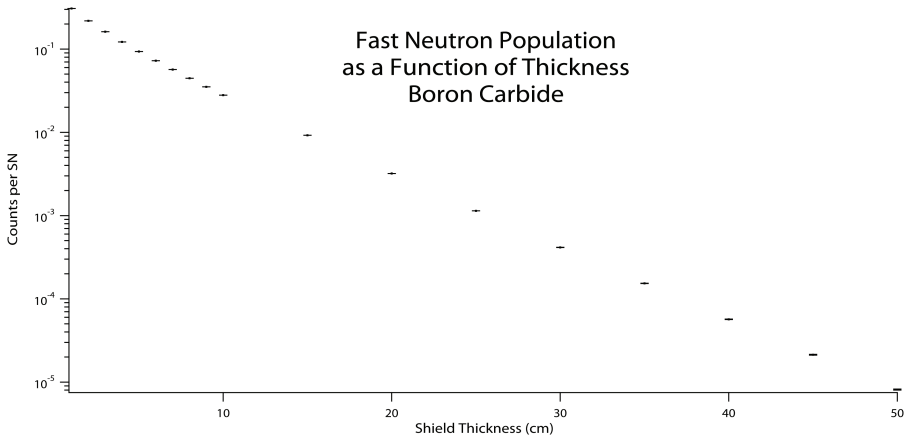

Figure 6.1. Thermal neutron population as function of thickness for a boron carbide shield.

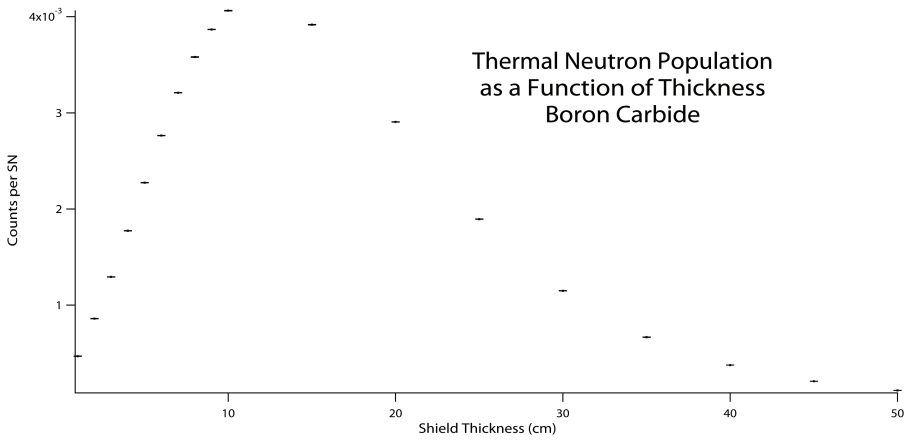

Figure 6.2. Thermal neutron population as function of thickness for a boron carbide shield.

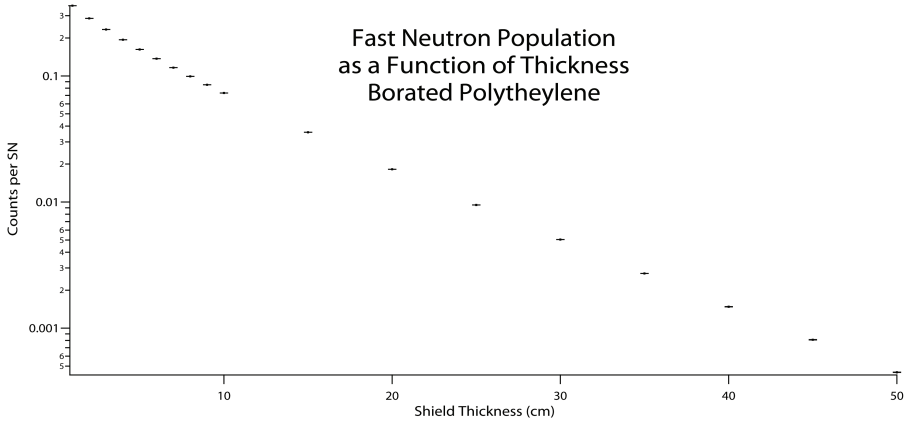

Figure 6.3. Fast neutron population as function of thickness for a borated polytheylene shield.

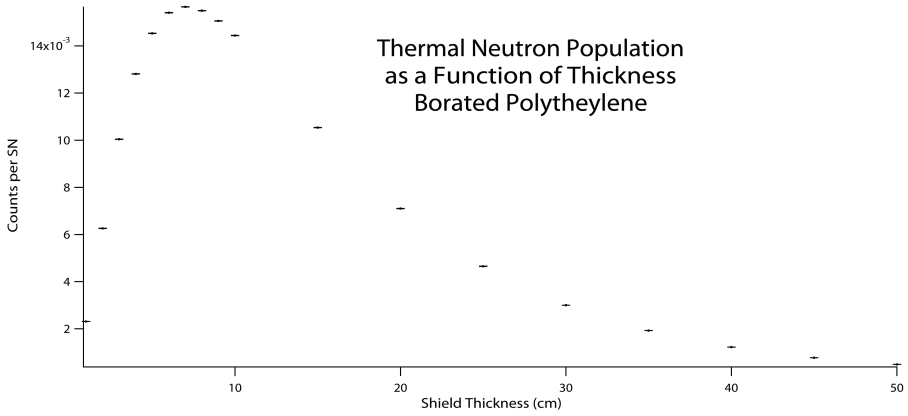

Figure 6.4. Thermal neutron population as function of thickness for a borated polytheylene shield.

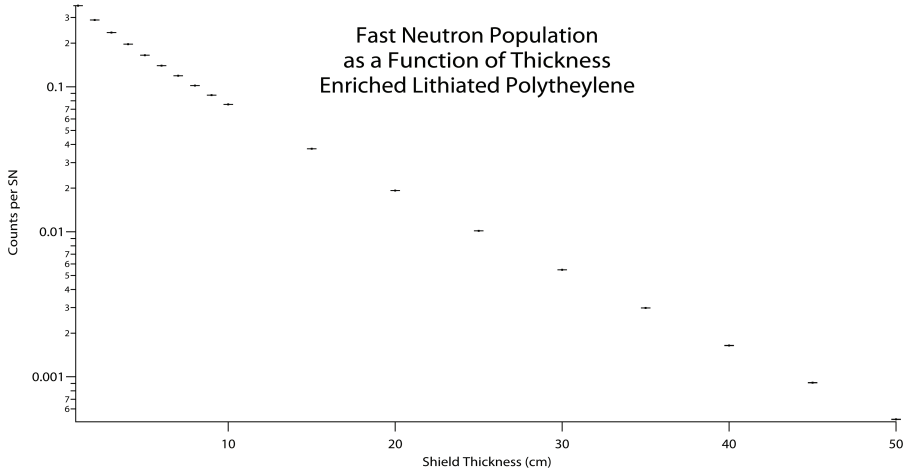

Figure 6.5. Fast neutron population as function of thickness for an enriched lithiated polytheylene shield.

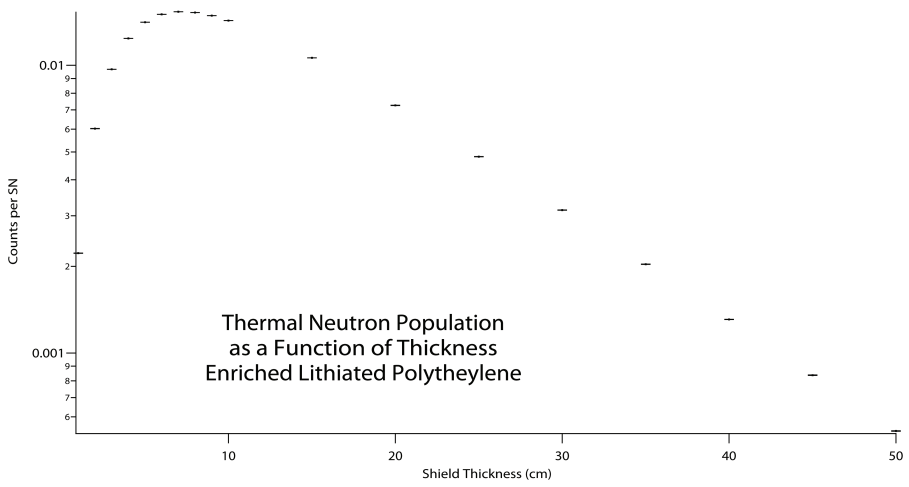

Figure 6.6. Thermal neutron population as function of thickness for an enriched lithiated polytheylene shield.

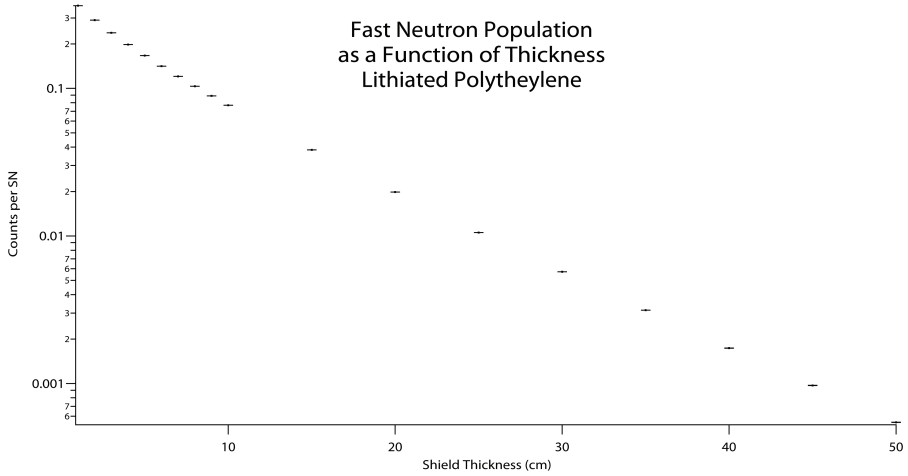

Figure 6.7. Fast neutron population as function of thickness for a unenriched lithiated polytheylene shield.

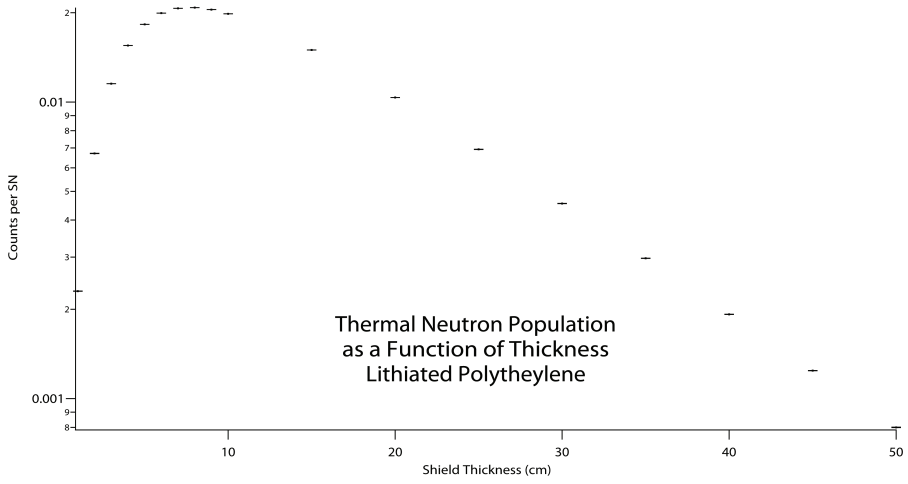

Figure 6.8. Thermal neutron population as function of thickness for a unenriched lithiated polytheylene shield.

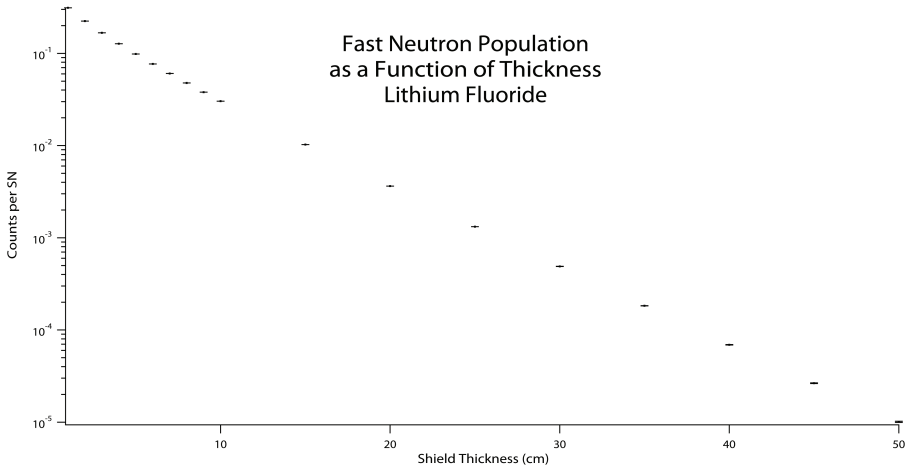

Figure 6.9. Fast neutron population as function of thickness for a lithium fluoride shield.

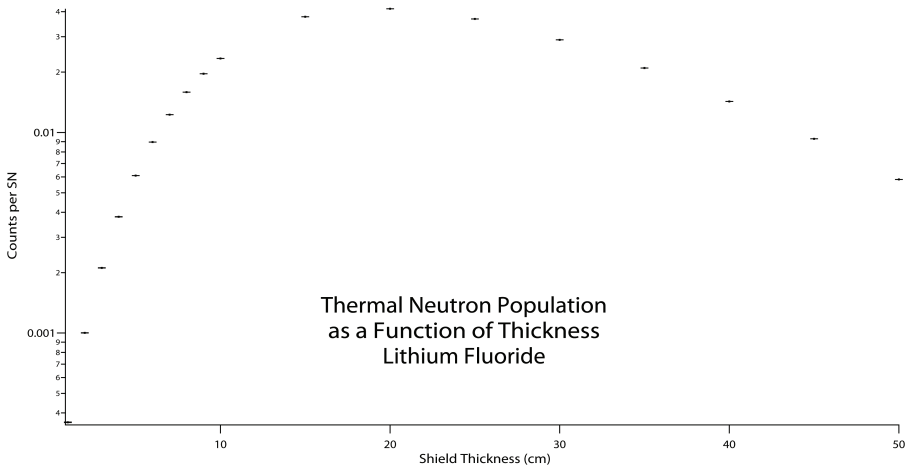

Figure 6.10. Thermal neutron population as function of thickness for a lithium fluoride shield.

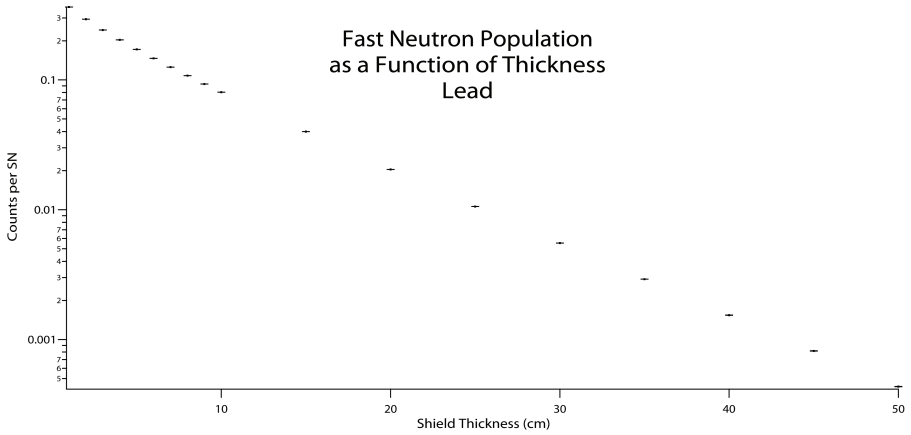

Figure 6.11. Fast neutron population as function of thickness for a lead shield.

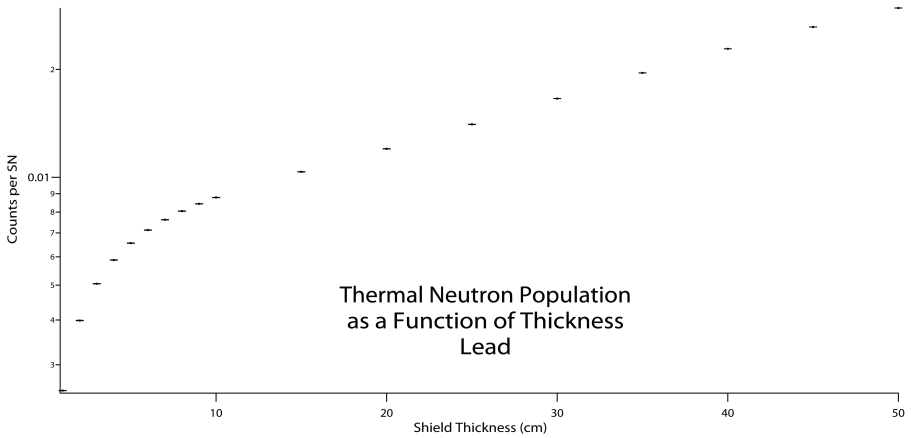

Figure 6.12. Thermal neutron population as function of thickness for a lead shield.

tered from the soil, and background gamma rays from the soil and any shielding material. At the same time, the shield must allow the passage of the 10.8 MeV gamma rays which serve as the trigger for the presence of explosives.

To best shield the detector from the neutrons produced by both the DT generator and secondary reactions within the soil, a plane of boron carbide will be placed above the neutron generator and soil.

Reduction of soil background

To test the reduction of both neutrons and gamma rays emitted by the soil, a 6 m x 6 m x 6 m cube of world average soil was created. Above this, a centimetre thick layer of air was placed which was also 6 m x 6 m. Above this, a boron carbide layer was placed of varying thickness, also 6 m by 6 m in extent. A neutron source was then placed which directed 14.1 MeV neutrons downward at the soil. An F1 tally of the neutron and gamma ray flux was then collected at the bottom air-boron carbide interface and another was collected at the top of the block of boron carbide. Both tallies were set up to tally only upward moving particles, that is gamma rays and neutrons entering the boron carbide and those leaving it, not those that are merely reflected by either surface.

The primary objective of the boron carbide shielding is to reduce the neutron population to limit damage and neutron interactions with the detectors. As boron carbide is a low average Z material, and gamma ray attenuation is proportional to Z^2, it will not strongly shield incident gamma rays. The mean free path of 10.8 MeV gamma rays in this material is 22 cm, meaning that the boron carbide shield can be made relatively thick without sacrificing significant signal. It will, however, provide greater protection against the low energy gamma rays which dominate the gamma ray background. The strong 511 keV background resulting from pair production, for example, has a mean free path of 5.2 cm in boron carbide.

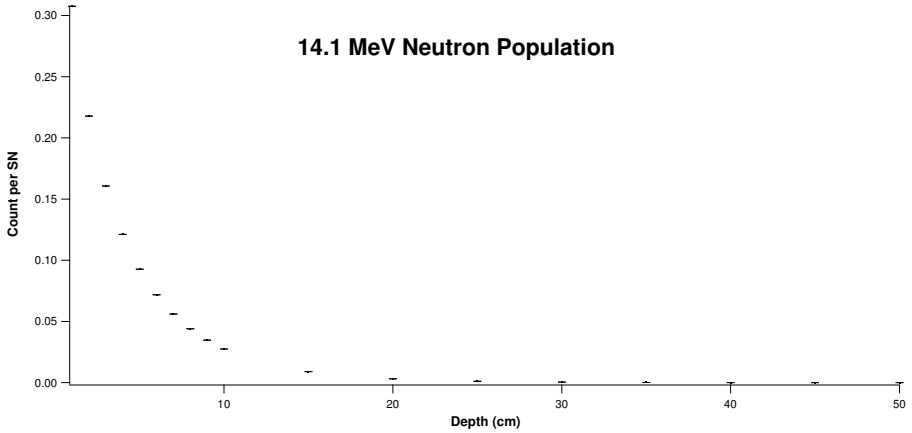

Figure 6.13. 14 MeV neutron population as a function of shielding thickness

Three different neutron populations were examined, including the original 14.1 MeV neutron population, the thermal neutron population, and the total neutron population. The population of each of these was collected using an F1 tally placed at the top of the boron carbide shield. Only upward moving neutrons were tallied using a cosine bin. The results can be seen in the Figs. 6.13 – 6.15. A thickness of 20 cm is sufficient to reduce the 14 MeV neutron population by two orders of magnitude, the thermal population by an order of magnitude, and the total neutron population by an an order of magnitude while retaining 40% of the 10.8 MeV gamma rays and reducing the low energy gamma ray background by roughly an order of magnitude.

Redection of Gamma Ray Backgrounds

In addition to excess neutrons, it would be ideal to reduce the number of gamma rays reaching the detectors to prevent afterglow effects as well as reduce the count rate from background, which could result in excessive detector dead time. Among the largest backgrounds are the 511 keV line generated by pair production reactions

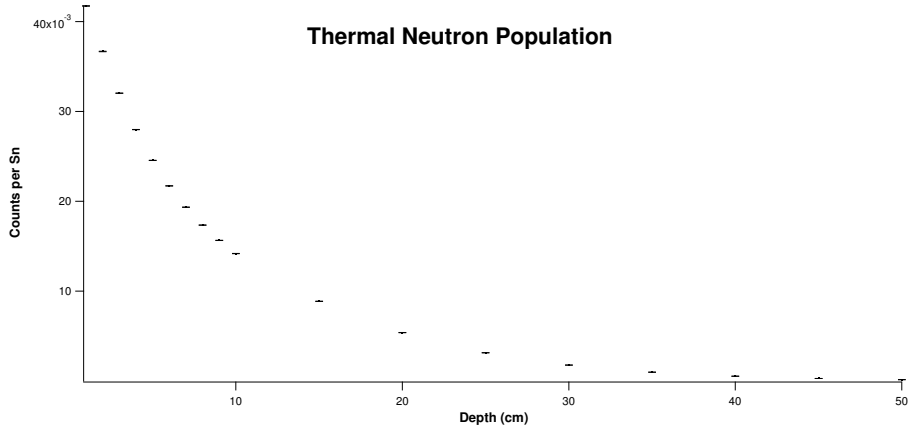

Figure 6.14. Thermal neutron population as a function of shielding thickness

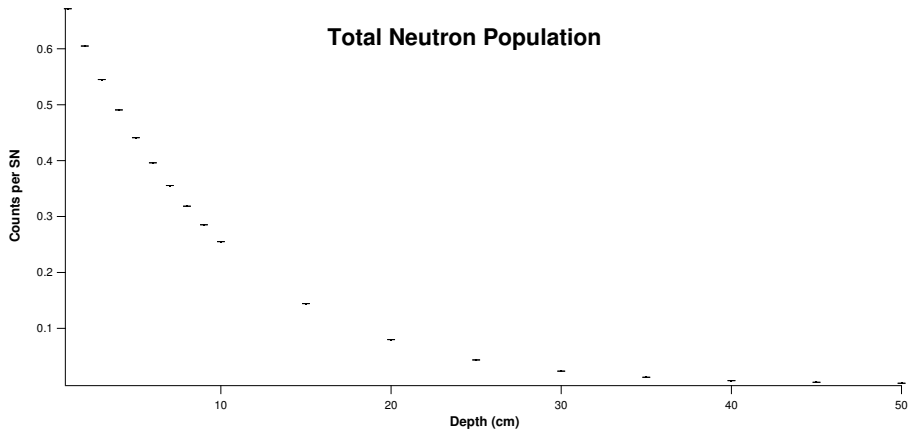

Figure 6.15. Total neutron population as a function of shielding thickness

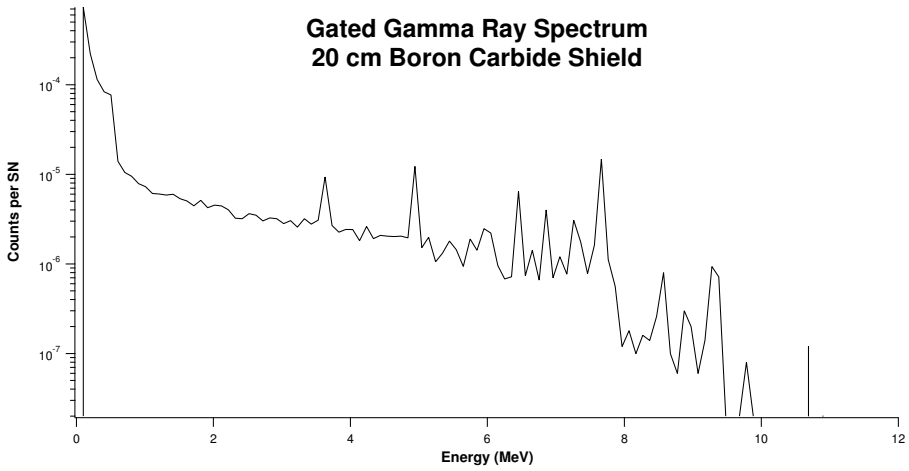

Figure 6.16. Gated gamma ray spectrum from a 20 cm boron carbide shield

in the soil. Taking a weighted average of the energy of the gamma rays that exit the 20 cm boron carbide shield after the timing gate begins, given by

$$\langle E \rangle = \frac{\sum_i E_i c_i}{\sum_i c_i} \tag{6.6}$$

where E_i is the energy of the ith bin and c_i is the number of counts yields an average energy of 760 keV. It would be desirable to reduce this background, however any shielding of this background will also result in attenuation of the 10.8 MeV gamma rays resulting from interaction with nitrogen within the explosives. However, reducing the incoming gamma rays will reduce the dead time experienced by the detector. As the spectra in Figs. 6.16 and 6.17 show, this spectrum is dominated by low energy gamma rays. These background low energy gamma rays are more easily shielding then the strong 10.8 MeV nitrogen line. The mean free path of 511 keV gamma rays in lead, is 0.71 cm and that for the average 760 keV gamma rays is 0.99 cm compared to 1.8 cm for 10.8 MeV gamma rays.

As an initial attempt to get an idea of the thickness required for a reasonable reduction of the gamma ray background, a layer of lead, a high Z material commonly

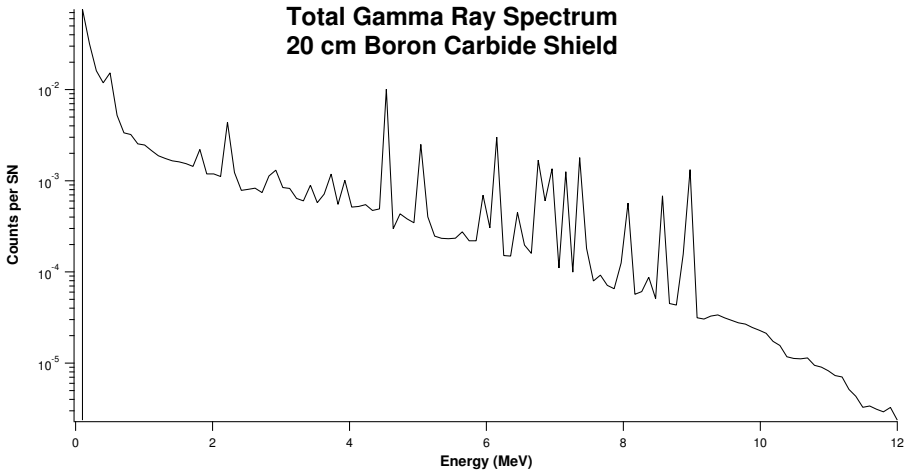

Figure 6.17. Total gamma ray spectrum from a 20 cm boron carbide shield

used to shield gamma rays, was placed directly above the layer of boron carbide. This layer covered the extent of the problem space in the xy plane, and was then extended along the z axis between 1 and 5 cm in 1 cm increments. The resulting gamma ray spectrum was collected at the top and bottom of the lead layer, with cosine binning set to collect only upward moving gamma rays.

While the addition of lead will reduce the overall strength of the dominant lower energy gamma ray background, it also adds the complication of reducing the solid angle each detector will represent. By necessity, the additional dimension in the z direction that the layer of lead adds will also move it farther from the ground and explosive. As a result, the solid angle each detector represents will decrease. As a result, the signal produced by the detector will also decrease. However, the parasitic material of the ground will continue to produce low energy background gamma rays through pair production. As the extent of the ground is much greater than that of the explosive, the effect of moving the detector farther away may not have as significant an effect as it does on the nitrogen signal. However it must be kept in mind that the population of neutrons producing this secondary radiation will also decrease as the distance to the neutron source is increased.

To fully understand this, a series of simulations were run in which a lead plate with dimensions 25 cm x 25 cm by a variable thickness was placed above the boron carbide neutron shield. Below the boron carbide shield, a 1 cm thick air layer was placed. This was followed by a 600 cm on side cube of soil containing a 10 cm in radius cylinder center on the z-axis of RDX that was 40 cm long to produce a nitrogen signal.

NaI detectors are limited to being able to count roughly 200,000 counts per second in typical spectroscopy applications without encountering excessive dead time which in turn will increase the effective collection time required to detect explosive. Thus, the goal of the lead gamma ray shielding is to decrease the total gamma ray count relative to the nitrogen signal count at 10.8 MeV.

Thickness (cm)	$R_{\gamma,N}$ (s^{-1})	$R_{\gamma,t}$ (s^{-1})	$\frac{R_{\gamma,N}}{R_{\gamma,t}}$
1	6.5×10^{-7}	7.40×10^{-5}	8.78×10^{-3}
2	3.5×10^{-7}	4.66×10^{-5}	7.51×10^{-3}
3	2×10^{-7}	2.96×10^{-5}	6.74×10^{-3}
4	1.1×10^{-7}	1.86×10^{-5}	5.92×10^{-3}
5	6×10^{-8}	1.19×10^{-5}	5.04×10^{-3}

Table 6.2.

Lead simulation results

Let c_t represent the total gamma ray count and c_N the total nitrogen gamma ray count, $R_{\gamma,t}$ the total gamma ray rate per source neutron, $R_{\gamma,N}$ the nitrogen gamma ray rate per source neutron, and R_G be the rate at which neutrons are produced by generator and t the amount of time the signal is observed. It is desirable to maximize the ratio of nitrogen counts to total counts, given by

$$\frac{c_N}{c_t} = \frac{R_{\gamma,N} R_G t}{R_{\gamma,t} R_G t} = \frac{R_{\gamma,N}}{R_{\gamma,t}} \tag{6.7}$$

The results of these simulations can be seen in Table 6.2. As is shown, the value of the ratio decreases with increasing thickness, indicating that the lead shielding does not assist in improving the signal strength by limiting incoming gamma rays, and so the use of lead shielding is detrimental and will not be used.

7. System Performance

Given the shielding design, the performance of the system is now considered. To do this, a deck was made consisting of a 4 m × 4 m × 4 m cube of soil, in which various explosives were placed. Three different devices were considered. These include an M107 155 mm shell, a VS-2.2 antitank mine, and a Mk-12 bomb. Also considered were different road surfaces, including dirt and conventional concrete. Simulations were run with the detection array 10.16 cm above the road surface. Each device was run with a depth, defined as the distance from the top of the ground-air interface to the surface of the object closest to ground-air surface. For the dirt road, depths of 1 cm, 15 cm, 30 cm, 45 cm, and 60 cm were used. For those with road surfaces, depths of 15 cm, 30 cm, 45 cm, and 60 cm were used as the road surface itself occupied the upper 10 cm.

7.1 Signal and background calculation

The heart of this system's performance is the reliance on the fact that thermal capture lines above 8 MeV are relatively rare. Unfortunately, the F8 tally, known as the energy deposition tally, which is used to mimic detector response in MCNP simulations does not allow time binning. As a result, it is not possible to use the F8 tally to simulate detector response in a system in which the detectors will be gated off, as is done in thermal neutron analysis to take advantage of the reduced background in the signal region above 8 MeV. Instead, the detector signal and background must be estimated using the gamma ray flux in to the detector array.

7.1.1 Photopeak efficiency calculation

This flux was collected by placing an F1 tally surrounding the detectors. The flux was cosine binned such that only particles entering the detectors were counted in the flux tally. To determine the number of gamma rays which will actually appear under the peak associated with the true energy of the 10.8 MeV signal and its 10.6 MeV silicon background, simulations were run for a 10.16 cm $\times$ 10.16 cm $\times$ 40.64 cm NaI detector. An F8 energy deposition tally was conducted for varying angles with respect to the surface of the surface of the detector. The entrance point was varied across the surface, and runs were made with the incoming angle θ such that $-80^{\circ} \leq \theta \leq 80^{\circ}$ in increments of 10°. These tallies were collected with the half distance of the detector cut in to thirds, and a collection of tallies was made for each of 9 points, including the detector's center point. To determine the average full photopeak efficiency, the total counts under the peak were found for each angle and position, and the efficiency determined. The average efficiency of the detector was found by taking the mean of all the efficiency values over all positions and angles. This average value was determined to be 9.5% $\pm$ 0.11%. This value will be used to determine the number of signal and background gamma rays which enter the detector and are detected by it.

7.1.2 Signal Estimation

The surface flux on the detectors must be utilized to estimate the signal as the energy deposition tally does not allow time binning, and thus cannot provide a simulation of the signal produced in the detectors in pulsed mode operation, as collection of spectra in the detectors cannot be limited in time, but instead collect over the duration of the simulation. The flux spectrum will be missing two important features of the energy deposition in to the detector and thus the resulting spectrum, the efficiency of the detector as well as the broadening of lines associated with imperfect collection of the energy of each gamma ray.

To accomplish this estimation, a series of simulations was conducted. In these simulations, a photon source was placed which corresponded to one of the 256 different bin energies from the surface flux. The position of this source was moved across nine different locations evenly distributed on the detector face. For each of these locations, the angle was varied from -80° to 80° in 10° degree increments. The results for these simulations for each bin energy were then averaged over all locations and angles. This allows the estimated detector response to take in to account the effects of the Compton continuum, detection efficiency, as well as the first and second escape peaks for all bins across the entire surface flux. Let $c_i^{'}$ be the resultant count in the ith bin of the spectrum, c_j be the original count in the jth bin of the flux tally, and $\epsilon_{i,j}$ be the simulated count per source gamma in the ith energy bin in the detector response simulation for a gamma ray in the jth energy bin in the flux tally. The resulting altered count is then

$$c_i^{'} = \sum_{j=1}^{N} \epsilon_{i,j} c_j \tag{7.1}$$

In addition, Gaussian broadening of each bin must be taken in to account. This can be simulated by using the known dependence of resolution on the energy of the measured photon. This dependence is expressed as

$$\text{FWHM} = a + b\sqrt{E + cE^2} \tag{7.2}$$

where $a = -0.00789$ MeV $b = 0.06769$ MeV$^{\frac{1}{2}}$ $c = 0.21159$ MeV^{-1} are the values of the parameters for NaI detectors [53]. Using this formula, the resolution at any given point in the spectrum can be calculated. The counts may then be redistributed among the bins by generating a Gaussian distribution for each point, then redistributing the counts in bins with corresponding energies. This can be done for each bin resulting from the F1 tally, resulting in a broadened spectrum. Given the combination of the simulated detection efficiencies, Compton continuum, escape peaks, and Gaussian broadening, the resultant modified surface flux should provide an estimated detector response which closes follows the true behaviour of an NaI detector in a gated detection system.

7.2 Decision Parameter

Given the computed spectrum, it must then be decided if the counts within the region of interest are significant. The number of counts under the peak above background may be estimated as

$$C_s = P - \frac{n}{2}(B_1 + B_2) \tag{7.3}$$

where $P = \sum_{i=B_1+1}^{B_2-1} c_i$ if c_i is the number of counts in the ith bin, B_1 the number of counts in the bin outside of the region of interest to the left of the peak, and B_2 is the number of counts just outside the right of the peak, and n is the number of bins between B_1 and B_2.

The significance of this signal, θ, is then given by

$$\theta = \frac{C_s}{\delta C_s} = \frac{P - \frac{n}{2}(B_1 + B_2)}{\sqrt{P + \left(\frac{n}{2}\right)^2 (B_1 + B_2)}} \tag{7.4}$$

Rewritten in terms of rates,

$$\theta = \sqrt{N_n}\frac{R_P - \frac{n}{2}(R_{B_1} + R_{B_2})}{\sqrt{R_P + \left(\frac{n}{2}\right)^2 (R_{B_1} + R_{B_2})}} \tag{7.5}$$

where N_n is the total number of neutrons released. Solving for t, The number of neutrons released and the time required must then be determined. The maximum generator rate will be determined by the maximum number of counts per second that the detector can tolerate without excessive dead time due to pulse pile up. The characteristic decay time for a light pulse in a NaI detector is 250 ns. Assuming Poisson distributed counts, the probability of one count or more during the light pulse decay is

$$P = 1 - e^{-r\tau_d} \tag{7.6}$$

Thus,

$$r = -\frac{\ln(1 - P)}{\tau_d} \tag{7.7}$$

Assuming a 5% chance is acceptable, this amounts to a rate of 200,000 cps. The detector rate, R_D is related to the generator rate by $R_{\gamma,A}$, the total number of gammas deposited per source neutron across all energy bins, by

$$R_D = R_G R_{\gamma,A} \tag{7.8}$$

So

$$R_G = \frac{R_D}{R_{\gamma,A}} \tag{7.9}$$

In pulsed mode operation, the generator is also only on for a portion of the collection cycle. Let t_a be the duration per pulse that the generator is on, and t_c be the total length of the cycle. Then the number of neutrons released per cycle is

$$N_{n,c} = R_G t_a = \frac{R_D}{R_{\gamma,A}} t_a \tag{7.10}$$

The total number of neutrons released after a time t is then

$$N_n = N_{n,c}\frac{t}{t_c} = \frac{R_D}{R_{\gamma,A}} t_a \frac{t}{t_c} = \frac{t_a}{t_c}\frac{R_D}{R_{\gamma,A}} t = \beta t \tag{7.11}$$

Substituting the expression in Eq. 7.2 back in to Eq. 7.2 yields

$$\theta = \sqrt{\beta t}\frac{R_P - \frac{n}{2}\left(R_{B_1} + R_{B_2}\right)}{\sqrt{R_P + \left(\frac{n}{2}\right)^2\left(R_{B_1} + R_{B_2}\right)}} \tag{7.12}$$

Solving for t yields

$$t = \frac{\theta^2}{\beta}\frac{R_P + \left(\frac{n}{2}\right)^2\left(R_{B_1} + R_{B_2}\right)}{\left[R_P - \frac{n}{2}\left(R_{B_1} + R_{B_2}\right)\right]^2} \tag{7.13}$$

For a significance of 2.5, there is a 98.8% chance that the signal is not due to statistical fluctuation. This level of significance will be use to determine detection time. The signal region is selected to be $\pm 2\sigma$ of the 10.8 MeV energy signal.

The probability that the signal is due to background is also calculated. Each bin is assumed to be Gaussian distributed. The probability that the fluctuation is given by

$$P = \frac{1}{\sigma_b\sqrt{\pi}}\int_{c_s}^{\infty} e^{-\frac{1}{2}\left(\frac{x-c_b}{2\sigma_b}\right)^2} dx$$

$$P = \frac{1}{2}\left[1 - \mathrm{erf}\left(\frac{c_s - c_b}{\sigma_b}\right)\right] \tag{7.14}$$

where c_b is the background count, σ_b the error in that count, and c_s is the error in that count.

7.3 Results

7.3.1 Detection time with NaI Detectors

The calculation above was computed for an M-107 shell, Mk-12 bomb, and VS-2.2 mine model on a dirt road at 1, 15, 30, 45, and 60 cm and 15, 30, 45, and 60 cm for a concrete road surface. As can be seen from tables 7.1 and 7.2, detection times vary from 5 minutes to times well beyond practical detection times. Detection for most devices is possible up to roughly 30 cm, however beyond that the signal falls below practical detection levels.

Surprisingly, this is not due primarily to the concentration of silicon in the soil and road surface. It can be seen from Fig. 7.2 that the counts with no explosive present are small in the signal region relative to the counts that result from the explosive presence, even in the 30 cm case of the Mk-12 bomb. Instead, the primary difficult in detecting the explosive arises not from the ^{29}Si background, but rather the first escape peak of nitrogen from the explosive itself. The nitrogen first escape peak occurs at 10.3 MeV, that for silicon at 10.6 MeV, and that for the primary photopeak at 10.8 MeV, placing the silicon background nearly in the middle of the primary and first escape peak of nitrogen. The resulting effect is to fill in additional counts between the primary and first escape peaks of nitrogen, making both peaks indistinct, resulting in the difficulty of detecting the peak in NaI, due to its poor resolution.

This can be seen in Fig. 7.1. Both the 10.8 MeV primary photopeak of nitrogen and its first escape peak at 10.3 MeV decrease in strength in the presence of the concrete road surface. This is likely a result of capture on the additional hydrogen

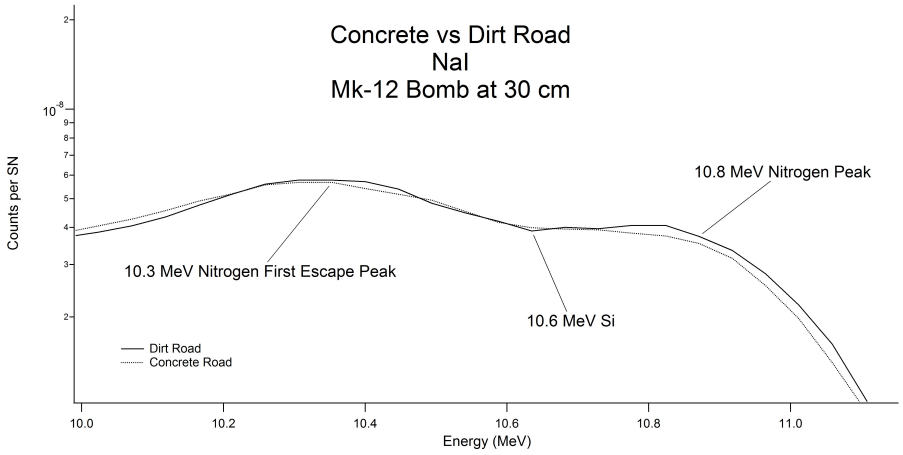

Figure 7.1. Differences in sodium iodide spectra for concrete and dirt roads

in concrete compared to average soil. The resulting additional 10.6 MeV gamma rays also increase, the result being that the two nitrogen peaks are suppressed while the background between them is increased, resulting in two peaks which are far less distinct than without the concrete, causing the difficulty in detecting explosive in the presence of concrete. Because of this effect, the probability that the counts in the region as calculated by Eq. 7.2 is essentially zero for all tested cases, yet detection time is excessive.

The difficulty caused is due directly to the poor energy resolution of the NaI detectors. If microphonics, cooling requirement, and additional cost of HPGe detectors can be ignored, they provide far superior performance to that of NaI, as the primary and first escape peaks of nitrogen and the 10.6 MeV silicon line are all fully resolved.

7.3.2 Detection time with HPGe Detectors

To estimate the detection time with HPGe, a similar procedure to that followed for NaI was followed. While the resolution of NaI is 390 keV at 10 MeV, that for HPGe is 20 keV at the same energy [55], a considerable improvement.

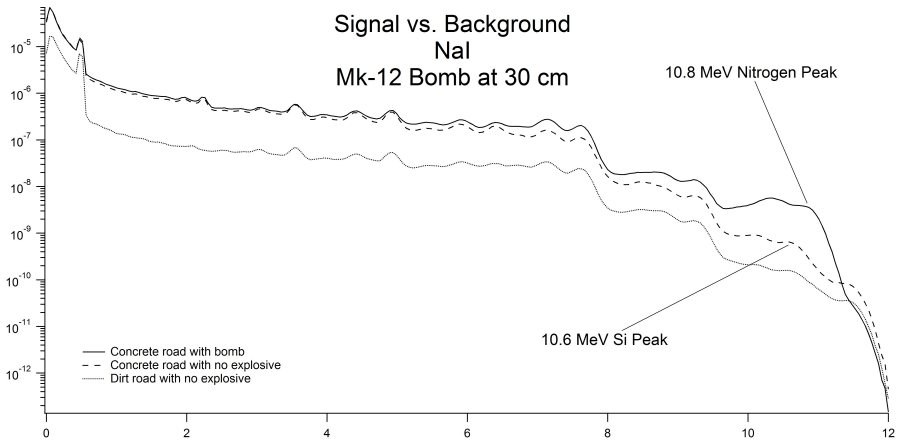

Figure 7.2. Sodium iodide signal vs. background

The simulated detectors' dimensions are based on the Ortec GEM-F8250P4-PLB-S. The Gaussian energy broadening constants are given by $a = 0.0011265$ MeV $b = 0.0012670$ MeV$^{\frac{1}{2}}$ $c = 0.00127429$ MeV^{-1} [56]. Samples of the detector's response were taken centered on the face of the detector, and then at radii of 1.36 and 2.71 cm, dividing the face of the detector roughly by thirds.

The maximum count rate for this system is primarily limited by the fall time of the preamplifier. Ortec, a major producer of HPGe detectors, indicates their preamps to have an energy rate limit of 145,000 MeV/sec [57]. The weight average energy in the worst case scenario from the spectra obtained from simulation is 835 keV, yielding a maximum rate of 173,000 cps. To ensure limited dead time, a rate of 40,000 cps was selected for the computation of detection time.

The resulting improved energy resolution completely resolves the ^{14}N primary and first escape peaks and the ^{29}Si peak, as shown in Fig. 7.3. The result is a substantial improvement detection time as a result, especially in the concrete road case. This is particularly obvious when the spectrum for HPGe and that for NaI is compared, as shown in Fig. 7.4. The resulting nitrogen peak, despite the significant burial depth, is still plainly visible and resolved from the silicon background, resulting in far superior detection time. Again, the counts under this peak are significantly above the background count obtained from a soil cube with no explosive present, resulting in essentially zero probability of a detection resulting from background as computed by Eq. 7.2.

7.4 Possible Improvements

The excess signal detection times are owed largely to the low energy resolution of the detectors. As a result, it is likely preferred to switch to a higher energy resolution detectors. While HPGe may be difficult to implement given the constraints regarding noise generated by microphonics, the poor count rate, the poor efficiency, as well as the requirement that these detectors remain at liquid nitrogen temperatures, they

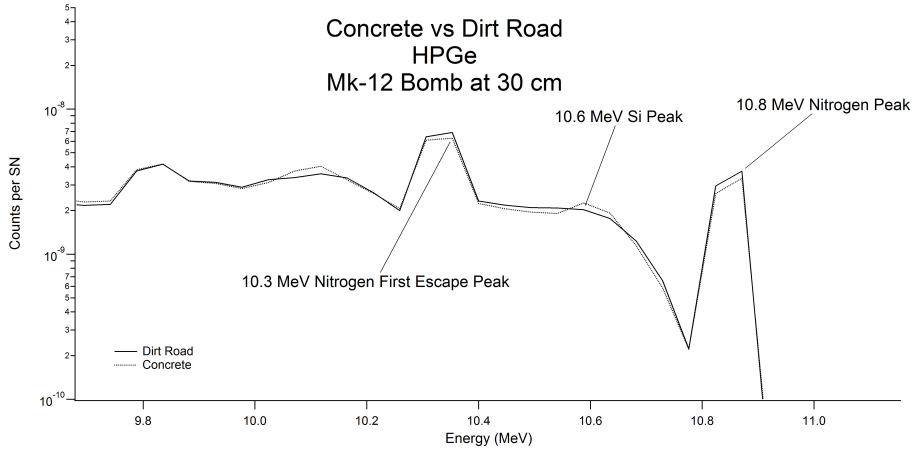

Figure 7.3. Differences in HPGe spectra for concrete and dirt roads

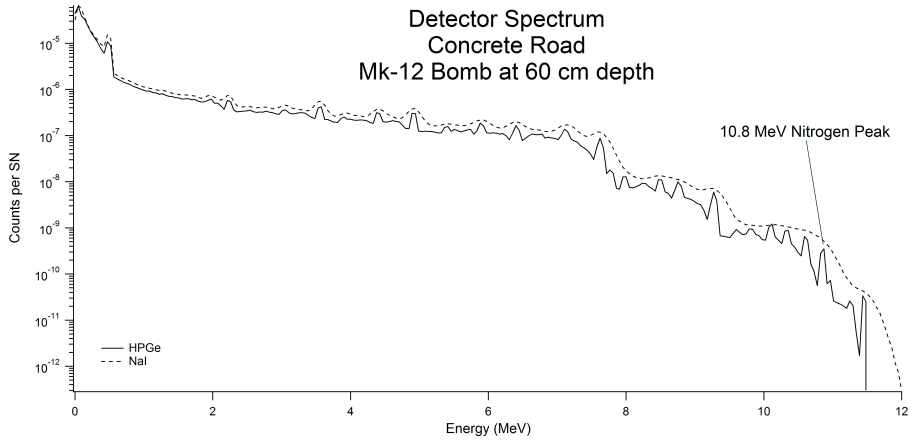

Figure 7.4. Comparison of spectra for NaI and HPGe for a Mk-12 bomb at 60 cm depth

Depth (cm)	Detection Time (NaI) (s)	Detection Time (HPGe) (s)
Mk-12 Bomb		
1	277	15.6
15	459	22.4
30	1330	39.2
45	2040	82.2
60	2770	241
M-107 Shell		
1	553	27.6
15	788	47.7
30	1310	90.4
45	4160	271
60	27200	697
VS-2.2 Mine		
1	481	29.6
15	889	65.0
30	3370	150
45	16800	306
60	117000	1800

Table 7.1.
Detection times for various devices on a dirt road

Depth (cm)	Detection Time (NaI) (s)	Detection Time (HPGe) (s)
Mk-12 Bomb		
15	1170	46.1
30	4820	124
45	10700	470
60	435000	1760
M-107 Shell		
15	3300	97.1
30	8540	319
45	72100	1050
60	–	7750
VS-2.2 Mine		
15	5140	143
30	46700	547
45	104000	1290
60	–	3840

Table 7.2.
Detection times for various devices on a concrete road

would provide considerable improvement in the detection time if feasible, considering the resolution is 20 keV at 10 MeV [55], a considerable improvement over the 390 keV of NaI. The resulting improved energy resolution would completely resolve the ^{14}N and ^{29}Si peaks, reducing detection time by one to two orders of magnitude.

Another possibility would be the substitution of scintillators based on lanthanum halides, especially LaBr and LaCl. These scintillators do not require cooling and have superior characteristics compared to NaI. LaBr has a superior light decay constant of 16 ns and LaCl 28 ns, compared to 250 ns for NaI, which will allow higher count rates than those available with NaI detectors. The light yield is also superior, with 63,000 photons/MeV released for LaBr and 49,000 photons/MeV for LaCl, compared to 38,000 photons/MeV for NaI. This superior light yield should also increase energy resolution of the detectors. While the densities of NaI and LaCl are comparable, that of LaBr is 5.08 g/cm^3, an approximately 40% increase over that of NaI, which will also increase the efficiency of the detector [41, 58]. The only difficulty associated with these types of detectors is they cost 7 - 17 times as much as NaI detectors and moreover are less commercially available in larger sizes as a result of their relatively recent introduction to the market.

APPENDIX

A. Sample MCNP5 Decks

A.1 Timing Gate

```
 Timing gate experiment
c -=-=-=-=-=-=-=-=-=-=-=-=-=-=-=-=-=-=-=-=-=-=-=-=-=-=-=-=-
c Cell cards - origin at center of sphere
c -=-=-=-=-=-=-=-=-=-=-=-=-=-=-=-=-=-=-=-=-=-=-=-=-=-=-=-=-
 1001 301 -0.0012 +2008 -2301 +2004 -2003 +2006 -2005
 1002 301 -0.0012 +2301 -2007 +2004 -2003 +2006 -2005
 1003 306 -2.26 +2001 -2008 +2004 -2003 +2006 -2005
 1011 322 -1.4 +2201 -2001 +2002 +2004 -2003 +2006 -2005
 1012 322 -1.4 -2201 +2004 -2202
 1013 322 -1.4 -2201 +2203 -2003
 1021 303 -1.82 -2101 +2102 -2103
 1031 320 -7.85 +2101 -2201 +2202 -2203
 1032 320 -7.85 -2101 +2202 -2102
 1033 320 -7.85 -2101 +2103 -2203
 1999 0 -2002:+2007:-2004:+2003:-2006:+2005

c -=-=-=-=-=-=-=-=-=-=-=-=-=-=-=-=-=-=-=-=-=-=-=-=-=-=-=-=-
c Surface cards
c -=-=-=-=-=-=-=-=-=-=-=-=-=-=-=-=-=-=-=-=-=-=-=-=-=-=-=-=-
 2001 PZ 0
 2301 PZ 11.16
 2002 Pz -600
 2401 PZ -10
```

```
 2302 PZ -20
 2303 PZ -30
 2304 PZ -40
 2305 PZ -50
 2306 PZ -60
 2003 Px 300
 2004 PX -300
 2005 PY 300
 2006 PY -300
 2007 PZ 600
 2008 PZ 10.16
 2009 PZ 15.16
 2101 C/X 0 -39.017 7.747
 2102 PX -30.2641
 2103 PX +30.2641
 2201 C/X 0 -39.017 9.017
 2202 PX -31.5341
 2203 PX +31.5341


c -=-=-=-=-=-
c Data cards
c -=-=-=-=-=-
c BEGIN MATERIALS
c -----------------------------------
c Air (80% N, 20% O; 0.0012 g/cc)
c -----------------------------------
 m301 07014.62c -0.75086
      08016.62c -0.23555
      18000.42c -0.01281
```

```
      01001.62c -0.00064
      06000.24c -0.00014
c -----------------------------------
c RDX c3H6N6O6
c Density: 1.82 g/cc
c -----------------------------------
 m303 6000.60c 3
      1001.50d  6
      7014.62c 6
      8016.60c 6
c -----------------------------------
c HMX c4H8N8O8
c Density: 1.91 g/cc
c -----------------------------------
 m304 6000.60c 4
      1001.50d  8
      7014.62c 8
      8016.60c 8
c -----------------------------------
c ANFO
c Data from:
c Explosives Detection and Identification by PGNAA
c by EH Seabury and AJ Caffrey
c Density: 0.84 g/cc for mining grade
c -----------------------------------
  m305 6000.60c -0.026
       1001.50d -0.054
       7014.62c -0.339
       8016.60c -0.581
```

```
c -----------------------------------
c Nitrogen for F4 tally
c -----------------------------------
 m399 7014.62c 1
c -----------------------------------
c Conventional Concrete
c Data from:
c Neutron Scattering in Concrete and Wood
c A Facure, A X Silvia, C Falcao, and V R Crispim
c Radiation Protection Dosimetry 119 (2006) pp 514-517
c Density: 2.26 g/cc
c -----------------------------------
 m306 1001.62c -0.0055
      8016.60c -0.4957
      11023.62c -0.0170
      19000.62c -0.0191
      12000.62c -0.0026
      13027.42c -0.0455
      14028.24c -0.2892
      14029.24c -0.01469
      14030.24c -0.009680
      16000.62c -0.0013
      20000.62c -0.0826
      26054.60c -7.189e-4
      26056.60c -0.01129
      26057.60c -2.606e-4
      26058.62c -3.469e-5
c -----------------------------------
c 10% water moist sand
```

```
C Density: 1.702 g/cc
c -----------------------------------
 m315 1001.62c -0.011898
      8016.60c -0.5698119
      14028.24c -0.420687
c -----------------------------------
c World average soil
c Source:
c Basic Considerations for Monte Carlo Calculations in Soil
c Applied Radiation and Isotopes 62 (2005) 97-107
c Typical density = 1.2 - 1.6 g/cc
c Isotope abundance data from It's Elemental
c education.jlab.org/itselemental
c -----------------------------------
 m319 3006.66c -2.25e-6
      3007.66c -2.775e-6
      5010.66c -1.98e-6
      5011.60c -8.02e-6
      6012.50c -0.0198
      6013.42c -2.22e-4
      7014.60c -9.96e-4
      7015.66c -3.66e-6
      8016.60c -0.4875
      8017.66c -1.86e-4
      9019.62c -2.0e-4
      11023.62c -0.0063
      12000.62c -0.005
      13027.42c -0.071
      14028.24c -0.307
```

```
14029.24c -0.0156
14030.24c -0.0103
15031.50c -6.5e-4
17000.64c -1.0e-4
19000.62c -0.014
20000.62c -0.0137
21045.62c -7.0e-6
22000.62c -0.0050
23000.62c -1.0e-4
24050.60c -4.35e-5
24052.60c -8.38e-4
24053.60c -9.50e-5
24054.60c -2.37e-5
25055.62c -8.5e-4
26054.60c -0.00222
26056.60c -0.0349
26057.60c -6.357e-4
26058.62c -1.072e-4
27059.66c -8.0e-6
28000.50c -4.0e-5
29000.50c -2.0e-5
37085.66c -7.217e-5
37087.66c -2.783e-5
39089.42c -5.0e-5
40090.66c -1.544e-4
40091.66c -3.366e-5
40092.66c -5.1454e-4
40094.66c -5.214e-5
40096.66c -8.4e-6
```

```
      56138.66c -5.0e-4
      72000.60c -6.0e-6
      82000.42c -1.0e-5
      90232.60c -5.0e-6
c -----------------------------------
c
c A36 Steel
c From ASTM spec sheet
c Density: 7.85 g/cc
c
c -------------------------------------
 m320 6012.50c -0.0025
      29000.50c -0.0020
      26054.60c -0.057281
      26056.60c -0.89919
      26057.60c -0.020766
      26058.62c -0.0027636
      25055.62c -0.0103
      15031.50c -0.00040
      14028.24c -0.0025824
      14029.24c -0.000131124
      14030.24c -8.6436e-5
c -----------------------------------
c
c Typical Western US Earth
c From PNNL 15870 Rev 1
c Density: 1.52 g/cc
c
c -----------------------------------
```

```
 m321 1001 -0.023834
      8016 -0.598898
      13027 -0.080446
      14000 -0.296821
c -----------------------------------
c
c World Average soil, 10 percent moisture
c Density: 1.4 g/cc
c
c -----------------------------------
 m322 1001.62c -0.011190
      3006.66c -2.03e-6
      3007.66c -2.4975e-6
      5010.66c -1.782e-6
      5011.60c -7.218e-6
      6012.50c -0.01782
      6013.42c -1.998e-4
      7014.60c -8.64e-4
      7015.66c -3.294e-6
      8016.60c -0.527349
      8017.66c -2.01148e-4
      9019.62c -1.8e-4
      11023.62c -0.00567
      12000.62c -0.0045
      13027.42c -0.0639
      14028.24c -0.2763
      14029.24c -0.01404
      14030.24c -0.00927
      15031.50c -5.85e-4
```

```
17000.64c -9e-5
19000.62c -0.0126
20000.62c -0.01233
21045.62c -6.3e-6
22000.62c -0.0045
23000.62c -9.0e-5
24050.60c -3.915e-5
24052.60c -7.542e-4
24053.60c -8.550e-5
24054.60c -2.133e-5
25055.62c -7.65e-4
26054.60c -0.001998
26056.60c -0.03141
26057.60c -5.7213e-4
26058.62c -9.648e-5
27059.66c -7.2e-6
28000.50c -3.6e-5
29000.50c -1.8e-5
37085.66c -6.4953e-5
37087.66c -2.5047e-5
39089.42c -4.5e-5
40090.66c -1.3896e-4
40091.66c -3.029e-5
40092.66c -4.63086e-4
40094.66c -4.6926e-5
40096.66c -7.56e-6
56138.66c -4.5e-4
72000.60c -5.4e-6
82000.42c -9.0e-6
```

```
      90232.60c -4.5e-6
c
c END MATERIALS
c -----------------------------------
c -----------------------------------
c Begin data cards
c -----------------------------------
 mode n p
 phys:p
 nps 1e9
c ctme 1000
 imp:n 1 9r 0
 imp:p 1 9r 0
 sdef pos=0 0 20.16 erg=14
c PTRAC file=asc max=1e6 nps=1,200 type=n write=all
 print
c -----------------------------------
c Tallies
c -----------------------------------
 F021:P 2301
 E021 3e-8 118i 12 T
 T021 1000 2000 T
 F031:P 2301
 E031 3e-8 118i 12 T
 T031 1000 3000 T
 F041:P 2301
 E041 3e-8 118i 12 T
 T041 1000 4000 T
 F051:P 2301
```

```
E051 3e-8 118i 12 T
T051 1000 5000 T
F061:P 2301
E061 3e-8 118i 12 T
T061 1000 6000 T
F071:P 2301
E071 3e-8 118i 12 T
T071 1000 7000 T
F081:P 2301
E081 3e-8 118i 12 T
T081 1000 8000 T
F091:P 2301
E091 3e-8 118i 12 T
T091 1000 9000 T
F101:P 2301
E101 3e-8 118i 12 T
T101 1000 10000 T
F111:P 2301
E111 3e-8 118i 12 T
T111 1000 11000 T
F121:P 2301
E121 3e-8 118i 12 T
T121 1000 12000 T
F131:P 2301
E131 3e-8 118i 12 T
T131 1000 13000 T
F141:P 2301
E141 3e-8 118i 12 T
T141 1000 14000 T
```

```
 F151:P 2301
 E151 3e-8 118i 12 T
 T151 1000 15000 T
 F161:P 2301
 E161 3e-8 118i 12 T
 T161 1000 16000 T
 F171:P 2301
 E171 3e-8 118i 12 T
 T171 1000 17000 T
 F181:P 2301
 E181 3e-8 118i 12 T
 T181 1000 18000 T
 F191:P 2301
 E191 3e-8 118i 12 T
 T191 1000 19000 T
 F201:P 2301
 E201 3e-8 118i 12 T
 T201 1000 20000 T
c -=-=-=-=-=-=-=-=-
c End of Input Deck
c -=-=-=-=-=-=-=-=-
```

A.2 Shielding Calculations

```
 Boron Poly Thickness
c -=-=-=-=-=-=-=-=-=-=-=-=-=-=-=-=-=-=-=-=-=-=-=-=-=-=-=-=-=-=-=-=-=-=-=-=-
c Cell cards - origin at center of sphere
c -=-=-=-=-=-=-=-=-=-=-=-=-=-=-=-=-=-=-=-=-=-=-=-=-=-=-=-=-=-=-=-=-=-=-=-=-
 1101 324 -1.00 +2002 -2003 +2005 -2006 +2007 -2008
```

```
 1102 0 +2001 -2002 +2005 -2006 +2007 -2008
 1103 0 +2003 -2004 +2005 -2006 +2007 -2008
 1999 0 -2001:+2004:-2005:+2006:-2007:+2008

c -=-=-=-=-=-=-=-=-=-=-=-=-=-=-=-=-=-=-=-=-=-=-=-=-=-=-=-=-=-=-=-=-=-=-
c Surface cards
c -=-=-=-=-=-=-=-=-=-=-=-=-=-=-=-=-=-=-=-=-=-=-=-=-=-=-=-=-=-=-=-=-=-=-
 2001 PZ -1
 2002 PZ 0
 2003 PZ 10
 2004 PZ 11
 2005 PX -500
 2006 PX 500
 2007 PY -500
 2008 PY 500

c -=-=-=-=-=-
c Data cards
c -=-=-=-=-=-
c BEGIN MATERIALS
c -----------------------------------
c Air (80% N, 20% O; 0.0012 g/cc)
c -----------------------------------
 m301 07014.62c -0.75086
      08016.62c -0.23555
      18000.42c -0.01281
      01001.62c -0.00064
      06000.24c -0.00014
c -----------------------------------
```

```
c RDX c3H6N6O6
c Density: 1.82 g/cc
c -----------------------------------
 m303 6000.60c 3
      1001.50d  6
      7014.62c 6
      8016.60c 6
c -----------------------------------
c HMX c4H8N8O8
c Density: 1.91 g/cc
c -----------------------------------
 m304 6000.60c 4
      1001.50d  8
      7014.62c 8
      8016.60c 8
c -----------------------------------
c ANFO
c Data from:
c Explosives Detection and Identification by PGNAA
c by EH Seabury and AJ Caffrey
c Density: 0.84 g/cc for mining grade
c -----------------------------------
  m305 6000.60c -0.026
       1001.50d -0.054
       7014.62c -0.339
       8016.60c -0.581
c -----------------------------------
c Nitrogen for F4 tally
c -----------------------------------
```

```
 m399 7014.62c 1
c -----------------------------------
c Conventional Concrete
c Data from:
c Neutron Scattering in Concrete and Wood
c A Facure, A X Silvia, C Falcao, and V R Crispim
c Radiation Protection Dosimetry 119 (2006) pp 514-517
c Density: 2.26 g/cc
c -----------------------------------
 m306 1001.62c -0.0055
      8016.60c -0.4957
      11023.62c -0.0170
      19000.62c -0.0191
      12000.62c -0.0026
      13027.42c -0.0455
      14028.24c -0.2892
      14029.24c -0.01469
      14030.24c -0.009680
      16000.62c -0.0013
      20000.62c -0.0826
      26054.60c -7.189e-4
      26056.60c -0.01129
      26057.60c -2.606e-4
      26058.62c -3.469e-5
c -----------------------------------
c 10% water moist sand
C Density: 1.702 g/cc
c -----------------------------------
 m315 1001.62c -0.011898
```

```
      8016.60c -0.5698119
      14028.24c -0.420687
c -----------------------------------
c World average soil
c Source:
c Basic Considerations for Monte Carlo Calculations in Soil
c Applied Radiation and Isotopes 62 (2005) 97-107
c Typical density = 1.2 - 1.6 g/cc
c Isotope abundance data from It's Elemental
c education.jlab.org/itselemental
c -----------------------------------
 m319 3006.66c -2.25e-6
      3007.66c -2.775e-6
      5010.66c -1.98e-6
      5011.60c -8.02e-6
      6012.50c -0.0198
      6013.42c -2.22e-4
      7014.60c -9.96e-4
      7015.66c -3.66e-6
      8016.60c -0.4875
      8017.66c -1.86e-4
      9019.62c -2.0e-4
      11023.62c -0.0063
      12000.62c -0.005
      13027.42c -0.071
      14028.24c -0.307
      14029.24c -0.0156
      14030.24c -0.0103
      15031.50c -6.5e-4
```

```
17000.64c -1.0e-4
19000.62c -0.014
20000.62c -0.0137
21045.62c -7.0e-6
22000.62c -0.0050
23000.62c -1.0e-4
24050.60c -4.35e-5
24052.60c -8.38e-4
24053.60c -9.50e-5
24054.60c -2.37e-5
25055.62c -8.5e-4
26054.60c -0.00222
26056.60c -0.0349
26057.60c -6.357e-4
26058.62c -1.072e-4
27059.66c -8.0e-6
28000.50c -4.0e-5
29000.50c -2.0e-5
37085.66c -7.217e-5
37087.66c -2.783e-5
39089.42c -5.0e-5
40090.66c -1.544e-4
40091.66c -3.366e-5
40092.66c -5.1454e-4
40094.66c -5.214e-5
40096.66c -8.4e-6
56138.66c -5.0e-4
72000.60c -6.0e-6
82000.42c -1.0e-5
```

```
      90232.60c -5.0e-6
c -----------------------------------
c
c A36 Steel
c From ASTM spec sheet
c Density: 7.85 g/cc
c
c -----------------------------------
 m320 6012.50c -0.0025
      29000.50c -0.0020
      26054.60c -0.057281
      26056.60c -0.89919
      26057.60c -0.020766
      26058.62c -0.0027636
      25055.62c -0.0103
      15031.50c -0.00040
      14028.24c -0.0025824
      14029.24c -0.000131124
      14030.24c -8.6436e-5
c -----------------------------------
c
c Typical Western US Earth
c From PNNL 15870 Rev 1
c Density: 1.52 g/cc
c
c -----------------------------------
 m321 1001 -0.023834
      8016 -0.598898
      13027 -0.080446
```

```
      14000 -0.296821
c -----------------------------------
c
c World Average soil, 10 percent moisture
c Density: 1.4 g/cc
c
c -----------------------------------
 m322 1001.62c -0.011190
      3006.66c -2.03e-6
      3007.66c -2.4975e-6
      5010.66c -1.782e-6
      5011.60c -7.218e-6
      6012.50c -0.01782
      6013.42c -1.998e-4
      7014.60c -8.64e-4
      7015.66c -3.294e-6
      8016.60c -0.527349
      8017.66c -2.01148e-4
      9019.62c -1.8e-4
      11023.62c -0.00567
      12000.62c -0.0045
      13027.42c -0.0639
      14028.24c -0.2763
      14029.24c -0.01404
      14030.24c -0.00927
      15031.50c -5.85e-4
      17000.64c -9e-5
      19000.62c -0.0126
      20000.62c -0.01233
```

```
      21045.62c -6.3e-6
      22000.62c -0.0045
      23000.62c -9.0e-5
      24050.60c -3.915e-5
      24052.60c -7.542e-4
      24053.60c -8.550e-5
      24054.60c -2.133e-5
      25055.62c -7.65e-4
      26054.60c -0.001998
      26056.60c -0.03141
      26057.60c -5.7213e-4
      26058.62c -9.648e-5
      27059.66c -7.2e-6
      28000.50c -3.6e-5
      29000.50c -1.8e-5
      37085.66c -6.4953e-5
      37087.66c -2.5047e-5
      39089.42c -4.5e-5
      40090.66c -1.3896e-4
      40091.66c -3.029e-5
      40092.66c -4.63086e-4
      40094.66c -4.6926e-5
      40096.66c -7.56e-6
      56138.66c -4.5e-4
      72000.60c -5.4e-6
      82000.42c -9.0e-6
      90232.60c -4.5e-6
c -----------------------------------
c
```

```
c Boron Carbide - B4C
c Density: 2.52 g/cc
c
c -----------------------------------
 m323 5010.66c -0.1550
      5011.60c -0.6277
      6012.50c -0.2150
      6013.42c -0.002413
c -----------------------------------
c
c Borated Polytheylene
c Density: 1.00 g/cc
c Source: PNNL Materials Compendium Rev 1
c
c -----------------------------------
 m324 1001.62c -0.1254
      5010.66c -0.01999
      5011.60c -0.08010
      6012.50c -0.7763
      6013.42c -0.008288
c
c END MATERIALS
c -----------------------------------
c -----------------------------------
c Begin data cards
c -----------------------------------
 mode n p
 phys:p
 nps 5e8
```

```
c ctme 1000
 imp:n 1 1 1 0
 imp:p 1 1 1 0
 sdef pos=0 0 -0.5 erg=14
c PTRAC file=asc max=1e6 nps=1,200 type=n write=all
 print
c ----------------------------------
c Tallies
c ----------------------------------
 F101:P 2003
 E101 3e-8 118i 12 T
 T101 1500 10000 T
 F201:N 2003
 E201 3e-8 118i 14 T
 F301:N 2002
 E301 3e-8 118i 14 T
c -=-=-=-=-=-=-=-
c End of Input Deck
c -=-=-=-=-=-=-=-
```

A.3 Signal Calcuation

```
 M107 Shell signal run
c -=-=-=-=-=-=-=-=-=-=-=-=-=-=-=-=-=-=-=-=-=-=-=-=-=-=-=-=-=-=-=-=-=-=-=-=-=-
c Cell cards - origin at center of sphere
c -=-=-=-=-=-=-=-=-=-=-=-=-=-=-=-=-=-=-=-=-=-=-=-=-=-=-=-=-=-=-=-=-=-=-=-=-=-
 1101 319 -1.4 +2302 +2001 -2007 +2003 -2004 +2005 -2006
 1102 319 -1.4 -2302 +2005 -2305
 1103 319 -1.4 -2302 +2306 -2006
```

```
1201 320 -7.85 -2302 +2305 -2303
1202 320 -7.85 -2302 +2304 -2306
1203 320 -7.85 +2301 -2302 +2303 -2304
1204 303 -1.82 -2301 +2303 -2304
1301 301 -0.0012 +2007 -2125 +2003 -2004 +2005 -2006
1302 301 -0.0012 +2125 -2126 +2003 -2111 +2005 -2006
1303 301 -0.0012 +2125 -2126 +2111 -2112 +2005 -2123
1304 301 -0.0012 +2125 -2126 +2111 -2112 +2124 -2006
1305 301 -0.0012 +2125 -2126 +2112 -2004 +2005 -2006
1306 301 -0.0012 +2126 -2002 +2003 -2004 +2005 -2006
1307 323 -2.52 +2125 -2201 +2111 -2112 +2123 -2124
1411 324 -3.67 +2128 -2127 +2109 -2107 +2120 -2122
1412 324 -3.67 +2128 -2127 +2105 -2103 +2120 -2122
1413 324 -3.67 +2128 -2127 +2101 -2102 +2120 -2122
1414 324 -3.67 +2128 -2127 +2104 -2106 +2120 -2122
1415 324 -3.67 +2128 -2127 +2108 -2110 +2120 -2122
1421 324 -3.67 +2128 -2127 +2109 -2107 +2116 -2118
1422 324 -3.67 +2128 -2127 +2105 -2103 +2116 -2118
1423 324 -3.67 +2128 -2127 +2101 -2102 +2116 -2118
1424 324 -3.67 +2128 -2127 +2104 -2106 +2116 -2118
1425 324 -3.67 +2128 -2127 +2108 -2110 +2116 -2118
1431 324 -3.67 +2128 -2127 +2109 -2107 +2113 -2114
1432 324 -3.67 +2128 -2127 +2105 -2103 +2113 -2114
1433 324 -3.67 +2128 -2127 +2101 -2102 +2113 -2114
1434 324 -3.67 +2128 -2127 +2104 -2106 +2113 -2114
1435 324 -3.67 +2128 -2127 +2108 -2110 +2113 -2114
1441 324 -3.67 +2128 -2127 +2109 -2107 +2117 -2115
1442 324 -3.67 +2128 -2127 +2105 -2103 +2117 -2115
1443 324 -3.67 +2128 -2127 +2101 -2102 +2117 -2115
```

```
1444 324 -3.67 +2128 -2127 +2104 -2106 +2117 -2115
1445 324 -3.67 +2128 -2127 +2108 -2110 +2117 -2115
1451 324 -3.67 +2128 -2127 +2109 -2107 +2121 -2119
1452 324 -3.67 +2128 -2127 +2105 -2103 +2121 -2119
1453 324 -3.67 +2128 -2127 +2101 -2102 +2121 -2119
1454 324 -3.67 +2128 -2127 +2104 -2106 +2121 -2119
1455 324 -3.67 +2128 -2127 +2108 -2110 +2121 -2119
1501 325 -2.7 +2128 -2127 +2111 -2109 +2123 -2124
1502 325 -2.7 +2128 -2127 +2123 -2121 +2109 -2110
1503 325 -2.7 +2128 -2127 +2123 -2124 +2110 -2112
1504 325 -2.7 +2128 -2127 +2122 -2124 +2109 -2110
1505 325 -2.7 +2128 -2127 +2107 -2105 +2121 -2122
1506 325 -2.7 +2128 -2127 +2103 -2101 +2121 -2122
1507 325 -2.7 +2128 -2127 +2102 -2104 +2121 -2122
1508 325 -2.7 +2128 -2127 +2106 -2108 +2121 -2122
1511 325 -2.7 +2128 -2127 +2109 -2107 +2118 -2120
1512 325 -2.7 +2128 -2127 +2105 -2103 +2118 -2120
1513 325 -2.7 +2128 -2127 +2101 -2102 +2118 -2120
1514 325 -2.7 +2128 -2127 +2104 -2106 +2118 -2120
1515 325 -2.7 +2128 -2127 +2108 -2110 +2118 -2120
1521 325 -2.7 +2128 -2127 +2109 -2107 +2114 -2116
1522 325 -2.7 +2128 -2127 +2105 -2103 +2114 -2116
1523 325 -2.7 +2128 -2127 +2101 -2102 +2114 -2116
1524 325 -2.7 +2128 -2127 +2104 -2106 +2114 -2116
1525 325 -2.7 +2128 -2127 +2108 -2110 +2114 -2116
1531 325 -2.7 +2128 -2127 +2109 -2107 +2115 -2113
1532 325 -2.7 +2128 -2127 +2105 -2103 +2115 -2113
1533 325 -2.7 +2128 -2127 +2101 -2102 +2115 -2113
1534 325 -2.7 +2128 -2127 +2104 -2106 +2115 -2113
```

```
 1535 325 -2.7 +2128 -2127 +2108 -2110 +2115 -2113
 1541 325 -2.7 +2128 -2127 +2109 -2107 +2119 -2117
 1542 325 -2.7 +2128 -2127 +2105 -2103 +2119 -2117
 1543 325 -2.7 +2128 -2127 +2101 -2102 +2119 -2117
 1544 325 -2.7 +2128 -2127 +2104 -2106 +2119 -2117
 1545 325 -2.7 +2128 -2127 +2108 -2110 +2119 -2117
 1591 325 -2.7 +2201 -2128 +2111 -2112 +2123 -2124
 1592 325 -2.7 +2127 -2126 +2111 -2112 +2123 -2124
 1999 0 -2001:+2002:-2003:+2004:-2005:+2006

c -=-=-=-=-=-=-=-=-=-=-=-=-=-=-=-=-=-=-=-=-=-=-=-=-=-=-=-=-=-=-=-=-=-=-
c Surface cards
c -=-=-=-=-=-=-=-=-=-=-=-=-=-=-=-=-=-=-=-=-=-=-=-=-=-=-=-=-=-=-=-=-=-=-
 2001 PZ -200
 2002 PZ 200
 2003 PX -200
 2004 PX +200
 2005 PY -200
 2006 PY +200
 2007 PZ 0
 2101 PX -5.08
 2102 PX +5.08
 2103 PX -6.48
 2104 PX +6.48
 2105 PX -16.64
 2106 PX +16.64
 2107 PX -18.04
 2108 PX +18.04
 2109 PX -28.2
```

```
 2110 PX +28.2
 2111 PX -29.9
 2112 PX +29.9
 2113 PY -5.08
 2114 PY +5.08
 2115 PY -6.48
 2116 PY +6.48
 2117 PY -16.64
 2118 PY +16.64
 2119 PY -18.04
 2120 PY +18.04
 2121 PY -28.2
 2122 PY +28.2
 2123 PY -29.9
 2124 PY +29.9
 2125 PZ 10.16
 2128 PZ 30.86
 2127 PZ 71.5
 2126 PZ 72.2
 2201 PZ 30.16
 2301 C/Y 0 -40.017 7.747
 2302 C/Y 0 -40.017 9.017
 2303 PY -30
 2304 PY +30
 2305 PY -31.27
 2306 PY +31.27

c -=-=-=-=-=-
c Data cards
```

```
c -=-=-=-=-=-
c BEGIN MATERIALS
c -----------------------------------
c Air (80% N, 20% O; 0.0012 g/cc)
c -----------------------------------
 m301 07014.62c -0.75086
      08016.62c -0.23555
      18000.42c -0.01281
      01001.62c -0.00064
      06000.24c -0.00014
c -----------------------------------
c RDX c3H6N6O6
c Density: 1.82 g/cc
c -----------------------------------
 m303 6000.60c 3
      1001.50d  6
      7014.62c 6
      8016.60c 6
c -----------------------------------
c HMX c4H8N8O8
c Density: 1.91 g/cc
c -----------------------------------
 m304 6000.60c 4
      1001.50d  8
      7014.62c 8
      8016.60c 8
c -----------------------------------
c ANFO
c Data from:
```

```
c Explosives Detection and Identification by PGNAA
c by EH Seabury and AJ Caffrey
c Density: 0.84 g/cc for mining grade
c -----------------------------------
  m305 6000.60c -0.026
       1001.50d -0.054
       7014.62c -0.339
       8016.60c -0.581
c -----------------------------------
c Nitrogen for F4 tally
c -----------------------------------
 m399 7014.62c 1
c -----------------------------------
c Conventional Concrete
c Data from:
c Neutron Scattering in Concrete and Wood
c A Facure, A X Silvia, C Falcao, and V R Crispim
c Radiation Protection Dosimetry 119 (2006) pp 514-517
c Density: 2.26 g/cc
c -----------------------------------
 m306 1001.62c -0.0055
      8016.60c -0.4957
      11023.62c -0.0170
      19000.62c -0.0191
      12000.62c -0.0026
      13027.42c -0.0455
      14028.24c -0.2892
      14029.24c -0.01469
      14030.24c -0.009680
```

```
      16000.62c -0.0013
      20000.62c -0.0826
      26054.60c -7.189e-4
      26056.60c -0.01129
      26057.60c -2.606e-4
      26058.62c -3.469e-5
c -----------------------------------
c 10% water moist sand
C Density: 1.702 g/cc
c -----------------------------------
 m315 1001.62c -0.011898
      8016.60c -0.5698119
      14028.24c -0.420687
c -----------------------------------
c World average soil
c Source:
c Basic Considerations for Monte Carlo Calculations in Soil
c Applied Radiation and Isotopes 62 (2005) 97-107
c Typical density = 1.2 - 1.6 g/cc
c Isotope abundance data from It's Elemental
c education.jlab.org/itselemental
c -----------------------------------
 m319 3006.66c -2.25e-6
      3007.66c -2.775e-6
      5010.66c -1.98e-6
      5011.60c -8.02e-6
      6012.50c -0.0198
      6013.42c -2.22e-4
      7014.60c -9.96e-4
```

```
7015.66c -3.66e-6
8016.60c -0.4875
8017.66c -1.86e-4
9019.62c -2.0e-4
11023.62c -0.0063
12000.62c -0.005
13027.42c -0.071
14028.24c -0.307
14029.24c -0.0156
14030.24c -0.0103
15031.50c -6.5e-4
17000.64c -1.0e-4
19000.62c -0.014
20000.62c -0.0137
21045.62c -7.0e-6
22000.62c -0.0050
23000.62c -1.0e-4
24050.60c -4.35e-5
24052.60c -8.38e-4
24053.60c -9.50e-5
24054.60c -2.37e-5
25055.62c -8.5e-4
26054.60c -0.00222
26056.60c -0.0349
26057.60c -6.357e-4
26058.62c -1.072e-4
27059.66c -8.0e-6
28000.50c -4.0e-5
29000.50c -2.0e-5
```

```
      37085.66c -7.217e-5
      37087.66c -2.783e-5
      39089.42c -5.0e-5
      40090.66c -1.544e-4
      40091.66c -3.366e-5
      40092.66c -5.1454e-4
      40094.66c -5.214e-5
      40096.66c -8.4e-6
      56138.66c -5.0e-4
      72000.60c -6.0e-6
      82000.42c -1.0e-5
      90232.60c -5.0e-6
c -----------------------------------
c
c A36 Steel
c From ASTM spec sheet
c Density: 7.85 g/cc
c
c -------------------------------------
 m320 6012.50c -0.0025
      29000.50c -0.0020
      26054.60c -0.057281
      26056.60c -0.89919
      26057.60c -0.020766
      26058.62c -0.0027636
      25055.62c -0.0103
      15031.50c -0.00040
      14028.24c -0.0025824
      14029.24c -0.000131124
```

```
      14030.24c -8.6436e-5
c -----------------------------------
c
c Typical Western US Earth
c From PNNL 15870 Rev 1
c Density: 1.52 g/cc
c
c -----------------------------------
 m321 1001 -0.023834
      8016 -0.598898
      13027 -0.080446
      14000 -0.296821
c -----------------------------------
c
c World Average soil, 10 percent moisture
c Density: 1.4 g/cc
c
c -----------------------------------
 m322 1001.62c -0.011190
      3006.66c -2.03e-6
      3007.66c -2.4975e-6
      5010.66c -1.782e-6
      5011.60c -7.218e-6
      6012.50c -0.01782
      6013.42c -1.998e-4
      7014.60c -8.64e-4
      7015.66c -3.294e-6
      8016.60c -0.527349
      8017.66c -2.01148e-4
```

```
9019.62c -1.8e-4
11023.62c -0.00567
12000.62c -0.0045
13027.42c -0.0639
14028.24c -0.2763
14029.24c -0.01404
14030.24c -0.00927
15031.50c -5.85e-4
17000.64c -9e-5
19000.62c -0.0126
20000.62c -0.01233
21045.62c -6.3e-6
22000.62c -0.0045
23000.62c -9.0e-5
24050.60c -3.915e-5
24052.60c -7.542e-4
24053.60c -8.550e-5
24054.60c -2.133e-5
25055.62c -7.65e-4
26054.60c -0.001998
26056.60c -0.03141
26057.60c -5.7213e-4
26058.62c -9.648e-5
27059.66c -7.2e-6
28000.50c -3.6e-5
29000.50c -1.8e-5
37085.66c -6.4953e-5
37087.66c -2.5047e-5
39089.42c -4.5e-5
```

```
      40090.66c -1.3896e-4
      40091.66c -3.029e-5
      40092.66c -4.63086e-4
      40094.66c -4.6926e-5
      40096.66c -7.56e-6
      56138.66c -4.5e-4
      72000.60c -5.4e-6
      82000.42c -9.0e-6
      90232.60c -4.5e-6
c -----------------------------------
c
c Boron Carbide - B4C
c Density: 2.52 g/cc
c
c -----------------------------------
 m323 5010.66c -0.1550
      5011.60c -0.6277
      6012.50c -0.2150
      6013.42c -0.002413
c ---------------------------------
c Sodium Iodide
c Density: 3.67 g/cc
c ---------------------------------
 m324 11023 -0.153373
      53127 -0.846627
c --------------------------------
c Aluminum
c Density: Density: 2.7 g/cc
c --------------------------------
```

```
 m325 13027.42c 1
c
c END MATERIALS
c ----------------------------------
c ----------------------------------
c Begin data cards
c ----------------------------------
 mode n p
 phys:p
 nps 1e9
c ctme 1000
 imp:p 1 68r 0
 imp:n 1 68r 0
 sdef pos=0 0 0.5 erg=14.1
c PTRAC file=asc max=1e6 nps=1,200 type=n write=all
 print
c ----------------------------------
c Tallies
c ----------------------------------
 F118:P 1411
 E118 0 254i 12
 FC118 Gaussian broadened spectrum on detector 11
 FT118 GEB -0.00789 0.06769 0.21159
 F668:P 1411
 FC668 Unbroadened spectrum on detector 11
 E668 0 254i 12
 F128:P 1412
 E128 0 254i 12
 FC128 Gaussian broadened spectrum on detector 12
```

```
FT128 GEB -0.00789 0.06769 0.21159
F678:P 1412
FC678 Unbroadened spectrum on detector 12
E678 0 254i 12
F138:P 1413
E138 0 254i 12
FC138 Gaussian broadened spectrum on detector 13
FT138 GEB -0.00789 0.06769 0.21159
F688:P 1413
FC688 Unbroadened spectrum on detector 13
E688 0 254i 12
F148:P 1414
E148 0 254i 12
FC148 Gaussian broadened spectrum on detector 14
FT148 GEB -0.00789 0.06769 0.21159
F698:P 1414
FC698 Unbroadened spectrum on detector 14
E698 0 254i 12
F158:P 1415
E158 0 254i 12
FC158 Gaussian broadened spectrum on detector 15
FT158 GEB -0.00789 0.06769 0.21159
F608:P 1415
FC608 Unbroadened spectrum on detector 15
E608 0 254i 12
F218:P 1421
E218 0 254i 12
FC218 Gaussian broadened spectrum on detector 21
FT218 GEB -0.00789 0.06769 0.21159
```

```
F768:P 1421
FC768 Unbroadened spectrum on detector 21
E768 0 254i 12
F228:P 1422
E228 0 254i 12
FC228 Gaussian broadened spectrum on detector 22
FT228 GEB -0.00789 0.06769 0.21159
F778:P 1422
FC778 Unbroadened spectrum on detector 22
E778 0 254i 12
F238:P 1423
E238 0 254i 12
FC238 Gaussian broadened spectrum on detector 23
FT238 GEB -0.00789 0.06769 0.21159
F788:P 1423
FC788 Unbroadened spectrum on detector 23
E788 0 254i 12
F248:P 1424
E248 0 254i 12
FC248 Gaussian broadened spectrum on detector 24
FT248 GEB -0.00789 0.06769 0.21159
F798:P 1424
FC798 Unbroadened spectrum on detector 24
E798 0 254i 12
F258:P 1425
E258 0 254i 12
FC258 Gaussian broadened spectrum on detector 25
FT258 GEB -0.00789 0.06769 0.21159
F708:P 1425
```

```
FC708 Unbroadened spectrum on detector 25
E708 0 254i 12
F318:P 1431
E318 0 254i 12
FC318 Gaussian broadened spectrum on detector 31
FT318 GEB -0.00789 0.06769 0.21159
F868:P 1431
FC868 Unbroadened spectrum on detector 31
E868 0 254i 12
F328:P 1432
E328 0 254i 12
FC328 Gaussian broadened spectrum on detector 32
FT328 GEB -0.00789 0.06769 0.21159
F878:P 1432
FC878 Unbroadened spectrum on detector 32
E878 0 254i 12
F338:P 1433
E338 0 254i 12
FC338 Gaussian broadened spectrum on detector 33
FT338 GEB -0.00789 0.06769 0.21159
F888:P 1433
FC888 Unbroadened spectrum on detector 33
E888 0 254i 12
F348:P 1434
E348 0 254i 12
FC348 Gaussian broadened spectrum on detector 34
FT348 GEB -0.00789 0.06769 0.21159
F898:P 1434
FC898 Unbroadened spectrum on detector 34
```

```
E898 0 254i 12
F358:P 1435
E358 0 254i 12
FC358 Gaussian broadened spectrum on detector 35
FT358 GEB -0.00789 0.06769 0.21159
F808:P 1435
FC808 Unbroadened spectrum on detector 35
E808 0 254i 12
F418:P 1441
E418 0 254i 12
FC418 Gaussian broadened spectrum on detector 41
FT418 GEB -0.00789 0.06769 0.21159
F968:P 1441
FC968 Unbroadened spectrum on detector 41
E968 0 254i 12
F428:P 1442
E428 0 254i 12
FC428 Gaussian broadened spectrum on detector 42
FT428 GEB -0.00789 0.06769 0.21159
F978:P 1442
FC978 Unbroadened spectrum on detector 42
E978 0 254i 12
F438:P 1443
E438 0 254i 12
FC438 Gaussian broadened spectrum on detector 43
FT438 GEB -0.00789 0.06769 0.21159
F988:P 1443
FC988 Unbroadened spectrum on detector 43
E988 0 254i 12
```

```
F448:P 1444
E448 0 254i 12
FC448 Gaussian broadened spectrum on detector 44
FT448 GEB -0.00789 0.06769 0.21159
F998:P 1444
FC998 Unbroadened spectrum on detector 44
E998 0 254i 12
F458:P 1445
E458 0 254i 12
FC458 Gaussian broadened spectrum on detector 45
FT458 GEB -0.00789 0.06769 0.21159
F908:P 1445
FC908 Unbroadened spectrum on detector 45
E908 0 254i 12
F518:P 1451
E518 0 254i 12
FC518 Gaussian broadened spectrum on detector 51
FT518 GEB -0.00789 0.06769 0.21159
F068:P 1451
FC068 Unbroadened spectrum on detector 51
E068 0 254i 12
F528:P 1452
E528 0 254i 12
FC528 Gaussian broadened spectrum on detector 52
FT528 GEB -0.00789 0.06769 0.21159
F078:P 1452
FC078 Unbroadened spectrum on detector 52
E078 0 254i 12
F538:P 1453
```

```
 E538 0 254i 12
 FC538 Gaussian broadened spectrum on detector 53
 FT538 GEB -0.00789 0.06769 0.21159
 F088:P 1453
 FC088 Unbroadened spectrum on detector 53
 E088 0 254i 12
 F548:P 1454
 E548 0 254i 12
 FC548 Gaussian broadened spectrum on detector 54
 FT548 GEB -0.00789 0.06769 0.21159
 F098:P 1454
 FC098 Unbroadened spectrum on detector 54
 E098 0 254i 12
 F558:P 1455
 E558 0 254i 12
 FC558 Gaussian broadened spectrum on detector 55
 FT558 GEB -0.00789 0.06769 0.21159
 F008:P 1455
 FC008 Unbroadened spectrum on detector 55
 E008 0 254i 12
 F101:P 2201
 FC101 Photon flux in to detector array
 E101 0 254i 12
 T101 1500 10000 T
 C101 0 1
c -=-=-=-=-=-=-=-=-
c End of Input Deck
c -=-=-=-=-=-=-=-=-
```

A.4 Efficiency Simulation

```
 HPGe efficiency simulation
c -=-=-=-=-=-=-=-=-=-=-=-=-=-=-=-=-=-=-=-=-=-=-=-=-=-=-=-=-=-=-=-=-=-=-=-=-
c Cell cards - origin at center of sphere
c -=-=-=-=-=-=-=-=-=-=-=-=-=-=-=-=-=-=-=-=-=-=-=-=-=-=-=-=-=-=-=-=-=-=-=-=-
 1001 303 -8.96 +2001 -2002 -2003
 1002 303 -8.96 +2004 -2003 +2002 -2005
 1003 303 -8.96 +2005 -2006 -2003
 1101 0 +2002 -2101 -2004
 1102 0 +2101 -2106 +2103 -2004
 1103 0 +2106 -2005 -2004
 1201 302 -2.6989 +2101 -2102 -2103
 1202 302 -2.6989 +2104 -2103 +2102 -2105
 1203 302 -2.6989 +2105 -2106 -2103
 1301 0 +2203 -2105 -2104
 1302 0 +2201 -2203 -2202
 1401 304 -5.323 (+2102 -2201 -2104):(+2201 -2203 +2202 -2104)
 1501 0 -2003 +2006 -2500
 1502 0 -2003 -2001 -2500
 1503 0 +2003 -2500
 1999 0 +2500

c -=-=-=-=-=-=-=-=-=-=-=-=-=-=-=-=-=-=-=-=-=-=-=-=-=-=-=-=-=-=-=-=-=-=-=-=-
c Surface cards
c -=-=-=-=-=-=-=-=-=-=-=-=-=-=-=-=-=-=-=-=-=-=-=-=-=-=-=-=-=-=-=-=-=-=-=-=-
 2001 PZ 0.0
 2002 PZ 0.1
 2003 CZ 4.758
```

```
 2004 CZ 4.478
 2005 PZ 11.403
 2006 PZ 11.503
 2101 PZ 0.5
 2102 PZ 0.503
 2103 CZ 4.078
 2104 CZ 4.075
 2105 PZ 10.703
 2106 PZ 11.003
 2201 PZ 1.903
 2202 CZ 0.46
 2203 PZ 5.703
 2500 SO 100

c -=-=-=-=-=-
c Data cards
c -=-=-=-=-=-
c BEGIN MATERIALS
c ----------------------------------
c Sodium Iodide
c Density: 3.67 g/cc
c ----------------------------------
 m301 11000.04p 1
      53000.04p 1
c ----------------------------------
c Aluminum
c Density 2.6989 g/cc
c ----------------------------------
 m302 13000.04p 1
```

```
c ----------------------------------
c Copper
c Density: 8.96 g/cc
c ----------------------------------
 m303 29000 -1.000
c ----------------------------------
c Germanium
c Density: 5.323 g/cc
c ----------------------------------
 m304 32000 -1.0
c
c
c END MATERIALS
c ----------------------------------
c ----------------------------------
c Begin data cards
c ----------------------------------
 mode p
 nps 1e7
c ctme 1000
 imp:p 1 14r 0
 sdef pos=0 1.358 -0.01 DIR=1 VEC=0 0.8660 0.5000 erg=3.603500
c PTRAC file=asc max=1e6 nps=1,200 type=n write=all
 print
c ----------------------------------
c Tallies
c ----------------------------------
 F18:P 1401
 E18 0 254i 12
```

```
c FT18 GEB -0.00789 0.06769 0.21159
c -=-=-=-=-=-=-=-=-=-
c End of Input Deck
c -=-=-=-=-=-=-=-=-=-
```

REFERENCES

REFERENCES

[1] DOD Personnel and Defense Manpower Data Center Casualty Statistics. Casualty summary by reason, October 7, 2001 through May 31, 2011. `http://siadapp.dmdc.osd.mil/personnel/CASUALTY/gwot_reason.pdf`, May 2011.

[2] Committee on Defeating Improvised Explosive Devices. Disrupting improvised explosive terror campaigns. Technical report, National Research Council, 2008.

[3] A. R Oppenheimer. *IRA: The Bombs and the Bullets*. Irish Academy Press, 2009.

[4] Carlo Kopp. Technology of improvised explosive devices. *Defence Today*, 6(3), 2007.

[5] Countering the threat of improvised explosive devices: Basic research opportunities (abbreviated version). Technical report, National Research Council, 2007.

[6] Maurice Marshall and Jimmie C. Oxley. *Aspects of Explosives Detection*. Elsevier, 2009.

[7] Jared Olson. Personal communication, 2008.

[8] Ordata. `maic.jmu.edu/ordata/`.

[9] Department of Defense. IED photograph. `http://www.defenselink.mil/news/Nov2005/20051109115418_11iraqb1-20051109.jpg`, Nov 2005.

[10] B.T. Fedoroffet et. al. Encyclopedia of explosives and related items. Technical Report PATR-2700, U.S. Army Research and Development Command, 1969.

[11] K. Eblagh. Practical problems in demining and their solutions. *IEEE Conference Publications*, 1996(CP431):1–5, 1996.

[12] Larry T. Lowe, Lloyd S. Riggs, Steve Cash, and Thomas H. Bell. Improvements to the u.s. army's an/pss-12 metal detector to enhance landmine discrimination capabilities. volume 4394, pages 85–96. SPIE, 2001.

[13] Y. Das, J.T. Dean, D. Lewis, J.H.J. Roosenboom, and G. Zahaczewsky. International pilot project for technology co-operation final report: A multi-national technical evaluation of performance of commercial off the shelf metal detectors in the context of humanitarian demining. Technical Report EUR 19719 EN, Joint Research Centre, 2001.

[14] Jacqueline MacDonald and J. R. Lockwood. *Alternatives for Landmine Detection*. RAND Corporation, 2003.

[15] P. Lopez, H. Sahli, and D. Cabello. Detection and classification of landmines from infrared images. In *Proceedings of EUDEM2-SCOT-2003: International Conference on Requirements and Technologies for the Detection, Removal, and Neutralization of Landmines and UXO*, page 242252, 2003.

[16] Khalil Khanafer and Kambiz Vafai. Thermal analysis of buried land mines over a diurnal cycle. *IEEE Transactions on Geoscience and Remote Sensing*, 40:461–473, 2002.

[17] John A. Hermann and Ian J. Chant. Microwave enhancement of thermal land mine signatures. volume 3710, pages 154–166. SPIE, 1999.

[18] O. Robert Mitchell, Srinivasa R. Somu, and Sanjeev Agarwal. Detection of antipersonnel land mines based on waterjet-induced thermal images. volume 3710, pages 180–188. SPIE, 1999.

[19] A. Wexler. Electrical impedance imaging in two and three dimensions. *Clinical physics and physiological measurement*, 9, Suppl. A:29 – 33, 1988.

[20] Philip Church, John Elton McFee, Stephane Gagnon, and Philip Wort. Electrical impedance tomographic imaging of buried landmines. *IEE Transactions on Geoscience and Remote Sensing*, 44:2407 – 2402, 2006.

[21] N. R. Butt, E. Gudmundson, A. Jakobsson, B. Rameev T. Apih, G. Mozzhukhin, and J. Barras. *Magnetic Resonance Detection of Explosives and Illicit Materials*. Springer, 2014.

[22] Frank S. Rotondo and Elizabeth Ayers. Antitank and antipersonnel mine detection test results for a nuclear quadrupole resonance detection system. Technical report, Institute for Defense Analyses, 2000.

[23] A.N. Garroway, M.L. Buess, J.B. Miller, Bryan H. Suits, A.D. Hibbs, G.A. Barrall, R. Matthews, and L.J. Burnett. Remote sensing by nuclear quadrupole resonance. *Geoscience and Remote Sensing, IEEE Transactions on*, 39(6):1108–1118, Jun 2001.

[24] J˙ . Campbell. Detection of buried land mines by compton backscatter imaging. *Nuclear Science and Engineering*, 110:417 – 424, 1992.

[25] Esam M. A. Hussein and Edward J. Waller. Review of one-side approaches to radiographic imaging for detection of explosives and narcotics. *Radiation Measurements*, 29(6):581 – 591, 1998.

[26] Nist XCOM: Photon cross sections database. `http://www.nist.gov/physlab/data/xcom/`.

[27] R.B. Firestone. *Table of Isotopes, 8th Ed.* Lawrence Berkeley National Laboratory, 1999.

[28] Marc Litz, Christopher Waits, and Jennifer Mullens. Neutron-activated gamma-emission: Technology review. Technical Report ARL-TR-5871, Army Research Laboratory, January 2012.

[29] L. Wielopolski, Z. Song, I Orion, A. L. Hanson, and G. Hendrey. Basic considerations for Monte Carlo calculations in soil. *Applied Radiation and Isotopes*, 62:97–107, 2005.

[30] Bubble Technology Industries Inc. Feasibility of fast neutron analysis (FNA) for detection of buried landmines. Technical Report CR 2004-201, DRDC Suffield, 2004.

[31] Evaluated nuclear data file. `http://www.nndc.bnl.gov/exfor/endf00.jsp`.

[32] CapGam. `http://www.nndc.bnl.gov/capgam/`.

[33] X-5 Monte Carlo Team. *MCNP A General Monte Carlo N-Particle Transport Code, Version 5 Volume I: Overview and Theory*. Los Alamos National Laboratory, April 2003.

[34] William L. Dunn and J. Kenneth Shultis, editors. *Exploring Monte Carlo Methods*. Else, 2011.

[35] Forrest B. Brown. Fundamentals of monte carlo particle transport. Technical Report LA-UR-05-4983, Los Alamos National Laboratory, 2005.

[36] X-5 Monte Carlo Team. Mcnp - a general monte carlo n-particle transport code, version 5. Technical Report LA-CP-03-0245, Los Alamos National Laboratory, 2003.

[37] R.C. Martin, J.B. Knauer, and P.A. Balo. Production, distribution and applications of californium-252 neutron sources. *Applied Radiation and Isotopes*, 53:785 – 792, 2000.

[38] J. Terrell. *Physics and Chemistry of Fission*, volume 2. Vienna: IAEA, 1965.

[39] T.E. Valentine. Evaluation of prompt fission gamma rays for use in simulating nuclear safeguard measurements. Technical Report ORNL/TM-1999/300, 1999.

[40] A. Facure, A. X. Silvia, C. Falcao, and V. R. Crispim. Neutron scattering in concrete and wood. *Radiation Protection Dosimetry*, 119:514–517, 2006.

[41] Glenn F. Knoll. *Radiation Detection and Measurement*. John Wiley and Sons, 3 edition, 2000.

[42] T.K. Gupta. *Radiation, Ionization, and Detection in Nuclear Medicine*. Springer Berlin Heidelberg, 2013.

[43] Mitsuru Ishii and Masaaki Kobayashi. Single crystals for radiation detectors. *Progress in Crystal Growth and Characterization of Materials*, 23:245 – 311, 1992.

[44] Michal Gierlik, Tadeusz Batsch, Marek Moszyński, Dariusz Wolski Tomasz Szczęśniak, Wlodzimierz Klamra, Bertrand Perot, and Gregory Perret. Comparative study of large NaI(Tl) and BGO scintillators for the EURopean Illicit TRAfficking Countermeasures Kit project. In *IEEE Nuclear Science Symposium Conference Record*, 2005.

[45] G. Vourvopoulos and F.J. Schultz. A pulsed fast-thermal neutron system for the detention of hidden explosives. *Nuclear Instruments & Methods in Physics Research, Section B*, 79:585 – 588, 1993.

[46] Gordon R. Gilmore. *Practical Gamma Ray Spectroscopy*. John Wiley and Sons, 2 edition, 2008.

[47] C.E. Moss and E.W. Tissinger. Efficiency of 7.62 cm bismuth germanate scintillators. *Nuclear llastruments and Methods in Physics Research*, 221:378–384, 1984.

[48] L. Jarczyk, H. Knoepfell, J. Lang, R. Müller, and W. Wölfli. Photopeak efficiency and response function of various NaI(Tl) and CsI(Tl) crystals in the energy range up to 11 MeV. *Nuclear Instruments and Methods in Physics Research*, 17:310–320, 1962.

[49] Chang Su Park, Gwang Min Sun, and H.D. Choi. Experimental and simulated efficiency of a HPGe detector in the energy range of 0.06 – 11 MeV. *Journal of the Korean Nuclear Society*, 35(3):234–242, 2003.

[50] Charles L. Melcher. Scintillation crystals for PET. *The Journal of Nuclear Medicine*, 41:1051–1055, 2000.

[51] G. A. Thieme, W. R. Hendee, G. S. Ibbott, P. L. Carson, and D. L. Kirch. Cross–sectional anatomic images by gamma ray transmission scanning. *Acta Radiologica Therapy Physics Biology*, 14:81–112, 1975.

[52] ORTEC X-Cooler II. `http://www.ortec-online.com/download.asbx?AttributeFileId=9019fa55-f662-4acd-8d0a-ca9759bdfd78`.

[53] Hashem Miri Hakimabad, Hamed Panjeh, and Alireza Vejdani-Noghreiyan. Evaluation the nonlinear response function of a 3×3 in nai scintillation detector for pgnaa applications. *Ap*, 65:918 – 926, 2007.

[54] M.H. Hadizadeh Yazdi, A.A. Mowlavi, M.N. Thompson, and H. Miri Hakimabad. Proper shielding for NaI(Tl) detectors in combined neutron-γ fields using mcnp. *Nuclear Instruments and Methods in Physics Research A*, 522:447 – 454, 2004.

[55] L. Porter and D. A. Sparrow. Assessment of thermal neutron activation applied to surface and near surface unexploded ordnance. P-3339, IDA, 1997.

[56] Sarah E. Bender. Application of monte carlo modeling of compton suppression spectroscopy to spent fuel material accountancy. Master's thesis, Pennsylvania State University, 2011.

[57] The best choice of high purity germanium (*hpge*) detector.

[58] J.E. McFee, A.A. Faust, H.R. Andrews, V. Kovaltchouk, E.T. Clifford, and H. Ing. A comparison of fast inorganic scintillators for thermal neutron analysis landmine detection. *Nuclear Science, IEEE Transactions on*, 56(3):1584–1592, June 2009.

VITA

VITA

Matthew David Marziale was born in Virginia in 1983. His family lived in a number of cities in the states of Virginia and Kentucky, where he attended twelve years of public school instruction. He started his post secondary education in physics at Purdue in 2002, where he majored in physics. He served as an undergraduate research assistant during the final two years of his undergraduate education. He graduated from Purdue in 2006.

He continued his studies at Purdue University, purusing a Ph.D. in physics. He was both a teaching and research assistant from 2006 to 2013. He graduated with his Ph.D. in physics in May, 2016.